

Electronic Thesis and Dissertation Repository

---

4-19-2017 12:00 AM

## Detection and Characterization of Extrasolar Planets through Planet-Disk Dynamical Interactions

Maryam Tabeshian  
*The University of Western Ontario*

Supervisor  
Prof. Paul A. Wiegert  
*The University of Western Ontario*

Graduate Program in Astronomy  
A thesis submitted in partial fulfillment of the requirements for the degree in Doctor of Philosophy  
© Maryam Tabeshian 2017

Follow this and additional works at: <https://ir.lib.uwo.ca/etd>



Part of the [Other Astrophysics and Astronomy Commons](#)

---

### Recommended Citation

Tabeshian, Maryam, "Detection and Characterization of Extrasolar Planets through Planet-Disk Dynamical Interactions" (2017). *Electronic Thesis and Dissertation Repository*. 4503.  
<https://ir.lib.uwo.ca/etd/4503>

This Dissertation/Thesis is brought to you for free and open access by Scholarship@Western. It has been accepted for inclusion in Electronic Thesis and Dissertation Repository by an authorized administrator of Scholarship@Western. For more information, please contact [wlsadmin@uwo.ca](mailto:wlsadmin@uwo.ca).

# Abstract

Structures observed in circumstellar disks may be caused by gravitational interaction with planetary or stellar companions. These perturbed disks are often signposts of planet birth in exoplanetary systems, and offer insights into the properties of both the disk and the perturbing planets. Therefore, structures observed in these disks provide a powerful tool for detecting and studying extrasolar planetary systems. In this work, we examine the link between disk structures and nearby/embedded planets using numerical simulations of both hypothetical and observed disk systems.

We demonstrate that gaps can be opened in dynamically cold debris disks at the mean-motion resonances (MMRs) of an orbiting planet. These gaps are opened away from the orbit of the planet itself, revealing that not all disk gaps need contain a planetary body. These gaps are large and deep enough to be detectable in resolved disk images for a wide range of reasonable disk-planet parameters. The gap location, shape, and size are diagnostic of the planet location, eccentricity and mass, and allow one to infer the existence of unseen planets, as well as calculate many important parameters of both seen and unseen planets in these systems. We suggest that the widths, locations, and shapes of the two most prominent resonances, the 2:1 and 3:1 MMRs, could be used to determine: 1) the position of any unseen planets for more efficient targeted searches, and 2) the mass, semimajor axis and eccentricity of the planetary perturber, and present an algorithm for doing so.

We apply our dynamical model of planet-disk interactions to the protoplanetary disk around the young pre-main sequence star HL Tauri which was observed recently in unprecedented detail by the *Atacama Large Millimeter/submillimeter Array* (ALMA). We determine that the disk structures that are likely sculpted by yet-to-be detected planets embedded in this gas-rich disk can be reproduced to a large extent using a simple particle-only model. For example, the number of planets in the HL Tau system remains a matter of debate; however, our results show that at least 5 of the observed gaps could be produced with only 3 planets in the system, where the additional gaps are due to mean-motion resonances. Our fitting of planetary masses and distances are also consistent with those in the literature. Therefore, we conclude that a particle-only treatment of gas-rich disks may be useful in understanding disk-planet dynamical interactions in some cases, and provide ‘low-cost’ initial parameter determinations which can ultimately be used as a starting point for investigating protoplanetary disks more thoroughly using computationally expensive hydrodynamic models.

In the present study, we show that numerical simulations of circumstellar disks provide a powerful tool for the study of planets and planetary systems which can ultimately help in understanding their formation and evolution.

**Keywords:** celestial mechanics - circumstellar disks - planets and satellites: detection - planets and satellites: fundamental parameters - planet-disk interactions - protoplanetary disks: individual (HL Tau)

# Co-Authorship Statement

This thesis dissertation contains adaptations from three papers that are either published in a peer-reviewed journal or soon will be. These include:

- Chapter 2: *Detection and Characterization of Extrasolar Planets through Mean-Motion Resonances. I. Simulations of Hypothetical Debris Disks*, published in the *Astrophysical Journal* (Tabeshian, M. & Wiegert, P. A., 2016, ApJ, 818, 159);

- Chapter 3: *Detection and Characterization of Extrasolar Planets through Mean-Motion Resonances. II. The Effect of the Planet's Orbital Eccentricity on Debris Disk Structures*, submitted for publication in the *Astrophysical Journal* (Tabeshian, M. & Wiegert, P. A., 2017, ApJ (submitted));

- Chapter 4: *Detection and Characterization of Extrasolar Planets: Applying a Particle-only Model to the HL Tau Disk*, to be submitted for publication.

Contributions to these papers were made by myself as well as by my PhD supervisor, Dr. Paul Wiegert. The simulation codes using a numerical integrator based on the Wisdom-Holman algorithm were written by Dr. Wiegert in C. I ran the code and processed and analyzed the output using a code I wrote in Interactive Data Language (IDL). I then prepared the figures as well as the manuscripts while Dr. Wiegert provided guidance and suggestions on a regular basis. I also wrote a code in IDL which called the simulation code and implemented chi-squared minimization as well as Monte Carlo simulations and uncertainty calculations for the project described in Chapter 4.

# Acknowledgements

## *To my family:*

Since the day I set foot on this planet, I have been blessed with the most incredible family in the world! A mom and dad that have always gone above and beyond for my sister and I to make our dreams come true. Thank you both for raising me up to more than I could ever be and for every sacrifice you made for me to be where I am now. And of course a big thanks to an amazing big sister who has always been by my side, helping me reach for the stars. But how can I ever thank the three of you enough for having my back and for always being there for me, so lovingly, so unconditionally? Without your unwavering support, I could not have gone through the amazing journey that started with a decision a 9 year-old girl made, that one day she would become an astronomer! That journey is not coming to an end with a PhD degree in astronomy; this is just the beginning of a new chapter, and I am truly blessed to have all of you in this with me ...

## *To my friends:*

I consider myself very lucky to have always been surrounded by an amazing support group of friends, some of whom I have long considered family. It is impossible to name all of you here and I only hope that I have been able to tell you how much every single one of you has given meaning to my life.

## *To my teachers:*

Perhaps I need to go back, far back, to the person who first taught me how to read, and thank every single teacher I have had ever since for building the foundations of my humble knowledge. But I would like to especially thank Drs. Stan Metchev and Peter Brown at the University of Western Ontario (UWO) for sharing with me their vast knowledge of planets and planetary systems, as well as Drs. Neil Basescu, with whom I took my first ever astronomy course, and Bert Liberi at the State University of New York, Westchester Community College for their undeniable role in developing my knowledge in physics and in mathematics. Also, my sincere thanks to Dr. Jan Cami at UWO for his help and patience with my programming questions and the dilemmas I so often ran into with my code! And many thanks to Dr. Jamshid Ghanbari, a dear family friend and astronomy professor that my father took me to when I was very young and someone who played a great role in my growing interest in astronomy. Thank you all!

## *To my MSc. supervisor, Dr. Martin Houde:*

When it comes to telling you how grateful I am for what you did for me, I always find myself at a loss for words. It has always been so heartwarming to know that you remained genuinely caring of my progress and wanted what was best for me that makes me incredibly grateful for having had you as my supervisor. Even though I will never be able to say this enough, but thank you for supporting me and my decision at a time that I needed it most. Your support led me to the path for success and gave me so much more that I can't even begin to describe.

*And finally, to my PhD supervisor, Dr. Paul Wiegert:*

I wish I knew where to begin and how to tell you how much a decision you made not even three years ago changed the course of things for me. Thank you for giving me the chance, the honor, the privilege of being your student, which I never took for granted. There are absolutely no words that would do justice in expressing the extent of my gratitude to you for all that you have done for me over the years and for the wealth of knowledge that you generously provided me with. Your support, your encouragement and the faith you have had in me are priceless and I will forever be indebted to you.

# Dedication

*To my parents, for their never-ending love and support ...*

# Contents

<b>Abstract</b>	<b>i</b>
<b>Co-Authorship Statement</b>	<b>ii</b>
<b>Acknowledgements</b>	<b>iii</b>
<b>Dedication</b>	<b>v</b>
<b>List of Figures</b>	<b>ix</b>
<b>List of Tables</b>	<b>xiii</b>
<b>List of Appendices</b>	<b>xiv</b>
<b>1 Prelude</b>	<b>1</b>
1.1 Introduction . . . . .	1
1.2 Protoplanetary and Pre-Transitional Disks . . . . .	3
1.2.1 Observed Disk Structures: Annular Gaps . . . . .	9
TW Hydrae . . . . .	9
HL Tauri . . . . .	11
1.2.2 Observed Disk Structures: Asymmetries . . . . .	12
1.3 Transitional Disks . . . . .	17
1.4 Debris Disks . . . . .	20
1.4.1 Dust Disks . . . . .	25
Structure and Application to the Search for Exoplanets . .	25
1.4.2 Planetesimal Disks . . . . .	29
Mean-Motion Resonance . . . . .	30
1.5 Summary . . . . .	32
<b>2 Planet-Disk Interactions via MMR I: Low Eccentricity Orbits</b>	<b>39</b>
2.1 Introduction . . . . .	39

2.2	The Dynamics of Mean-Motion Resonances . . . . .	43
2.3	Simulations . . . . .	47
2.3.1	The Method . . . . .	47
2.3.2	Simulated Debris Disks . . . . .	48
2.4	Results . . . . .	50
2.4.1	Interior Resonance . . . . .	51
2.4.2	Exterior Resonance . . . . .	54
2.5	Discussion . . . . .	57
2.5.1	Asymmetries in MMR Gaps . . . . .	57
2.5.2	Minimum and Maximum Detectable Planet Masses . . . . .	58
2.5.3	Libration Width vs. Planet Mass . . . . .	60
2.5.4	Resonant Location Versus Planet Mass . . . . .	63
2.5.5	Finding the Planet's Semimajor Axis based on the Observed Gap Width and Location . . . . .	64
2.5.6	The Effect of Planet's Orbital Eccentricity and Lindblad Resonances . . . . .	66
2.5.7	Disk Optical Depth and Gap Contrast . . . . .	68
2.6	Summary and Conclusions . . . . .	71
<b>3</b>	<b>Planet-Disk Interactions via MMR II: The Effect of Eccentricity</b>	<b>76</b>
3.1	Introduction . . . . .	76
3.2	Disk Dynamics . . . . .	83
3.2.1	Forced Eccentricity and Longitude of Pericenter . . . . .	83
3.2.2	Disk Offset . . . . .	84
3.2.3	The Importance of Radiation Forces in Debris Disks . . . . .	85
3.3	Simulations . . . . .	89
3.3.1	The Method . . . . .	89
3.3.2	Simulated Debris Disks . . . . .	91
3.4	Results . . . . .	91
3.4.1	Interior Resonance . . . . .	93
3.4.2	Exterior Resonance . . . . .	98
3.5	Discussion . . . . .	100
3.5.1	Locating an Unseen Planet from Asymmetries in MMR Gaps . . . . .	100
3.5.2	Higher Order Resonances . . . . .	101
3.5.3	Determining Planetary Parameters . . . . .	102



Eccentricity . . . . .	103
Semimajor Axis . . . . .	103
Semimajor Axis from Multi-epoch Observations . . . . .	104
Mass . . . . .	105
3.5.4 Disk Offset and Peri/Apocenter Glow . . . . .	108
3.5.5 Simulating ALMA Observations . . . . .	109
3.6 Summary and Conclusions . . . . .	112
<b>4 Applying a Particle-only Model to the HL Tau Disk</b>	<b>118</b>
4.1 Introduction . . . . .	118
4.1.1 Hydrodynamic Studies of HL Tau to Date . . . . .	120
4.2 Method . . . . .	125
4.2.1 The HL Tau Disk Profile . . . . .	125
4.2.2 Simulations . . . . .	125
4.2.3 Fitting . . . . .	126
4.2.4 Uncertainties . . . . .	128
4.3 Results . . . . .	129
4.3.1 MMR Gaps in the HL Tau Disk . . . . .	133
4.4 Summary and Conclusions . . . . .	135
<b>5 Summary, Conclusions, and Future Prospects</b>	<b>141</b>
5.1 Summary and Conclusions . . . . .	141
5.2 Future Prospects . . . . .	145
<b>A Orbital Elements</b>	<b>149</b>
A.1 Semimajor Axis ( $a$ ) . . . . .	149
A.2 Eccentricity ( $e$ ) . . . . .	150
A.3 Inclination ( $i$ ) . . . . .	151
A.4 Longitude of the Ascending Node ( $\Omega$ ) . . . . .	151
A.5 Argument of Pericenter ( $\omega$ ) . . . . .	152
A.6 True Anomaly ( $\nu$ ) . . . . .	152
<b>Curriculum Vitae</b>	<b>155</b>

# List of Figures

1.1	Evolution of a circumstellar disk after the collapse of a giant molecular cloud core. . . . .	2
1.2	The Spectral Energy Distribution (SED) of the star FX Tau and the IR excess from its circumstellar disk. . . . .	4
1.3	Gaps in the SEDs of the disks around HK Tau, T Tau O, RY Tau, and SU Aur, explained as being due to tidal effects of a companion star or a planet. . . . .	6
1.4	ALMA’s high resolution images of disks around HL Tau and HD 163296, revealing a series of concentric gaps likely due to planets sweeping up their orbits. . . . .	7
1.5	Simulations showing the minimum mass of a planet around a 1.3 $M_{\odot}$ star that can open a gap in gas distribution and in mm dust. . . . .	8
1.6	The planet-forming disk around the nearby star TW Hydrae observed by HST and ALMA, showing gaps likely carved out by planets. . . . .	10
1.7	The observed polarized intensity profile of the disk around TW Hydrae. . . . .	11
1.8	ALMA’s high resolution image of the disk around HL Tauri, revealing multiple gaps. . . . .	12
1.9	Simulations of disks showing the effect of disk inclination with respect to the plane of the sky on gap structures, assuming the disks are observed at the wavelength of 10 $\mu m$ . . . . .	14
1.10	Same as Figure 1.9 but at $\lambda = 0.1 mm$ . . . . .	15
1.11	Disk asymmetries observed in LkH $\alpha$ 330, SR 21N, and HD 135344B due to disk inclination and possible tidal effects by unseen planets. . . . .	16
1.12	Evolution of a circumstellar disk from primordial to debris disk via homologous depletion and inside-out clearing. . . . .	18

1.13	Spiral patterns in the transitional disk of SAO 206462 taken in near-IR scattered light using the Subaru telescope. Such patterns may give clues to the presence of nearby planetary bodies. . . .	19
1.14	Schematic illustration of the Poynting-Robertson (PR) effect. . .	22
1.15	Schematic illustration of the orbits of dust fragments of various sizes. . . . .	23
1.16	Clumpy structure observed in Fomalhaut’s disk, providing first clues to the presence of a planet. . . . .	26
1.17	HST image of the warped inner disk of $\beta$ Pictoris, caused by a planet inclined to the disk. . . . .	27
1.18	Shadow cast by the warped inner disk of TW Hydrae caused by an inclined planet. . . . .	28
1.19	Distribution of Solar System’s Main Belt asteroids in semimajor axis, showing the Kirkwood gaps at mean-motion resonances with Jupiter. . . . .	30
1.20	Conceptual illustration of the three planetesimal belts around the star $\beta$ Pictoris. . . . .	32
2.1	Orbits of known Solar System asteroids at or interior to Jupiter’s as of June 2015, showing that MMR gaps may not be revealed through a telescopic image of <i>some</i> disks due to the smearing effects of asteroid eccentricities. . . . .	44
2.2	Maximum libration widths for 2:1, 3:2, and 3:1 Main Belt resonances with Jupiter. . . . .	46
2.3	Simulation showing interior resonance structures at 2:1 MMR (double arc) formed by interactions of planetesimals in the disk with a $4.0 M_J$ planet on a circular orbit and particle distributions in heliocentric distance. . . . .	52
2.4	Same as Figure 2.3 but with planet’s eccentricity increased to $e = e_J = 0.0489$ . An extra gap appears at the 3:1 MMR. . . . .	53
2.5	Structures formed by exterior resonance interactions of planetesimals with a $4.0 M_J$ planet on a circular orbit interior to the disk. The gap formed at exterior 2:1 MMR is a single arc. . . . .	55
2.6	Same as Figure 2.5 but with planet’s eccentricity increased to $e = e_J = 0.0489$ . An extra gap appears again at 3:1 MMR with the planet. . . . .	56

2.7	Gaps at 2:1 and 3:1 MMR formed by a $1.0 M_{\oplus}$ planet on circular orbit exterior to the disk. The gaps are too narrow to be observed in the simulated disk and can only be revealed when a histogram of particle distributions is made. . . . .	59
2.8	Comparison of analytical and simulated libration widths versus planet mass for interior and exterior 2:1 resonance with a planet having $e = 0.0$ and $e = 0.0489$ . . . . .	60
2.9	The effect of planet's mass and eccentricity on the resonant location for the 2:1 interior and exterior MMR. . . . .	63
2.10	The shift in gap location versus the planet's mass for the 2:1 interior and exterior MMR with planet eccentricities $e = 0.0$ and $e = 0.0489$ . . . . .	65
2.11	Spiral patterns formed in simulated disks with planet on a non-circular orbit. These may be forced eccentricity waves originating at Lindblad resonances. . . . .	67
2.12	MMR gap contrast vs. planet's mass for 2:1 interior and exterior resonances. . . . .	68
2.13	Same as Figure 2.3(a) for interior resonance except that particles in $x$ and $y$ are binned and assigned a color based on the total emission from each bin, normalized to the peak intensity . . . .	70
2.14	Same as Figure 2.13 but for the case of exterior resonance. The same disk is shown in Figure 2.5(a). . . . .	70
3.1	Comparison of the Poynting-Robertson inspiral timescales to the collisional lifetimes of dust particles in a debris disk. . . . .	89
3.2	Simulation result illustrating interior 2:1 and 3:1 MMRs with a single planet of mass $M = 3.0 M_J$ and eccentricity $e = 0.1$ . . . .	95
3.3	Distribution of particles shown by Figure 3.2 but in semimajor axis instead of heliocentric distance. . . . .	96
3.4	Interior resonance gaps formed by interaction of disk particles with a planet of mass $M = 1.0 M_J$ and $e = 0.3$ and particle trapping at 3:2 MMR. . . . .	97
3.5	Same as Figure 3.4 but with $M = 6.0 M_J$ and $e = 0.1$ . . . . .	98
3.6	Same as Figure 3.2 with mass $M = 3.0 M_J$ and eccentricity $e = 0.1$ but with the perturber interior to the disk. . . . .	99

3.7	Interior MMR with a planet of mass $6 M_J$ and eccentricity 0.2 and the formation of a higher order (4:1) MMR gap. . . . .	102
3.8	Change in MMR libration width with planet mass for 2:1 and 3:1 resonance with a planet exterior to the disk (i.e. interior resonance). . . . .	106
3.9	Same as Figure 3.8 but for exterior resonance. . . . .	107
3.10	CASA simulated observations of disks shown by Figures 3.2(a) and 3.6(a). . . . .	111
3.11	Surface brightness profile of the disk shown in Figure 3.10(a) along the major axis. . . . .	112
4.1	Comparison between the radial profile of the HL Tau disk observed by ALMA and our simulation using a single power-law profile in dust density distribution. . . . .	130
4.2	Same as Figure 4.1 but with two different power-law indices for dust surface density distribution with a slope break beyond the orbit of the outermost planet. . . . .	131
4.3	Uncertainty calculations at $2\sigma$ confidence level for the masses of the three planets in the HL Tau disk. . . . .	131
4.4	Comparison between ALMA's (deprojected) image of the HL Tau disk with a CASA simulated image drawn from our best-fit parameters. . . . .	135
A.1	Orbital elements describing the size, shape, and orientation of any Keplerian orbit. . . . .	153

# List of Tables

3.1	Equations relating the mass of a perturber having various orbital eccentricities to the observed width of a gap at the 2:1 and 3:1 interior and exterior MMR drawn from our measurements of gap widths. . . . .	107
4.1	Estimated locations and masses of possible planets forming HL Tau's 5 major gaps found in the literature. . . . .	124
4.2	The best-fit parameters and uncertainties obtained using the downhill simplex method for the semimajor axes and masses of the three planets that are likely responsible for sculpting the prominent gaps of the HL Tau disk as well as the range of values proposed by others. . . . .	132

# List of Appendices

Appendix A Orbital Elements . . . . .	149
---------------------------------------	-----

# Chapter 1

## Prelude

### 1.1 Introduction

Planets form from the same cloud of gas and dust that gives birth to a star. While the bulk of the gas falls into the central stellar body, conservation of angular momentum forces some of the material into orbit around it, and it is in this circumstellar disk that planet formation takes place. Circumstellar disks are typically depleted over time but can persist around stars to different degrees throughout their lifetimes. This has led to studies of the structure and evolution of these disks at every stage in the hopes of better understanding planet formation. This thesis has as its primary goal to illuminate the link between circumstellar disks and planets.

These disks are dominated by gas and sub-micron size dust at the early stages of star formation. The small dust particles continually collide to form larger grains which eventually seed planets. As the star is born at the center of the swirling cloud of gas and dust that once collapsed under its own gravity, the gas is blown away by the strong stellar winds. This important process turns the disk from a gas-rich ‘protoplanetary disk’, into a ‘pre-transitional’ and then a ‘transitional’ disk, and finally into a gas-poor but dust-rich ‘debris disk’ (see Figure 1.1). Though the present work focuses mostly on this final stage, understanding how we know what we know about circumstellar disks in general as well as the structures observed in protoplane-



tary disks, as the precursors of debris disks, is essential in our study of structures in gas-poor disks.

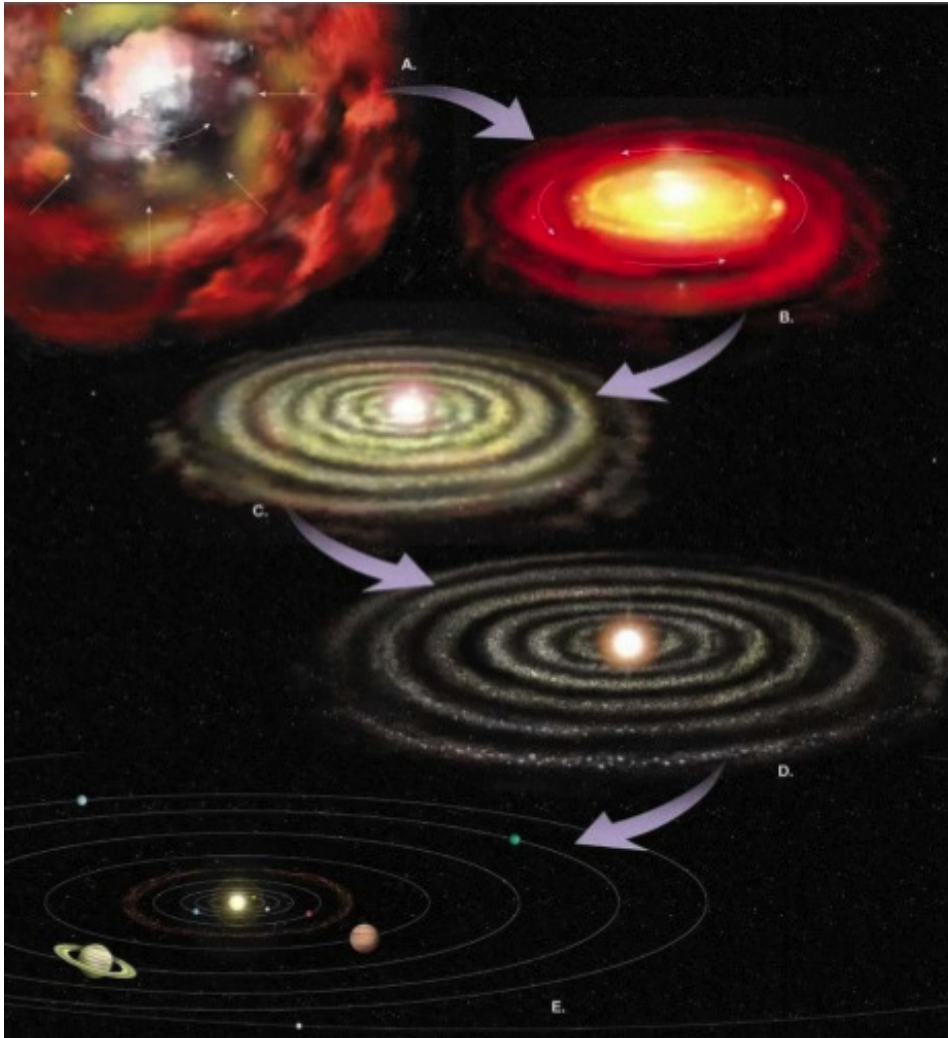


Figure 1.1: Evolution of a circumstellar disk after the collapse of a giant molecular cloud core. The disk evolves from being gas-rich to gas-poor over the course of  $\sim$  a billion years. Credit: Pearson Prentice Hall Inc.

Therefore, we start in this chapter by outlining structures formed in circumstellar disks at each stage. Sections 1.2.1 and 1.2.2 review observational signatures of annular gaps and azimuthal asymmetries for a few protoplanetary disks as well as simulations that attempt to illustrate geometrical effects as one possible source of the observed asymmetry in the disk structure. Next comes a brief discussion of the disk as it transitions from being gas-rich to gas-poor, a phase in which the disk is referred to as “transitional” (Section 1.3) before we finally

get to the last stage in which little or no gas remains (Section 1.4).

Once we establish what is already known about disk structures, in the subsequent chapters we shift our focus to structures formed in debris disks via a mechanism known as “Mean-Motion Resonance” (MMR) and how such structures could be useful to not only detect but also characterize extrasolar planets. This is what will be outlined in Chapters 2 and 3 where we examine the gravitational perturbation of the disk by a planet on a nearly circular (zero or low eccentricity)<sup>1</sup> orbit and one in which the planet has a range of moderate orbital eccentricities. In each case, we will present a means of determining the mass as well as some orbital parameters of the planetary perturber from the disk structure and illustrate how detection of MMR gaps can be used in the study of planets beyond our Solar System.

Finally in Chapter 4, we take our dynamically simple model of gap formation in debris disks and apply it to structures in a protoplanetary disk, HL Tauri, in order to address the question of whether such simple models can inform the study of these systems or if a complicated hydrodynamic model is required. A summary and conclusions are provided in Chapter 5 along with some outstanding questions for future research.

## 1.2 Protoplanetary and Pre-Transitional Disks

Stars spend most of their lives in a stable state, a condition referred to as being ‘on the *main sequence*’, after an earlier turbulent phase of gravitational collapse from an interstellar gas cloud. It is now well established that protoplanetary disks form around most pre-main sequence (PMS) stars, and that these disks are the birthplace of planets. Earliest indirect observational clues to the existence of disks around PMS stars came from detecting excess infrared and submillimeter emission in the Spectral Energy Distributions (SEDs) of sources observed with near- and mid-infrared photometry (see Figure 1.2). The star itself produces a black-body spectrum peaked at optical wavelengths, but is much fainter in the infrared. The ‘excess’

---

<sup>1</sup>‘Eccentricity’ is one of the *orbital elements* used to describe the orbits of particles around a central body. A brief outline of orbital elements appears in Appendix A.

infrared flux observed comes from the reprocessing of optical photons by dust near the star.

A study by Strom et al. (1989) revealed that at least 60% of the Solar-type stars in their sample of 83 PMS stars exhibit significant near-IR excess emission. Their findings were later confirmed when in 1993 a team led by Robert O'Dell of Rice University used the Hubble Space Telescope (HST) to directly image stars in the Orion Nebula, and revealed that nearly half of those stars are surrounded by circumstellar disks of gas and dust (O'dell et al., 1993).

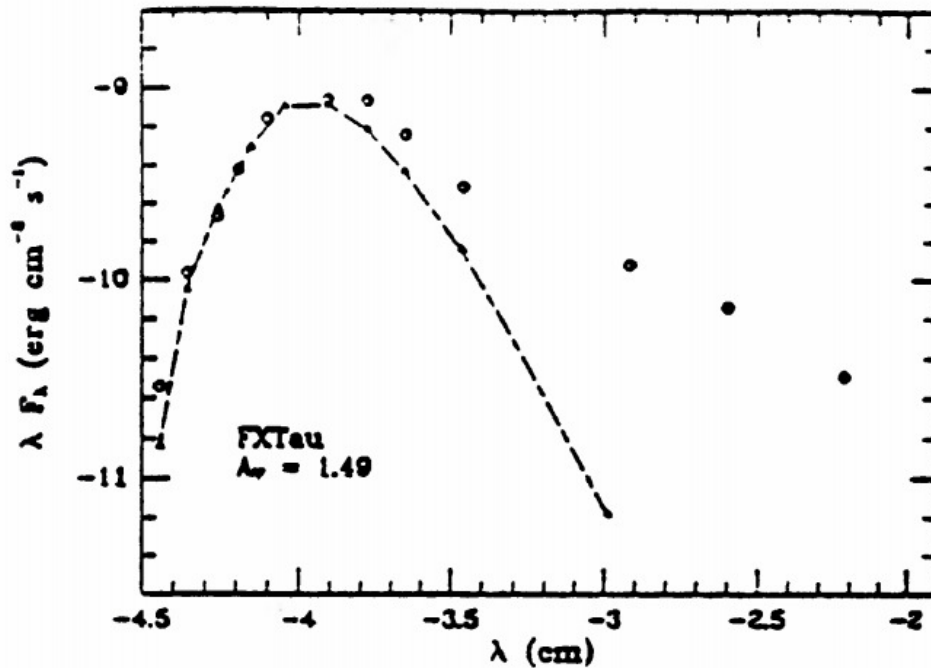


Figure 1.2: The IR excess in the Spectral Energy Distribution of the star FX Tau was identified as being due to the presence of a circumstellar disk around this young T-Tauri star whose blackbody emission is shown by the dashed curve. The excess IR emission at the right of the figure cannot be explained by the star itself. Credit: Strom et al. (1989).

Following the discovery of disks around PMS stars by Strom et al. in 1989, Skrutskie et al. (1990) combined fluxes measured using the Infrared Astronomical Satellite (IRAS) and NASA's Infrared Telescope Facility (IRTF) to reveal inner disk holes and outer gaps in these disks. This suggested that some disks were undergoing a transitional phase from being optically thick to a state in which most of the disk has been dissipated, possibly due to agglomeration of disk material into planets. The existence of annular gaps in these so-called 'pre-transitional

disks’ — optically thick disks that have optically thin gaps — have since been confirmed observationally, with some even being directly imaged at near-IR and millimeter/submillimeter wavelengths.

A year before first protoplanetary disks were directly imaged by HST in 1993, SED analysis of these disks had also indicated the presence of gaps. In a study by Marsh & Mahoney in 1992, the authors observed what they described as “a range of ‘missing’ temperatures” in the SEDs of HK Tau, T Tau O, RY Tau, and SU Aur (see Figure 1.3) consistent with sculpting of the disks by companion stars or planets (Marsh & Mahoney, 1992). This reinforced the notion that protoplanetary disks are indeed the cradles of planets, as their name suggests.

Planet formation does not always result in the removal of disk material and gap formation, but can sometimes trigger density enhancements in the disks and appear as complex features such as spiral patterns and dust traps. The spiral arms observed in some protoplanetary disks are explained as being driven by spiral density waves due to gravitational perturbations of a massive planet or a stellar companion (e.g. Muto et al., 2012; Brown et al., 2009). On the other hand, some protoplanetary disks such as IRS 48 show asymmetric concentration of dust grains on one side of the disk which is likely due to a companion triggering an azimuthal gas pressure bump that results in trapping the dust particles (van der Marel et al., 2013). Understanding the origin and evolution of such density enhancements is also important in the context of planet formation and evolution; however, the present study intends to focus on the scenarios that explain the *removal* of disk material and the development of gaps in disks, particularly as they relate to disk-planet interactions. Note that gaps developed in circumstellar disks by interaction with planets are not necessarily caused by the *removal* of disk particles, but can be the result of a significant change in the particles’ orbits. We will return to this in Chapter 3.

As technology advances, gaps in protoplanetary disks are now frequently revealed. These gaps are often found to be azimuthally symmetric and are believed to have been formed as the newly formed planets sweep up the material in their neighborhood while orbiting the star at the center of the disk. The astonishingly detailed image of the disk around HL Tauri which was

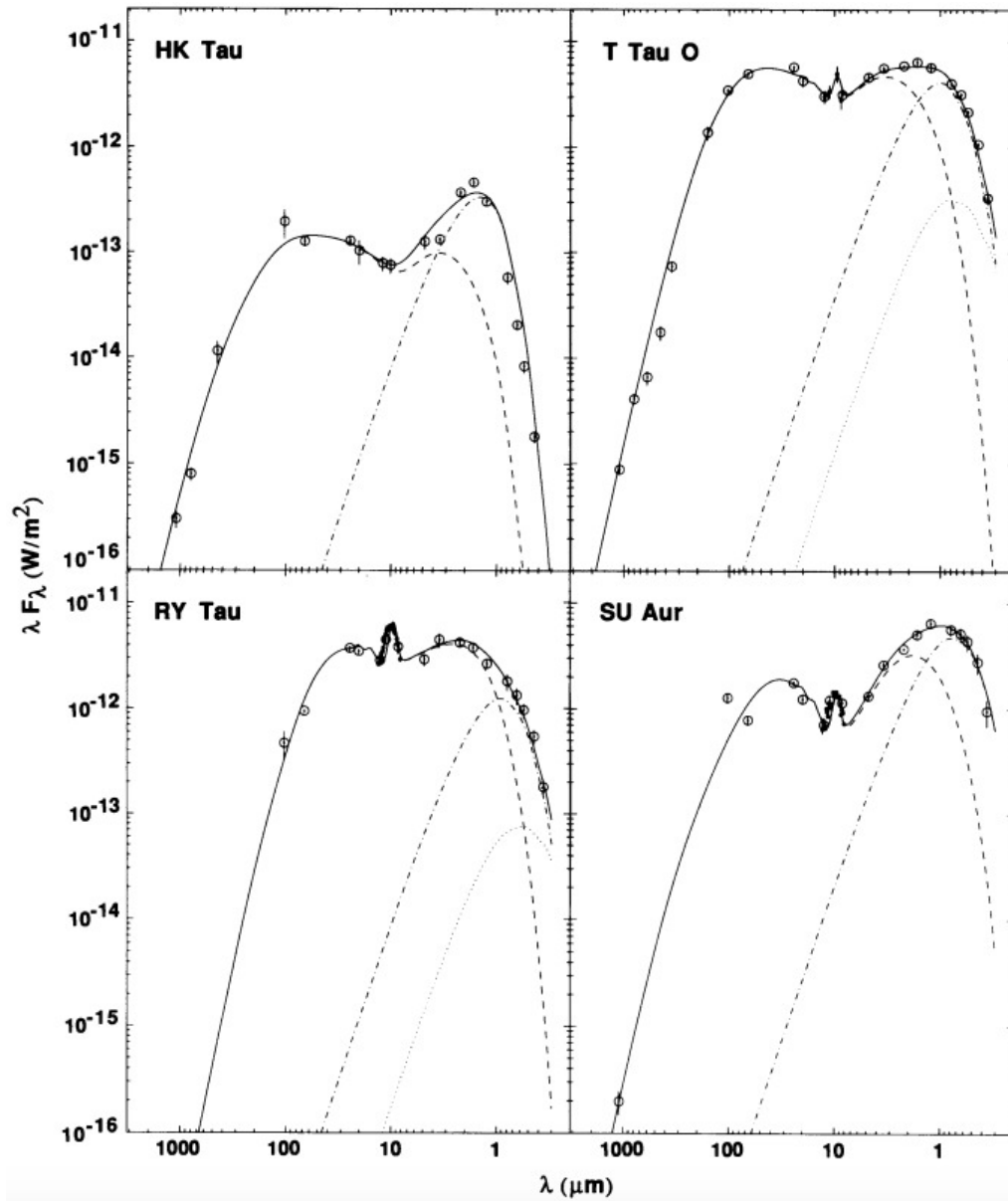


Figure 1.3: The appearance of discrete gaps in the SEDs of the disks around HK Tau, T Tau O, RY Tau, and SU Aur are explained as being due to tidal effects of a companion star or a planet. The solid curves represent the best-fit model to the data (the circles with error bars) while the dashed and the dot-dashed curves show the contributions of the disk and the star to the total flux, respectively. These four stars are believed to still be accreting mass from their circumstellar disks; and the dotted curves show the SED of the boundary layer between each accreting star and the accretion disk. Credit: Marsh & Mahoney (1992).

made by the *Atacama Large Millimeter/submillimeter Array* (ALMA) and released in November 2014, shown by the left panel of Figure 1.4, is by far the best example showing gap structures (likely induced by planets) in a protoplanetary disk and can help better understand the processes that go into formation and evolution of planetary systems (see NRAO, 2014). More recently in December 2016, ALMA released the image of another protoplanetary disk also with ring-like structures around the star HD 163296, shown by the right panel of Figure 1.4, that are believed to be sculpted by two Saturn-mass planets currently forming in the disk (NRAO, 2016b). Considering how young HL Tau and HD 163296 are believed to be (1 and 5 million years, respectively), images like these have surprised astronomers as planet formation was not expected to begin at such an early stage after the formation of protoplanetary disks since it had previously been expected that planets typically take a few tens of million years to form (see Encrenaz et al., 2004). We note that the planets themselves are not visible in the images, but are inferred from the structures they produce in the disk; the idea that disks may encode information about planets that are otherwise too faint to detect is one we will return to.

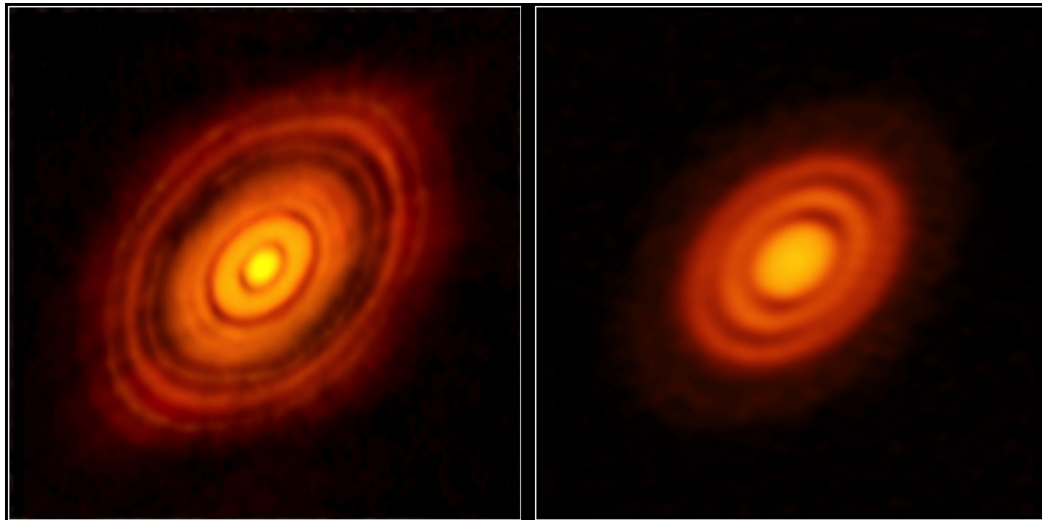


Figure 1.4: Left: As part of its science verification phase, ALMA captured this image of the disk around HL Tauri, a Sun-like star located 450 light-years away in the constellation Taurus. This is the most detailed image ever taken of a disk, revealing structures that likely serve as nurseries for planet formation. Credit: NRAO (2014). Right: A more recent ALMA image of a protoplanetary disk around HD 163296 shows similar ring structures believed to have been formed by two proto-Saturns. Credit: NRAO (2016b).

A recent study by Price et al. (2017) shows that a planet with mass as low as 0.1 Jupiter-mass ( $M_J$ ) can change the distribution of dust in a protoplanetary disk by pushing dust particles away which could get trapped in mean-motion resonances and form bright rings around a dark gap in dust emission. However, the same study suggests that a gas gap can only develop in the disk if the planetary mass is at least  $1 M_J$  (see Figure 1.5).

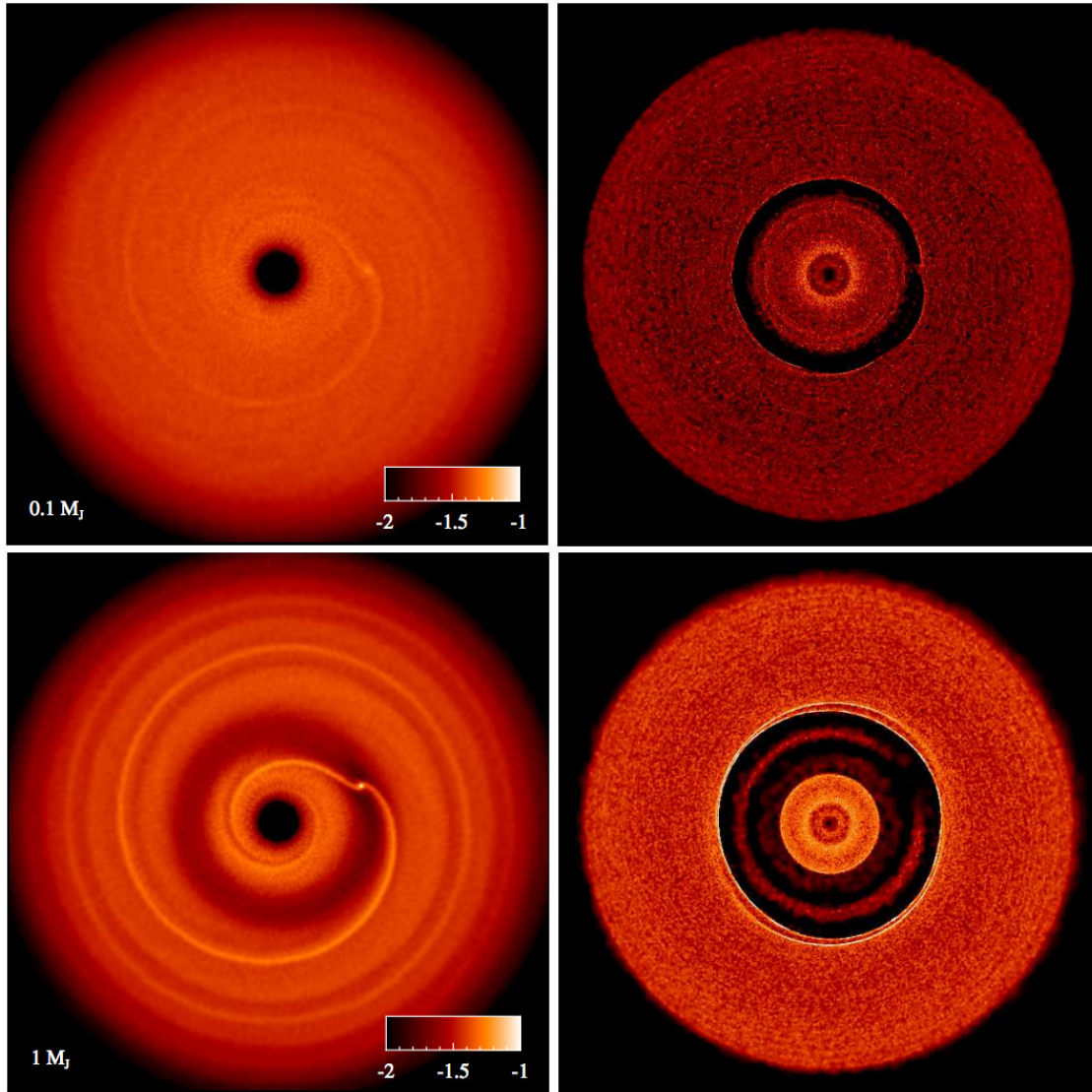


Figure 1.5: Simulations showing the minimum mass of a planet around a 1.3 Solar-mass ( $M_\odot$ ) star that can open a gap in gas distribution (left) and in mm dust (right). While a  $0.1 M_J$  planet can significantly affect the surface density of dust and form a gap in its vicinity, a planet at least 10 times more massive is required to form a gap in gas distribution, as shown by the top and bottom panels, respectively. Credit: Price et al. (2017).

In addition to symmetric gaps, observations have also revealed that asymmetric structures are common features of gaps in protoplanetary disks and are interpreted as being either due to density perturbations of a stellar or planetary companion or have a geometric nature as will be discussed in Section 1.2.2. This thesis is particularly concerned with the formation of asymmetric structures in circumstellar disks, and the multitude of information that they reveal about planets near them. As a result, we will introduce in some detail the different phenomena which can affect the distribution of gas and/or dust within disks, and particularly gap formation, at different stages of their evolution. Thus we will start the next section by discussing two protoplanetary disks imaged in the recent years that show very detailed structures potentially made by planets before we turn to a discussion of the observed asymmetries in protoplanetary disks.

### 1.2.1 Observed Disk Structures: Annular Gaps

Dynamical clearing by a giant planet or a low mass stellar companion has been proposed as a mechanism that likely explains the presence of gaps in protoplanetary disks. Here we will discuss two examples of symmetric gaps observed in disks around TW Hydrae and HL Tauri that are likely indicative of planet formation in these disks.

#### **TW Hydrae**

Multi-wavelength observations of the young ( $\sim 10$  million year-old) pre-main sequence star, TW Hydrae have revealed a disk extending to  $\sim 150 - 230$  AU around this M2 star (see for instance, Weinberger et al., 2002; Apai et al., 2004; Qi et al., 2004; Roberge et al., 2005; Andrews et al., 2012) with a gap approximately 2 AU wide which has also been imaged using Hubble Space Telescope's high contrast direct imaging (see left panel of Figure 1.6) and was found to be likely due to a sub-Saturn mass planet (Debes et al., 2013). In March 2016 the National Radio Astronomy Observatory (NRAO) released an image of the TW Hya disk taken by ALMA (shown by the right panel of Figure 1.6), placing the two prominent gaps revealed



in this image 20 and 40 AU from the star. ALMA's unprecedented image of this protoplanetary disk also revealed an inner gap as close as 1 AU from the star, making TW Hydrae strikingly similar to a young Solar System with 3 potential planets at distances similar to those from Uranus, Pluto and the Earth to the Sun.

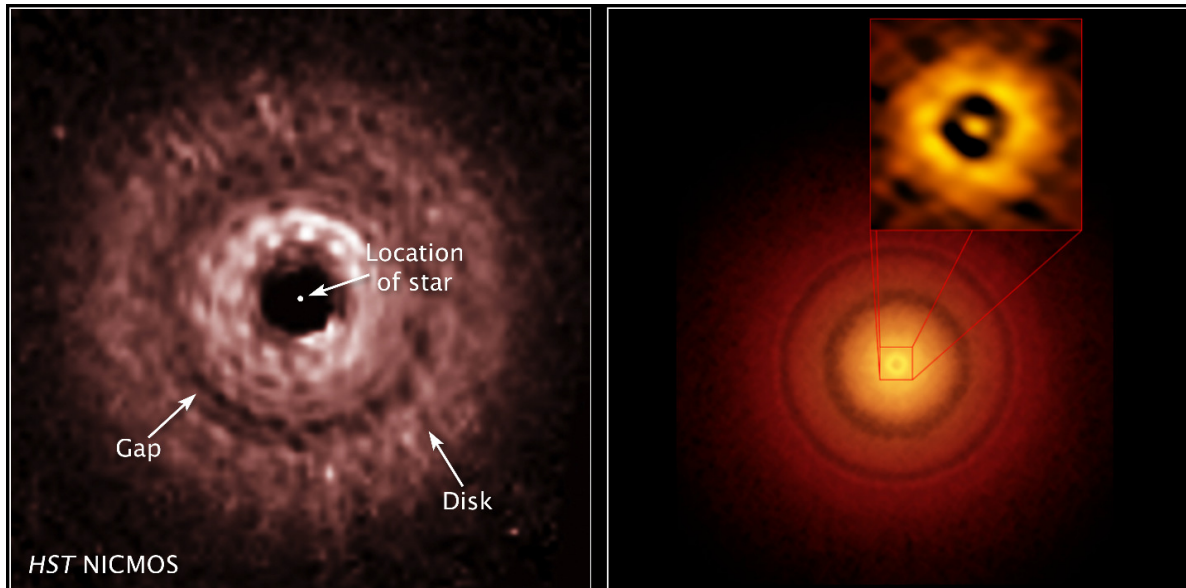


Figure 1.6: The planet-forming disk around the nearby star TW Hya ( $\sim 175$  light-years away) as seen in 2005 by HST (left) and in 2016 with ALMA (right). ALMA's high resolution image shows three gaps in the disk, likely formed by the gravitational clearing of at least three planets around this red dwarf star. The innermost gap (zoomed-in) is believed to be as close to the star as the Sun-Earth distance. Credit: NASA, ESA, and Debes et al. (2013) (the HST image) and NRAO (2016a) (the ALMA image).

Using a new high-contrast H-band ( $1.6 \mu m$ ) polarized intensity (PI) image of the TW Hydrae disk, Akiyama et al. (2015) had also been able to detect the gap at 20 AU which appeared as a clear ring-like PI depression (see Figure 1.7). The authors proposed that the gap is likely formed by a planet in the disk, though again we note that in none of these images has the planet been directly imaged.

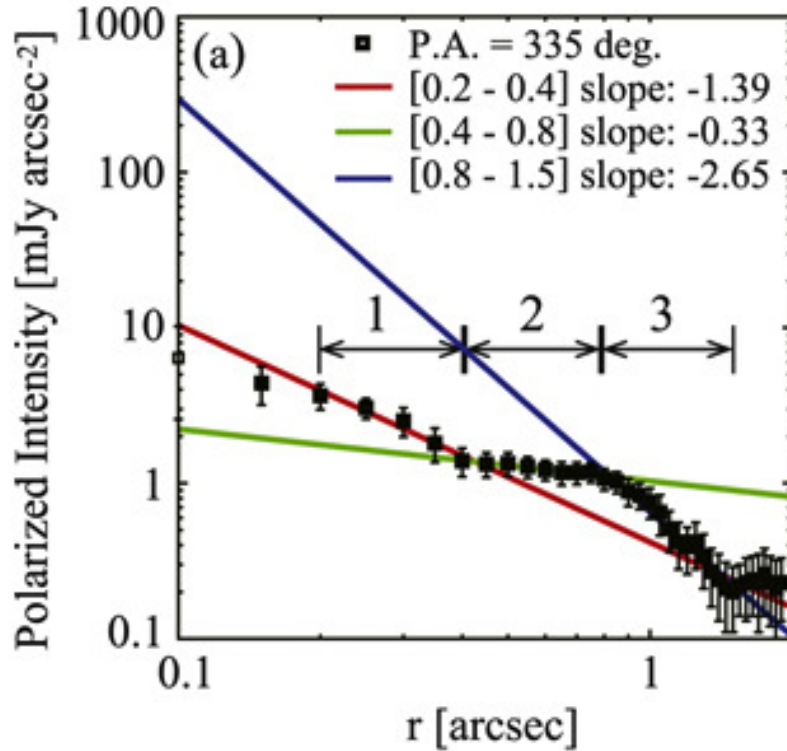


Figure 1.7: The observed PI profile of the disk around TW Hydrae. Three major zones have been defined as step transitions: Zone 1 ( $0.''2 \leq r \leq 0.''4$ ), Zone 2 ( $0.''4 \leq r \leq 0.''8$ ), and Zone 3 ( $0.''8 \leq r \leq 1.''5$ ) with power-law fits in each zone shown in red, green, and blue, respectively. The change in slope at  $\sim 0.''4$  could be the result of a planet-induced gap at  $\sim 20$  AU. The change in slope around  $0.''8$  is explained by Apai et al. (2004) as possibly being due to a change in the disk's surface density or the change in the flaring angle. Credit: Akiyama et al. (2015).

## HL Tauri

ALMA's recent image of the disk around HL Tau, which was made as part of its science verification process and was released in November 2014, is undoubtedly the most detailed observational evidence of gaps in a protoplanetary disk ever obtained (see NRAO (2014) and Figure 1.8). Tamayo et al. (2015) argued that the concentric gaps revealed in the ALMA image of HL Tau are most likely carved out by planets as they sweep up their orbits of the remaining gas and dust. They also put constraints on the masses of the planets that form the most prominent gaps seen in the ALMA image (labeled 1 through 5 in Figure 1.8) and found a maximum mass of  $\sim 2$  Neptune masses for the outer three bodies if the planets are not in

mean-motion resonance, otherwise, the authors showed that the planets can reach at least the mass of Saturn. We will revisit the HL Tau disk in more details in Chapter 4.

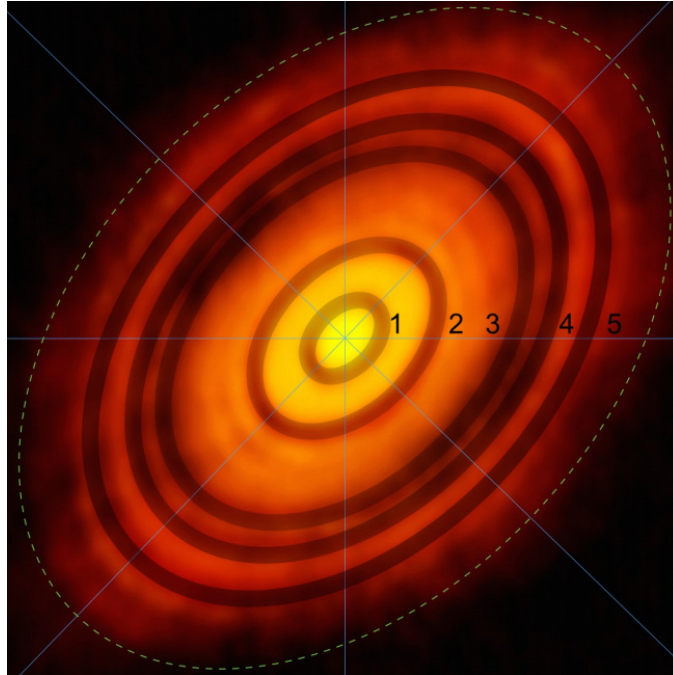


Figure 1.8: Detailed structure of the disk around HL Tau released by ALMA in late 2014. The most prominent gaps are labeled 1 through 5 by Tamayo et al. (2015). Credits: ALMA (NRAO/ESO/NAOJ); C. Brogan, B. Saxton (NRAO/AUI/NSF).

### 1.2.2 Observed Disk Structures: Asymmetries

Studying the structure of protoplanetary disks revealed that gaps are not always azimuthally symmetric; rather azimuthal asymmetries turned out to be a common feature of such disks and gaps with asymmetric azimuthal profiles such as those having horseshoe morphologies have been observed.

A planet that is in the process of accreting mass is thought to be one mechanism that explains the observed asymmetries in protoplanetary disks. As accretion happens onto a planet, the planet pulls the disk material from the surface of the disk to the disk's mid-plane, compressing the disk in the vertical direction. This can produce a shadow in the scattered light and a dip in disk brightness (Jang-Condell, 2009). On the other hand, Kraus et al. (2013) proposed

that a close stellar-mass companion can also distort the disk and form asymmetries.

Asymmetries in protoplanetary disks could also be due to geometric effects. An annular gap in a protoplanetary disk may show a non-axisymmetric structure depending on the disk's angle of inclination (with respect to the line of sight) as well as the wavelength with which it is observed. This is demonstrated by Jang-Condell & Turner (2013) who used simulations to show how the observed protoplanetary disk structures depend on the viewing angle as well as the wavelength of observation. They simulated images of protoplanetary disks at a range of wavelengths (1, 10, 30, 100, 300, and 1000  $\mu m$ ) and varying inclination angles ( $0^\circ$ ,  $30^\circ$ ,  $45^\circ$ ,  $60^\circ$ ). Their results indicated that disks that have ring-like gaps when viewed at  $0^\circ$  inclination (i.e. face-on), start to show horseshoe shaped gaps when they are tilted at various angles, making the near side of the disk to appear brighter in scattered light compared to the far side of the disk. However, the apparent asymmetry starts to diminish as the wavelength is increased to 0.1  $mm$  and longer since optical depth decreases with increasing wavelength. This is shown by Figure 1.9 (for  $\lambda = 10 \mu m$ ) and Figure 1.10 (for  $\lambda = 0.1 mm$ ).

In both figures, the top panels show simulations of disks without gaps while the middle and bottom panels show disks with gaps carved out by a planet of  $70 M_\oplus$  and  $200 M_\oplus$ , respectively, where  $M_\oplus$  denotes Earth's mass. Starting with  $0^\circ$  inclination in the left panels and moving to the right, the upper part of the disks is tilted away from the observer at  $30^\circ$ ,  $45^\circ$ , and  $60^\circ$ . Gaps start to become horseshoe-shaped as the disk is tilted in each case; however, comparison of the two figures at different wavelengths shows that the horseshoe morphology is more prominent when the disk is viewed using shorter wavelengths due to wavelength dependence of the disk's optical depth.

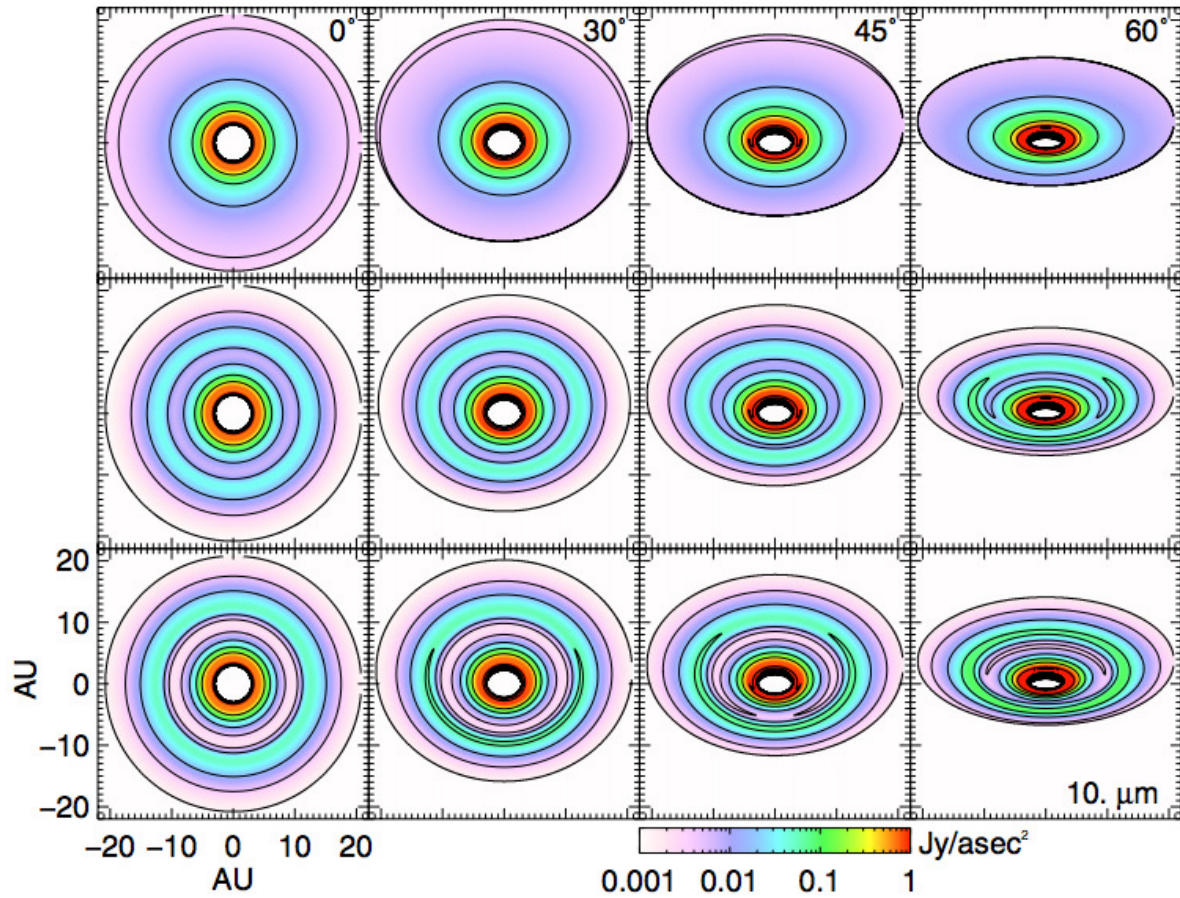


Figure 1.9: Simulated images at  $\lambda = 10 \mu\text{m}$  of disks without gaps (top) and with gaps due to a planet at 10 AU with  $M = 70 M_{\oplus}$  that opens a gap 0.56 deep and 1.1 AU wide (middle) and  $M = 200 M_{\oplus}$  having a depth of 0.84 and width of 1.7 AU (bottom). The inclination angle is increased from left to right. Contours are spaced by a factor of four in brightness (using the scale shown at the bottom). An annular gap is seen as having a horseshoe shape as the disk is tilted with respect to the line of sight. Credit: Jang-Condell & Turner (2013).

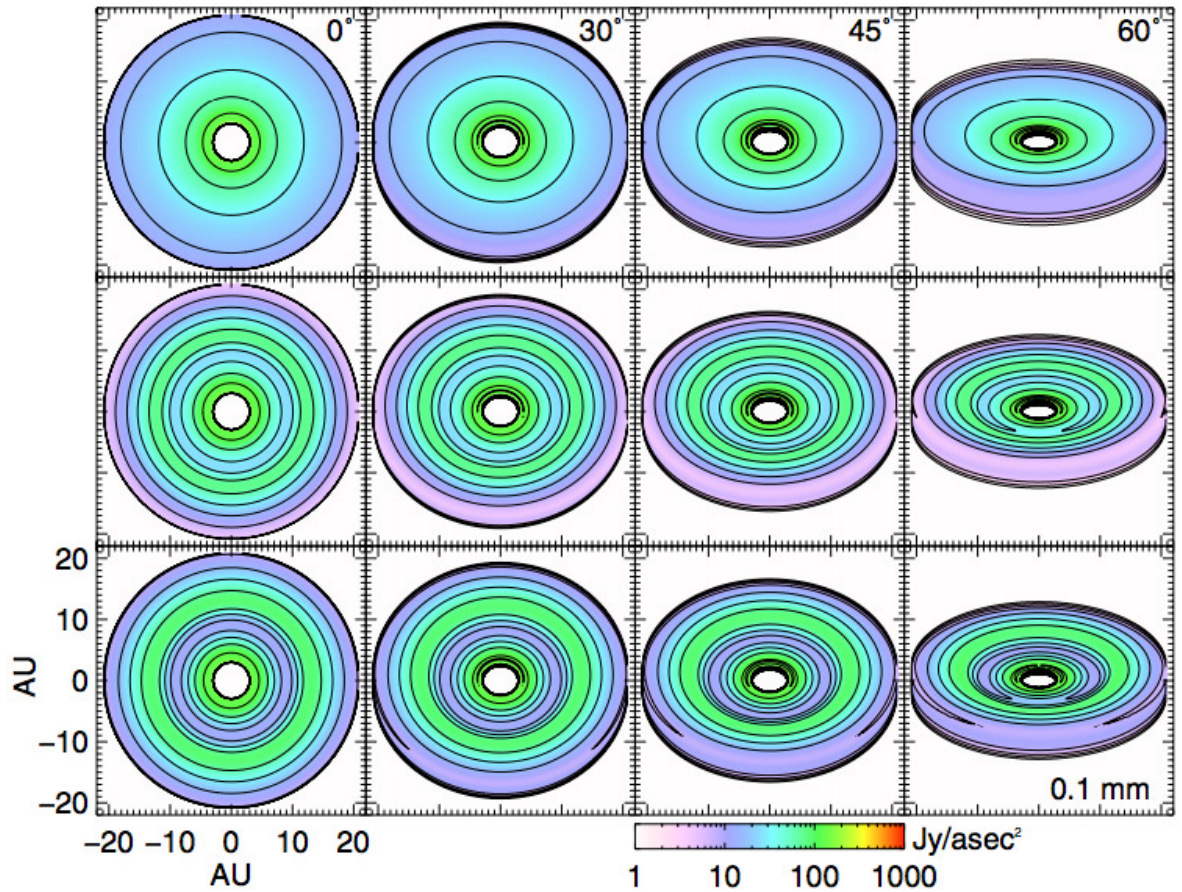


Figure 1.10: Same as Figure 1.9 but at  $\lambda = 0.1 \text{ mm}$  and contour spacing is by a factor of two in brightness. The horseshoe shape of the gap is less prominent when the wavelength is increased. Credit: Jang-Condell & Turner (2013).

The authors then applied their model to the pre-transitional disk around the T-Tauri star LkCa 15 that has already been found through its SED to have a gap between 5 and 46 AU (Espaillat et al., 2007). The disk's inner cavity has been directly imaged both in scattered light (Thalmann et al., 2010) and by radio interferometry (Andrews et al., 2011). More recently a protoplanet has even been directly imaged at a distance of  $\sim 20$  AU (Kraus & Ireland, 2012) from LkCa 15. The discovered planet is too far from the outer wall of the cavity at 46 AU to be responsible for gas and dust depletion; however, some authors speculate the possibility of one (or more) planetary-mass companions of 5 Jupiter-mass ( $M_J$ ) farther out that is responsible for shaping the cavity's outer wall (e.g. Espaillat et al., 2008; Bonavita et al., 2010). When their model was applied to the LkCa 15 disk, Jang-Condell & Turner (2013) were able to reproduce

the shape of the gap from direct observations of the disk with a disk that is inclined at  $52^\circ$ .

Brown et al. (2009) also reported asymmetries they observed in disks around HD 135344B, SR 21N and LkHa 330 (shown in Figure 1.11) as being mostly due to inclinations of the disks with additional contributions possibly from gravitational perturbations of a giant planet or a binary stellar companion.

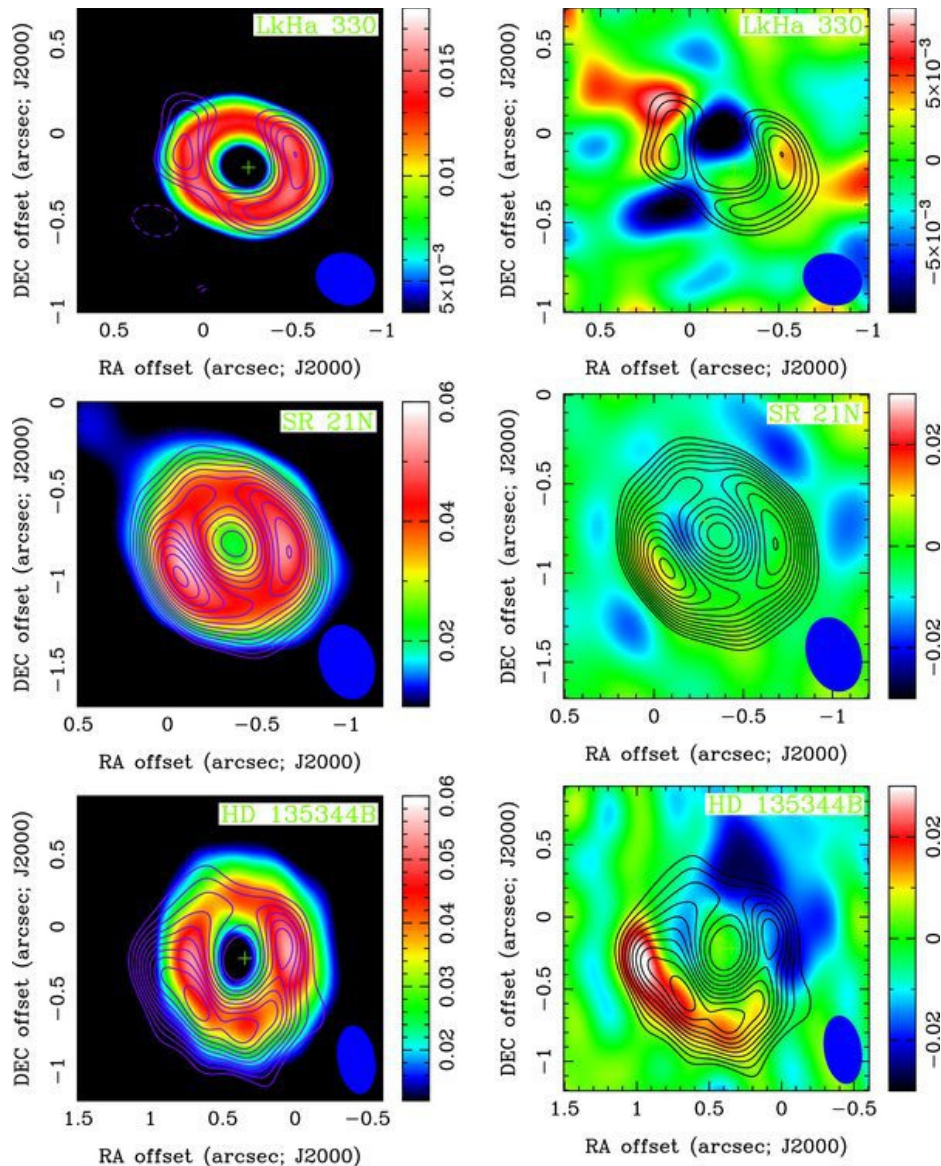


Figure 1.11: Asymmetries in the disks of LkHa 330 (top), SR 21N (middle), and HD 135344B (bottom). On the left are models of the disks at  $880 \mu\text{m}$  emission and  $1\sigma$  contours. The models are then subtracted from the data and the results are shown on the right. Inner cavities are found to have radii of 47, 33, and 30 AU, respectively, for the three disks. Credit: Brown et al. (2009).

In addition to the factors mentioned here that result in azimuthal asymmetries in disks, we will show in the chapters that follow that disk-planet gravitational interactions through mean-motion resonances could also form azimuthally asymmetric gaps.

## 1.3 Transitional Disks

Transitional disks are a relatively short-lived phase that bridge the gap between gas-rich, optically thick disks and the less luminous, optically thin debris disks that are free (or almost free) of gas. Unlike pre-transitional disks that show gaps between optically thick inner and outer parts, the central cavity of a transitional disk is almost completely devoid of gas and dust, though the outer regions are still optically thick. With stellar accretion coming to a halt, much of the disk's remaining gas at this point is either accreting onto the cores of what will eventually become gaseous planets or is about to be blown out by radiation from the newly born star. As photoevaporation starts to remove gas from the vicinity of the star, sub-micron sized dust particles quickly drain onto the star, creating an inner gas- and dust-free cavity that shows up as a dip in its SED.

As the small grains remain coupled to the gas and are removed from the disk, some could still survive if there is a planet of a few times Jupiter's mass or larger that is still accreting a gaseous envelope, according to a study by Owen (2014). The radiation pressure from the accreting planet that has already opened a gap in its surrounding would create a pressure bump, holding back some small dust grains in the outer disk. At slightly larger sizes, micron and mm-sized dust can also get trapped in the gas pressure bumps, resulting in a so-called "dust filtration" that is used to explain the observed asymmetries in dust distribution of transitional disks (see for instance, Rice et al., 2006).

Their short lifetime of only a few hundred thousand years (Espaillat et al., 2014) makes observations of these disks challenging. However, using their characteristic SEDs that exhibit a deficit of dust emission at short wavelengths ( $< 6 \mu\text{m}$ ) but strong excess emission at longer



wavelengths, a number of such disks have been identified (e.g, Hughes et al., 2007, 2009; Andrews et al., 2009, 2011; Balog et al., 2016). Using data from Spitzer Space Telescope, Balog et al. (2016) were able to identify 8 such disks that are undergoing a transitional phase in the open stellar cluster IC 2395. Combining their data from this open cluster with that from 19 other young ( $< 18$  Myr) clusters and associations, the authors concluded that though transitional disks are not as frequently found as disks around accreting T-Tauri stars and debris disks due to their short lifespan, their proportion depends on the age of the cluster and increases from  $(8.4 \pm 1.3)\%$  at  $\sim 3$  Myr to  $(46 \pm 5)\%$  at  $\sim 10$  Myr.

Also using the Spitzer data, a previous study by Currie (2009) suggested two different paths for disks to transition from primordial protoplanetary disks to debris disks. According to these authors, after only 2 to 5 Myr, depending on stellar mass, protoplanetary disks start showing signs of gas and dust dispersal via either an inside-out clearing by developing an inner hole or their gas is “homologously depleted”, meaning that the clearing occurs at various locations in the disk. This is shown schematically by Figure 1.12.

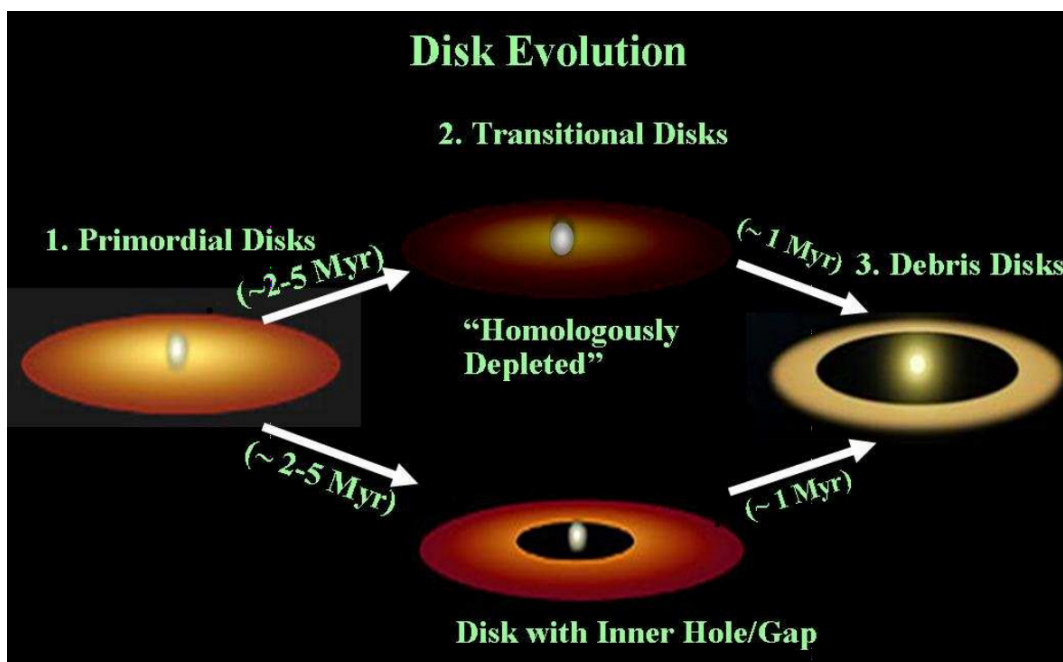


Figure 1.12: Evolution of a circumstellar disk from primordial to debris disk could follow one of two scenarios: gas and dust clearing at a range of disk locations (“homologous depletion”) or inside-out clearing and development of an inner cavity. Credit: Currie (2010).

Despite their short lifetime, some transitional disks have been observed directly in scattered light, such as the disk around SAO 206462 (see Figure 1.13). In addition to an inner cavity, this transitional disk exhibits two spiral arms, possibly excited by hidden planet(s) in the disk (see Muto et al., 2012). Using hydrodynamic and radiative transfer models, Fung & Dong (2015) argued that the mass of the planet that could be launching such spiral patterns in the SAO 206462 disk may be constrained from the azimuthal separation of the two arms and found it to be  $\sim 6 M_J$ .

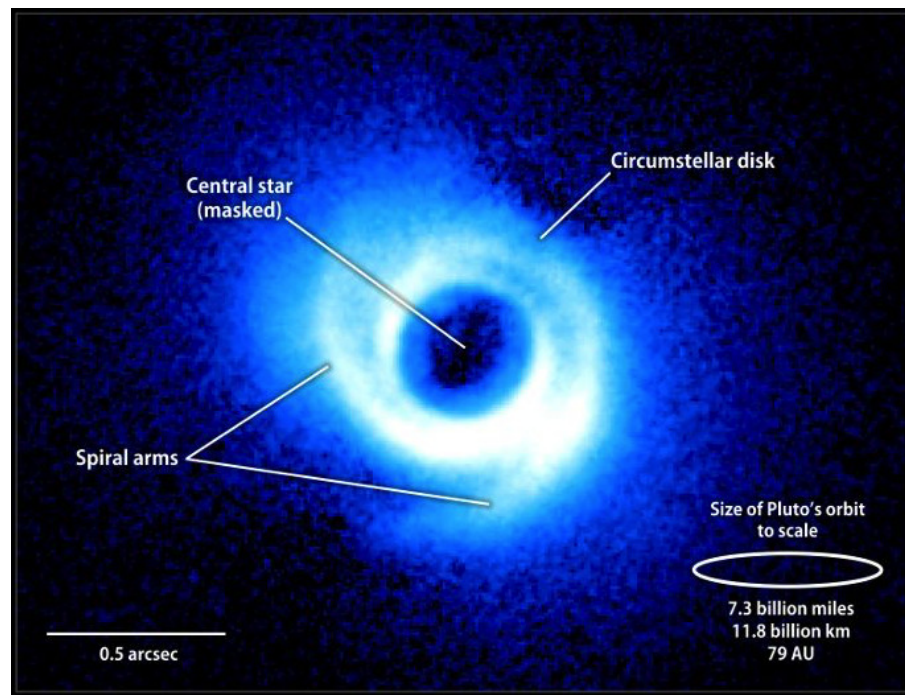


Figure 1.13: Spiral patterns revealed in the transitional disk of SAO 206462 in near-IR scattered light using the Subaru telescope may be explained as density variations due to the presence of planetary bodies in the disk. The mass of a planet that could have potentially formed these spiral arms is estimated by Fung & Dong (2015) to be  $\sim 6 M_J$ . Credit: NAOJ, Subaru, and Muto et al. (2012).

‘Giant planets’ like Jupiter, Saturn, Uranus and Neptune in our Solar System, are formed from large amounts of hydrogen and helium gas. This gas starts dissipating in a transitional disk, marking the end of the giant planet formation phase. Studying their structures and the mechanisms by which the gas and small dust in these disks are dissipated helps understand

how and when giant planet formation stops. They would also hold the key to the missing piece of the disk evolution just as it transitions from being gas-rich to a gas-poor disk. In the next section, we shall briefly go over this final stage in the disk evolution before we discuss in detail how the present study attempts at using structures in such disks to glean information about planets beyond the Solar System.

## 1.4 Debris Disks

Debris disks represent a later stage of disk evolution, about 10 Myr after the collapse of the molecular cloud core, in which most, if not all, of the gas in the disk is blown away by stellar radiation, leaving behind a disk of solid material that range in size from dust grains of a few micrometer in radius through large planetesimals whose radii reach hundreds of kilometers, to full-fledged planets.

First evidence of the existence of a debris disk outside the Solar System came in 1983 when analysis of the SED of the main-sequence star Vega using *IRAS* revealed a strong infrared excess beyond  $12 \mu\text{m}$  which was explained as originating from thermal radiation from solid particles larger than  $1 \text{ mm}$  (Aumann et al., 1984). This finding was observationally confirmed a year later when Smith & Terrile (1984) directly imaged a debris disk around the young main sequence star,  $\beta$  Pictoris with more discoveries of extrasolar debris disks made in the years that followed. More than a decade later, a study by Plets & Vynckier (1999) also using *IRAS* showed that about 13% of all main sequence stars within 25 parsec (pc) of the Sun display the “Vega phenomenon”, meaning that they harbor debris disks, with radial extents of tens to even hundreds of astronomical units and overall masses of  $0.01 - 0.1 M_{\odot}$ .

Debris disks are often observed through the infrared radiation emitted by dust. The smaller dust is either blown out of the system by radiation pressure (sub-micron sizes) or spirals into the star due to Poynting-Robertson (PR) drag on short timescales, effects that will be described below. As a result, dust must be continuously replenished through collision (or tidal disruption)

of the larger bodies. For instance, the lifetime of the dust particles in the debris disk around Vega is in the order of about 1 Myr, which is much shorter than the age of this star ( $\sim 350$  Myr) (Habing et al., 1999). Therefore, the presence of small dust grains in debris disks implies that they are constantly resupplied. This is thought to be mostly through collisions among the larger bodies and/or evaporation of comets (Li & Greenberg, 1998; Grun et al., 1985; Habing et al., 1999). Thus debris disks are often called “second generation disks” for this reason.

Stellar radiation has two main effects on dust. Very small particles are pushed out of the system by its pressure. On the other hand, larger particles remain bound to the star, but a relativistic effect called ‘Poynting-Robertson drag’ causes them to spiral inwards towards the star, eventually destroying them, unless the particle is larger than  $\sim 1$  mm, in which case it can retain a stable orbit.

Radiation pressure, sometimes also referred to as photon pressure, is the radial component of the radiation force of a star. It is often quantified by,  $\beta$ , a dimensionless parameter that gives the ratio of the radiation force to the force of gravity. Because both gravity and radiation pressure have a  $1/r^2$  dependence, with  $r$  being the radial distance to the star, the  $\beta$  parameter is a constant for a particular body regardless of its distance.  $\beta$  goes roughly as the surface area to volume of the body, and thus small particles have larger  $\beta$ , that is, they are relatively more affected by radiation pressure than larger particles. The definition of  $\beta$  is (Burns et al., 1979):

$$\beta = \frac{F_{rad}}{F_g} = \frac{3L_{\star}Q_{PR}}{16\pi cGM_{\star}\rho s} \approx 0.57 \left( \frac{\rho}{1 \text{ g cm}^{-3}} \right)^{-1} \left( \frac{s}{1 \mu\text{m}} \right)^{-1}, \quad (1.1)$$

where  $L_{\star}$  and  $M_{\star}$  are the luminosity and mass of the star,  $c$  is the speed of light in vacuum,  $\rho$  and  $s$  are the density and size of the dust, and  $Q_{PR}$  is a dimensionless quantity called the Mie Scattering coefficient which is of order unity for a perfectly absorbing particle. Equation 1.1 is independent of the distance to the particle and only depends on the properties of the star and the particle. This equation implies that particles are not gravitationally bound if  $\beta > 1$ , in which case radiation force overcomes the force of gravity and the result is that the particle leaves the system.

Radiation pressure is most effective on sub- $\mu\text{m}$  particles and removes them over timescales of less than several tens of years (Artymowicz, 1988). While the radiation pressure pushes small ( $\lesssim 1 \mu\text{m}$ ) dust away from the star, another effect, called the Poynting-Robertson (PR) drag, makes particles with  $1 \mu\text{m} \lesssim s \lesssim 1 \text{ mm}$  slowly migrate toward the star. This is a relativistic effect caused by the fact that in the frame of reference of the star, the dust in orbit around the star preferentially re-emits radiation more in the forward direction than in the direction of the star. The result is that the particle loses angular momentum and starts spiraling inward. This is illustrated by Figure 1.14.

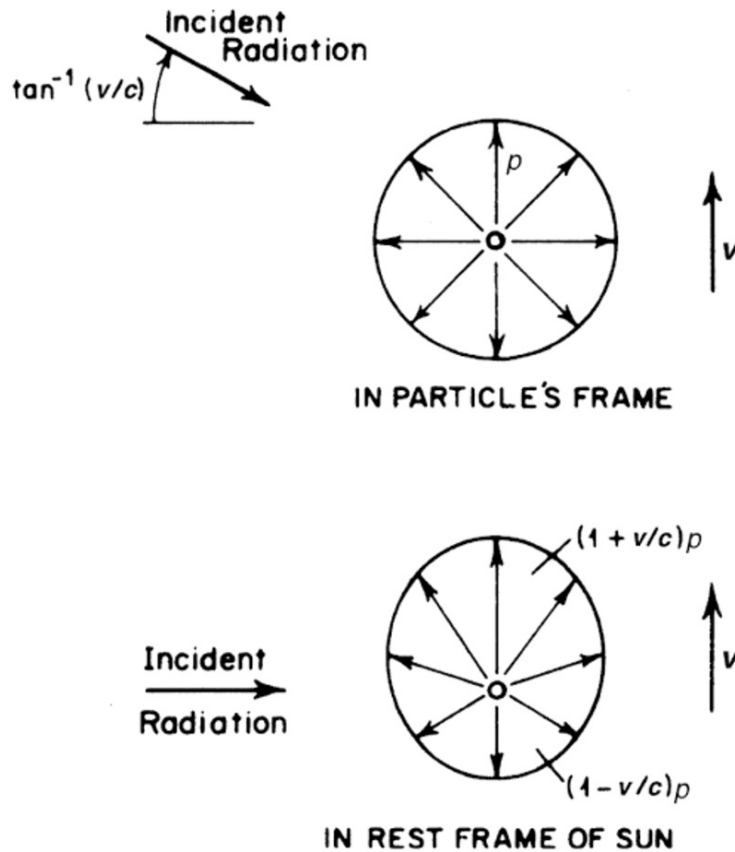


Figure 1.14: Dust particles absorb and re-emit the radiation from the star. The re-emission by dust, although isotropic in its own frame of reference (top), is larger in the direction away from the star in the star's rest frame (bottom). Thus the particle loses angular momentum and decays toward the star as a result of this so-called Poynting-Robertson (PR) drag. In this schematic illustration of the PR effect,  $p$  is the radiation momentum and  $v$  is the tangential component of the particle's velocity which is zero in the particle's frame. Credit: Burns et al. (1979).

Therefore, the spatial distribution and the ultimate fate of circumstellar particles of various sizes are determined by the  $\beta$  parameter such that the dust particle is blown out of the system if  $\beta > 0.5$  but its orbit decays otherwise. The orbits of particles of various  $\beta$  values are shown schematically by Figure 1.15.

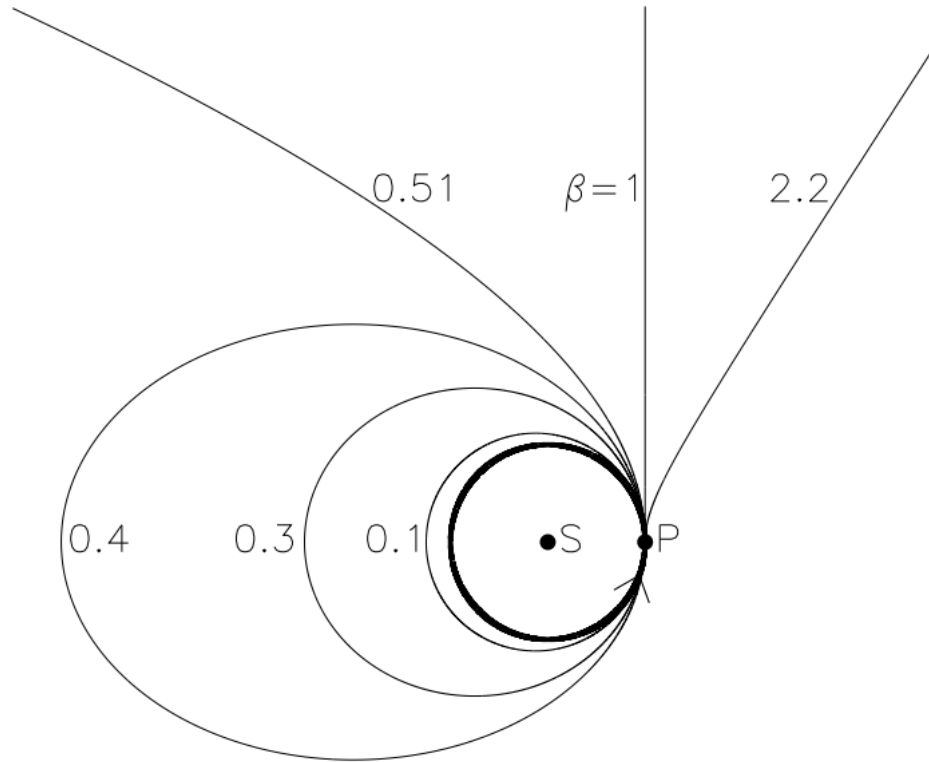


Figure 1.15: Schematic illustration showing a parent body, P, initially in circular orbit (shown with a thick circle) around a star, S, that has fragmented into a range of smaller bodies of various sizes. Depending on their  $\beta$  parameter, the fragments take on different orbits. Those with  $\beta = 0$  are entirely unaffected by the radiation pressure and retain the orbit of the parent body. As  $\beta$  approaches 0.5, the fragments take on more and more eccentric orbits but their pericenter distance remains the same as that of the parent body. Finally, any fragment with  $\beta > 0.5$  is unbound and leaves the star on a hyperbolic orbit. Credit: Wyatt et al. (1999).

However, Wyatt et al. (1999) suggests that the effect of the PR drag in removing dust from debris disks can be overlooked since particles get destroyed in a collisional cascade before they move far from where they are produced. In this scenario collisions between dust particles grind them down to smaller sizes (and larger  $\beta$ ), which are removed by radiation pressure even before they spiral inward under the PR drag. This is due to the fact that collisions must happen very

frequently in dusty disks that are detectable in thermal emission in order to produce high dust surface densities. The PR decay time as well as the collisional time of dust particles are given by Equations 1.2 and 1.3, respectively (Wyatt et al., 1999):

$$t_{pr} = 400(M_{\odot}/M_{\star})[(r_1/a_{\oplus})^2 - (r_2/a_{\oplus})^2]/\beta, \quad (1.2)$$

which gives the time (in years) that it takes the orbit of a particle to decay from a radial distance of  $r_1$  to  $r_2$ , where distances are in AU ( $a_{\oplus} = 1$  AU). On the other hand, the collisional lifetime of dust is:

$$t_{coll} = \frac{P}{4\pi\tau_{eff}(r)}, \quad (1.3)$$

where  $\tau_{eff}$  is the wavelength-dependent optical depth of the disk which is a measure of its surface density,  $P$  is the mean orbital period of the particle (in years) given by Kepler's third law as:

$$P = \sqrt{(a/a_{\oplus})^3(M_{\odot}/M_{\star})}. \quad (1.4)$$

According to Wyatt et al. (1999), the PR drag does not influence the evolution of the observed dust disks since in order for these disks to be detectable in thermal emission, they must have high surface densities which would consequently result in frequent collision among their constituent dust particles, hence making  $t_{PR} > t_{coll}$ . This would mean that  $\tau_{eff}(r) > 10^{-4} \sqrt{(M_{\odot}/M_{\star})(r/a_{\oplus})}$  (or  $\beta_{pr} > 0.5$ ) for the observed disks. Therefore, dust does not get a chance to decay onto the star before it gets collisionally broken up and blown out by radiation pressure. We will return to this idea and explore it in more details in Section 3.2.3.

Despite its continuous regeneration, the lifetime of dust disks is short, in the order of 0.5 Gyr (see the next section), while planetesimal disks can survive throughout the lifetime of their system. Although the term “debris disks” is used interchangeably to refer to both dust disks and planetesimal disks, we shall discuss each separately in the two sections that follow.

### 1.4.1 Dust Disks

In this section, we will address disks formed by the smallest (sub-mm) solid particles that are left after the primordial disk disappears. In particular, we will address how structures and asymmetries observed in dusty disks have been used in the search for planets beyond the Solar System.

#### Structure and Application to the Search for Exoplanets

One of the goals of this thesis is to connect disk structures to their causes, where here the focus is on structures caused by planets. Observations of dust disks often reveal significant and non-axisymmetric structures. Some examples include dust disks around Vega, Fomalhaut, and  $\epsilon$  Eridani.

For instance, using the *James Clerk Maxwell Telescope (JCMT)*, sub-millimeter observations at  $850 \mu\text{m}$  by Holland et al. (1998) of the young (200 Myr) A3V star Fomalhaut that is located 7.7 pc from the Sun revealed two clumps in the north and south, both of which are offset from the star by  $10''$  ( $\sim 80 \text{ AU}$ ) (see Figure 1.16). A more recent study by Holland et al. (2003), also using the *JCMT* but at  $450 \mu\text{m}$ , confirmed the existence of at least one clump with about 5% the total flux in Fomalhaut's disk. The clumpy structure was explained by Wyatt & Dent (2002) to possibly be either due to a localized collision of larger bodies producing the dust which can remain close to the parent bodies for up to 700 dynamical periods (that is if the collision is non-catastrophic) or be the result of the temporary trapping of dust particles in external 2:1 mean-motion resonance with an unseen planet at 80 AU as it migrates outward (see Chapter 2 for a detailed description of the mean-motion resonance).

If the clumpy structure seen in dust disks such as Fomalhaut, Vega, and  $\epsilon$  Eridani are in fact due to resonant trapping of particles by planets, this can be used to trace unseen planets in exoplanetary systems (see for instance Greaves et al., 1998; Liou & Zook, 1999; Liou et al., 2000; Ozernoy et al., 2000). This would be analogous to the trapping of dust and the consequent formation of non-axisymmetric structures observed in the zodiacal cloud in Earth's



orbit (Dermott et al., 1994) and can be extended to extrasolar debris disks in the search for signatures of exoplanets. For instance, using numerical simulations of dust traps in a planet’s external MMR, Ozernoy et al. (2000) obtained structures that resemble remarkably those seen in Vega and  $\epsilon$  Eridani. They were also able to reproduce the horseshoe-shaped features detected in Fomalhaut’s disk with a  $0.3 M_J$  planet that traps dust in 1:1 MMR, the so-called “Trojan” companions. In a similar manner, the planets that are believed to have caused the clumpy structures in Vega and  $\epsilon$  Eridani are estimated, on the basis of numerical simulations of their effect on their disks, to have masses of  $3 M_J$  (Wilner et al., 2002) and  $0.1 - 0.2 M_J$  (Quillen & Thorndike, 2002; Ozernoy et al., 2000), respectively.

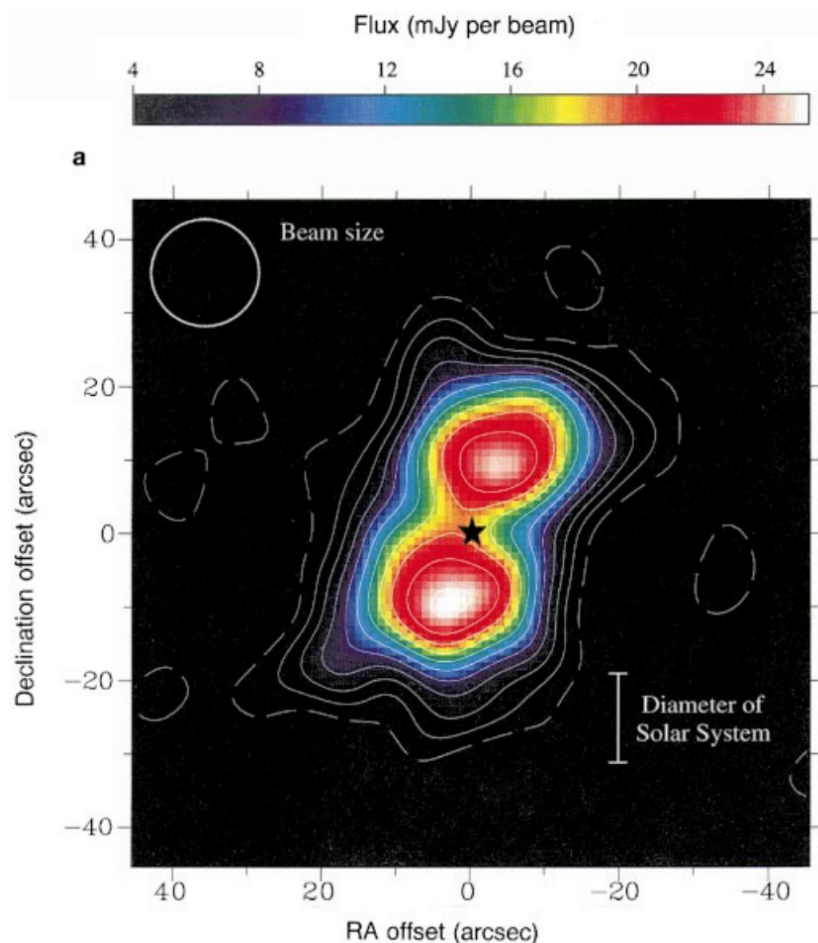


Figure 1.16: Clumpy structure in Fomalhaut’s disk revealed by observation of dust emission at  $850 \mu m$  was explained as possibly being caused by a planet at 80 AU. Contours show  $1\sigma$  intervals starting at  $2\sigma$  (the dashed contour). Credit: Holland et al. (1998).

In addition to forming clumpy structures, a planet can also warp the disk (see Burrows et al., 1995; Augereau et al., 2001) as well as offset its center of symmetry from the star (see Wyatt et al., 1999; Kalas et al., 2005). Warps may be caused by a planet that is inclined to the disk and was first noted in the edge-on disk around  $\beta$  Pictoris (Burrows et al., 1995) as a  $\sim 5^\circ$  tilt in the its inner ( $< 80$  AU) component of larger bodies (planetesimals) with respect to the outer main disk of particles that extends to thousands of AU (see Figure 1.17). Observations by Lagrange et al. (2010) later confirmed that there is, indeed, a planet a few times Jupiter's mass 9 AU from  $\beta$  Pic and that its orbit is inclined to the main disk by  $\sim 1^\circ$  (Lagrange et al., 2012). This provides a good example of how the study of disk structures can lead the way to planet discoveries.

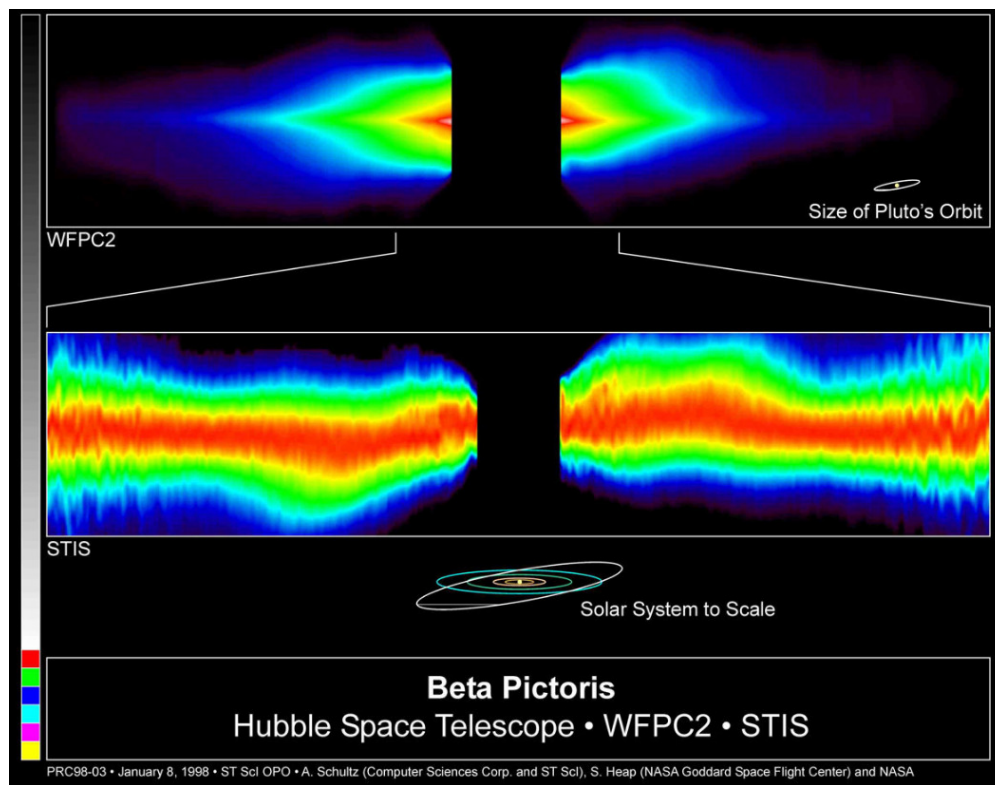


Figure 1.17: The warped inner disk in the  $\beta$  Pic system, first noted observationally by Burrows et al. (1995) and shown in this HST image of the disk, is indicative of gravitational interaction with a planet on an inclined orbit. The disk extends to at least 1000 AU from the star and the warp occurs at around  $\sim 70 - 150$  AU (e.g. Burrows et al., 1995; Heap et al., 2000). The size of the Solar System is given for comparison. Credit: Heap (GSFC/NASA), Schultz (CSC/STScI, and NASA).

Similar effects have been observed in protoplanetary disks as well. Recently Debes et al. (2017) noted a shadow sweeping across the TW Hya disk which is believed to be cast by a warped inner disk that precesses due to an unseen planet (see Figure 1.18).



Figure 1.18: One of the consequences of the planet-disk dynamical interaction is the warping of the disk which was shown by Debes et al. (2017) to cast a shadow moving across the disk as the orbit of the innermost planet around the protoplanetary disk TW Hya precesses. This is illustrated schematically by the figure on the right and was observed by comparing two HST images of the disk taken one year apart (top left panels) which becomes even more evident when the images are enhanced (bottom left panels). Credit: NASA, ESA, A. Feild (STScI) and J. Debes (STScI).

Whereas a planet on an inclined orbit to a disk can be revealed through its signature warping of the disk, a planet on an eccentric orbit can also leave its imprint on the disk by offsetting its center from the star. We will leave discussion of disk offset to Section 3.2.2 where we outline the effect of a planetary perturber that has non-circular orbit.

The fact that most systems with excess infrared emission have non-axisymmetric structures, with some even showing warps and offsets, suggests that they have at least one planet embedded in or near their dusty disks. Therefore, perturbed disks can be used to infer presence of planets whose parameters can be determined through numerical simulations. In addition to providing clues to the existence of planets, dust is often used to probe planetesimals in extrasolar systems. We shift our focus to these larger solid bodies in the next section.

### 1.4.2 Planetesimal Disks

Planetesimals are large pieces of rock and/or ice that are believed to be remnants of the primordial cloud that formed the stars and planets. The planetesimals coagulated from smaller solid particles that condensed from the cooling gas of the protoplanetary disk. The Solar System has two of such planetesimal disks, the Main Asteroid Belt located between the orbits of Mars and Jupiter, as well as the Kuiper Belt that starts just around Pluto's mean distance from the Sun. Unlike dust particles that have short lifetimes as discussed earlier, planetesimals are long-lived dynamically and less active geologically. This makes them pristine sources of information that offer clues to the formation and evolution of planetary systems. Due to their relatively large sizes (compared to dust), planetesimals are insensitive to radiation and drag forces ( $\beta \ll 1$ ) and are dominantly affected by the gravitational force of the central star.

It is not unreasonable to expect to find extrasolar debris disks that resemble our own Main Belt and Kuiper Belt, though it would require high resolution facilities and advanced adaptive optics to observe them directly in scattered light. Instead, we expect to more easily observe dust produced by the inevitable collision of planetesimals, and thus observations of dust in thermal emission can be used to study planetesimal disks.

Observations of thermal emission in mm and sub-mm wavelengths are sensitive to detecting emission from dust that is comparable in size to the wavelength with which it is observed. Therefore, dust particles are often used as tracers of larger, planetesimal-size bodies from which they are believed to be originated. For instance, using  $10 \mu\text{m}$  spectroscopic observations with Subaru, Okamoto et al. (2004) noticed three peaks at 6, 16, and 30 AU in the spatial profile of  $0.1 \mu\text{m}$  dust grains around  $\beta$  Pictoris which they interpreted as recent fragmentation from larger bodies from a nearby belt of planetesimals. The multiple ring system points to multiple planets around  $\beta$  Pic that have sculpted its circumstellar disk. They also observed an asymmetry in the innermost belt, suggesting that it is inclined to the other two disks and which is in line with earlier findings by Burrows et al. (1995) of the dynamical signature of an inclined planet.

### Mean-Motion Resonance

One important feature of the Solar System's asteroid belt is structures formed through mean-motion resonances of disk particles with, primarily, Jupiter. This was shown for the first time in 1867 by Daniel Kirkwood who noted regions that are almost devoid of asteroids when he plotted the number of asteroids that were known at the time as a function of their semimajor axis (another of the orbital elements, see Appendix A) (Kirkwood, 1867). This is illustrated by Figure 1.19. He was also able to pinpoint that the semimajor axes where the gaps occurred were not independent of Jupiter's. In fact, the ratio of the semimajor axis of each gap to that of Jupiter turned out to be a simple fraction, bringing particles with those semimajor axes into periodic conjunctions with Jupiter in a so-called "mean-motion resonance" configuration.

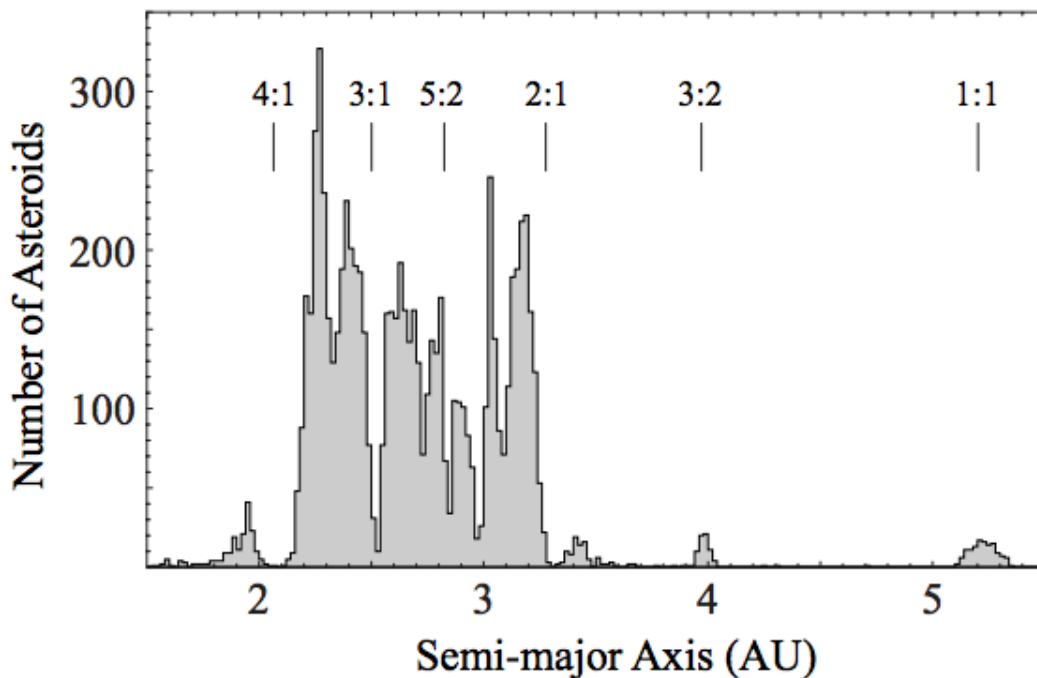


Figure 1.19: Histogram showing distribution of the Solar System's Main Belt asteroids in semimajor axis. Gaps occur at mean-motion resonances with Jupiter while some resonances (such as 1:1 and 3:2) trap particles and form the Trojan and Hilda family of asteroids. Credit: Murray & Dermott (1999).

Two particles are said to be in mean-motion resonance if their orbits are commensurable, meaning that for every  $p$  number of times one particle orbits the star, the other completes

$p + q$  orbits, where  $p$  and  $q$  are positive integers. MMRs often result in destabilization and the consequent removal of the less massive particle from its orbit over the course of a few orbital periods, forming gaps in particle distributions. In some cases, the particles may not actually be removed but they go into orbits with larger eccentricities which would mean that they spend more time near apoastron, causing gaps to show in their distribution.

Resonances are not always destructive and can sometimes trap particles and form stable configurations similar to the Trojan and Hilda family of asteroids in the Main Belt that are in 1:1 and 3:2 MMR with Jupiter, respectively. What exactly makes resonances destructive or constructive is not well understood. We shall focus on the scenario that results in gap formation, either via resonant removal of particles, or by sending them into high eccentricity orbits. We establish a method that uses MMRs to look for and characterize planets beyond the Solar System which will be discussed in Chapters 2 and 3.

Studies have been done to address azimuthal asymmetries in extrasolar debris disks and their relation to planets in these systems, but when it comes to structures formed by possible MMRs with unseen planets, they are mostly related to particle trappings in resonances. Therefore, a discussion of the structures formed by the resonant gap formation in extrasolar debris disks, and how they can be used to identify and study unseen planets in these systems is largely missing from the literature. There are, however, a few exceptions, though they do not provide a comprehensive picture for the characterization of extrasolar planets through MMRs. For instance, a numerical simulation of resonant structures formed in a planetesimal disk by a non-migrating planet by Reche et al. (2008) produced gaps that are strikingly similar to what we will discuss in this work; however, the authors did not address these gaps in detail, neither did they discuss how they can be used to characterize the planet causing them. Another example is the work done by Okamoto et al. (2004) in which the authors explained the outer and inner edges of the innermost ring of planetesimals around  $\beta$  Pictoris as being sculpted by the 2:1 and the 4:1 MMR with an unseen exterior planet. They attempted to determine the location of a planet that they believed to be between the first and second rings (see Figure 1.20), the same

planet that had been thought to have caused the warping of the inner disk. They placed the potential  $\beta$  Pic planet at 12 AU, also putting it in a 3:2 resonance with the middle belt. The planet was later found through observations made by Lagrange et al. (2010) to have a semimajor axis of  $\sim 9$  AU.

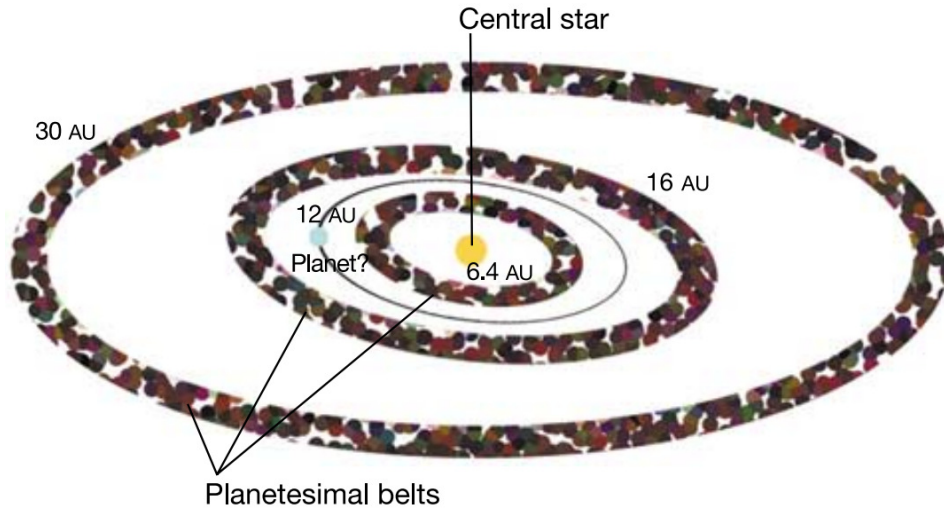


Figure 1.20: Conceptual illustration of the three planetesimal belts around the star  $\beta$  Pictoris, believed to be the sources of smaller particles found from the thermal emission of dust. If the outer and inner edges of the innermost belt at 6.4 AU are defined by the 2:1 and 4:1 MMR with an exterior planet, that planet must have a semimajor axis of 12 AU. Credit: Okamoto et al. (2004).

## 1.5 Summary

Planet-disk interactions during the early stages of planet formation are believed to play a crucial role in disk evolution as well as the formation and evolution of planetary systems. At later times, the gas dissipates, leaving a long-lived debris disk that is able to survive scattering by planets and which persists around at least 15% of main-sequence stars (Habing et al., 1999, 2001; Lagrange et al., 2001).

Planets cause, or are suspected to cause, a variety of structures in debris disks. Since the disks are both larger and (often) brighter than any embedded planets, studies of disks offer the possibility of detecting and studying planets indirectly. Given the fact that direct imaging of

extrasolar planets is extremely challenging, indirect techniques, such as the one we present in this work, could potentially be very powerful in identifying and characterizing planets beyond the Solar System.

The observed structures in circumstellar disks are largely attributed to planets interacting with the disks gravitationally, making gaps and other dynamic features key pieces of evidence for the existence of planets in or near these disks. The dynamics of gap opening via planet-disk interactions is not very well understood, particularly if more than one planet is present, as perturbations by additional planets could further complicate the disk structure. Nevertheless, studying the sources of the observed asymmetries in both gas-rich and gas-poor disks can potentially help piece together the broad picture of not only how planets form and evolve but also provide clues to the properties of the planets that are believed to be responsible for many of the observed symmetric and asymmetric features of circumstellar disks.

As the quest for finding planets outside the Solar System continues, understanding the structure and evolution of debris disks is essential in the detection and characterization of evolved extrasolar planets. The present work addresses this through the analysis of disk-planet dynamical interactions via mean-motion resonances. Chapters 2 and 3 outline the resonant interactions of a debris disk with a single non-migrating planet. Though determination of the mass of the companion would help reveal whether it is a planet or a star, we ignore the possibility of the companion being a star for simplicity. We will then shift our focus to a protoplanetary disk, the HL Tau, in Chapter 4 and try to address the question of whether some of its prominent gaps that have been observed by the powerful ALMA interferometer can be explained using a simple “particle-only” dynamical model. Computationally less intensive and with fewer free parameters, we compare this minimal model with more extensive ones in the literature to determine how much information we can glean about gas disks without the use of sophisticated hydrodynamic models.



# Bibliography

- Akiyama, E., Muto, T., Kusakabe, N., et al., 2015, ApJ, 802, L17.
- Andrews, S. M., Wilner, D. J., Hughes, A. M., et al., 2009, ApJ, 700, 1502.
- Andrews, S. M., Wilner, D. J., Espaillat, C., et al., 2011, ApJ, 732, 42.
- Andrews, S. M., Wilner, D. J., Hughes, A. M., et al., 2012, ApJ, 744, 162.
- Apai, D., Pascucci, I., Brandner, W., et al., 2004, A&A, 415, 671.
- Artymowicz, P., 1988, ApJ, 335, L79.
- Augereau, J. C., Nelson, R. P., Lagrange, A. M., et al., A&A, 370, 447.
- Aumann, H. H., Beichman, C. A., Gillett, F. C., et al. 1984, ApJ, 278, L23.
- Balog, Z., Siegler, N., Rieke, G. H., et al., 2016, ApJ, 832, 87.
- Bonavita, M., Chauvin, G., Boccaletti, A., et al., 2010, A&A, 522, 2.
- Brown, J. M., Blake, G. A., Qi, C., et al., 2009, ApJ., 704, 496.
- Burns, J. A., Lamy, P. L., Soter, S., 1979, Icarus, 40, 1.
- Burrows, C. J., Krist, J. E., Stapelfeldt, K. R., & WFPC2 Investigation Definition Team., 1995,  
in BAAS, Vol. 27, 1329.
- Currie, T., Lada, C. J., Plavchan, P., et al. 2009, ApJ, 698, 1.

- Currie, T. 2010, ArXiv e-prints [arXiv:1002.1715]
- Debes, J. H., Jang-Condell, H., Weinberger, A. J., et al., 2013, *ApJ*, 771, 45.
- Debes, J. H., Poteet, C. A., Jang-Condell, H., et al., 2017, *ApJ*, 835, 205.
- Dermott, S. F., Jayaraman, S., Xu, Y. L., et al., 1994, *Nature*, 369, 719.
- Encrenaz, T., Bibring, J. P., Blanc, M., et al., 2004, *The Solar System*, 3rd Ed., Springer, Berlin.
- Espaillet, C., Calvet, N., D'Alessio, P., et al., 2007, *ApJL*, 670, L135.
- Espaillet, C., Calvet, N., Luhman, K. L., et al., 2008, *ApJL*, 682, L125.
- Espaillet, C., Muzerolle, J., Najita, J., et al., 2014, *Protostars and Planets VI*, pp 497-520.
- Fung, J. and Dong, R., 2015, *ApJL*, 815, L21.
- Greaves, J. S., Holland, W. S., Moriarty-Schieven, G., et al., 1998, *ApJL*, 506, L133.
- Grun, E., Zook, H. A., Fechtig, H., et al., 1985, *Icarus*, 62, 244.
- Habing, H. J., Dominik, C., Jourdain de Muizon, M., et al., 1999, *Nature*, 401, 456.
- Habing, H. J., Dominik, C., Jourdain de Muizon, M., et al., 2001, *A&A*, 365, 545.
- Holland, W. S., Greaves, J. S., Zuckerman, B., et al., 1998, *Nature*, 392, 788.
- Holland, W. S., Greaves, J. S., Dent, W. R. F., et al., 2003, *ApJ*, 582, 1141.
- Hughes, A. M., Wilner, D. J., Calvet, N., et al., 2007, *ApJ*, 664, 536.
- Hughes, A. M., Andrews, S. M., Espaillet, C., et al., 2009, *ApJ*, 698, 131.
- Jang-Condell, H., 2009, *ApJ*, 700, 820.
- Jang-Condell, H. and Turner, N. J., 2013, *ApJ*, 772, 34.
- Kalas, P., Graham, J. R., and Clampin, M., 2005, *Nature*, 435, 1067.

- Kirkwood, D., 1867, *Meteoric Astronomy: A Treatise On Shooting-stars, Fireballs, & Aerolites*, Philadelphia, PA: J. B. Lippincott & Co.
- Kraus, A. L. and Ireland, M. J., 2012, *ApJ*, 745, 5.
- Kraus, S., Ireland, M. J., Sitko, M. L., et al., 2013, *ApJ*, 768, 80.
- Lagrange, A. M., Backman, D. E., Artymowicz, P., 2001, in Mannings V., Boss A. P., Russell S. S., eds, *Protostars and Planets IV*, Univ. of Arizona Press, Tucson.
- Lagrange, A. M., Bonnefoy, M., Chauvin, G., et al., 2010, *Science*, 329, 57.
- Lagrange, A.-M., Boccaletti, A., Milli, J., et al. 2012, *A&A*, 542, A40.
- Li, A. and Greenberg, J. M., 1998, *A&A*, 331, 291.
- Liou, J. C. and Zook, H. A. 1999, *AJ*, 118, 580.
- Liou, J. C., Zook, H. A., Greaves, J. S., et al., 2000, in *Lunar and Planetary Science XXXI*, ed. C. Agee & D. Black (Houston: LPI), abstract 1416.
- Marsh, K. A. and Mahoney M. J., 1992, *ApJL*, 395, L115.
- Murray, C. D. and Dermott, S. F., 1999, *Solar System dynamics* (Cambridge: Cambridge Univ. Press).
- Muto, T., Grady, C. A., Hashimoto, J., et al. 2012, *ApJ*, 748, L22.
- NRAO, 2014, “*Birth of Planets Revealed in Astonishing Detail in ALMA’s ‘Best Image Ever’*”, National Radio Astronomy Observatory (Press Release).
- NRAO, 2016, “*ALMA Finds Compelling Evidence for Pair of Infant Planets around Young Star*”, National Radio Astronomy Observatory (Press Release).
- NRAO, 2016, “*Planet Formation in Earth-like Orbit around a Young Star: ALMA’s Best Image Yet of a Protoplanetary Disk*”, National Radio Astronomy Observatory (Press Release).

- O'dell, C. R., Wen, Z., and Hu, X., 1993, *ApJ*, 410, 696.
- Okamoto, Y. K., Kataza, H., Honda, M., et al., 2004, *Nature*, 431, 660.
- Owen, J. E. 2014, *ApJ*, 789, 590.
- Ozernoy, L. M., Gorkavyi, N. N., Mather, J. C., et al., 2000, *ApJ*, 537, L147.
- Plets, H. and Vynckier, C., 1999, *A&A*, 343, 496.
- Price, D. J., Wurster, J., Nixon, C., et al., 2017, *Publications of the Astronomical Society of Australia (PASA)*, arXiv:1702.03930.
- Qi, C., Ho, P. T. P., Wilner, D. J., et al., 2004, *ApJL*, 616 L11.
- Quillen, A. C. and Thorndike, S., 2002, *ApJL*, 578, L149.
- Reche, R., Beust, H., Augereau, J.C., et al., 2008, *A&A*, 480, 551.
- Rice, W. K. M., Armitage, P. J., Wood, K., et al., 2006, *MNRAS*, 373, 1619.
- Roberge, A., Weinberger, A. J., and Malumuth, E. M., 2005, *ApJ*, 622, 1171.
- Skrutskie, M. F., Dutkevitch, D., Strom, S. E., et al., 1990, *AJ*, 99, 1187.
- Smith, B. A. and Terrile, R. J., 1984, *Science*, 226, 1421.
- Strom, K. M., Strom, S. E., Edwards, S., et al., 1989, *AJ*, 97, 1451.
- Tamayo, D., Triaud, A. H. M. J. , Menou, K., et al., 2015, *ApJ*, 805, 100.
- Thalmann, C., Grady, C. A., Goto, M., et al., 2010, *ApJL*, 718, L87.
- van der Marel, N., van Dishoeck, E. F., Bruderer, S., et al., 2013, *Science*, 340, 1199.
- Weinberger, A. J., Becklin. E. E., Schneider, G., et al., 2002, *ApJ*, 566, 409.
- Wilner, D. J., Holman, M. J., Kuchner, M. J., et al., 2002, *ApJ*, 569, L115.

Wyatt, M. C., Dermott, S. F., Telesco, C. M., et al. 1999, ApJ, 527, 918.

Wyatt, M.C. and Dent, W.R.F., 2002, MNRAS, 334, 589.

## Chapter 2

# Detection and Characterization of Extrasolar Planets through Mean-Motion Resonances. I. Simulations of Hypothetical Debris Disks

*This chapter is adapted from: Tabeshian, M. & Wiegert, P. A., 2016, ApJ, 818, 159.*

### 2.1 Introduction

The detection of excess infrared radiation from a number of stars indicate the presence of debris disks around them, some of which, such as those around Fomalhaut and Beta Pictoris, have been observationally resolved. The first extrasolar debris disk ever discovered was found around Vega using *IRAS*, from the thermal emission of circumstellar dust which revealed a strong infrared excess beyond  $12\ \mu\text{m}$  (Aumann et al., 1984). The excess radiation was immediately linked to the possible presence of solid dust particles with radii greater than 0.12 cm and temperatures of approximately 85 K, located at a mean distance of 85 AU from the nearby

main sequence star  $\alpha$  Lyrae and which were believed to be debris left-overs from the formation of this stellar system (Aumann et al., 1984). This discovery sparked interest in studying debris disks outside our own Solar System and the first optical image of an exosolar debris disk emerged later in the same year. Using ground-based optical coronagraphy, Smith & Terrile were able to directly image a flattened disk of cold, solid material around  $\beta$  Pictoris (Smith & Terrile, 1984).

Interactions between planets and disks have been studied in great detail for gas-rich disks with the main motivation being understanding planet formation (see the review paper by Kley & Nelson, 2012). The study of geometric structures in protoplanetary disks has offered insights into the formation and evolution of planetary systems. Such structures, which are mostly believed to be signposts of planet formation, reveal themselves as density variations across the disk and have been inferred from Spectral Energy Distributions and high-resolution millimeter and submillimeter interferometry observations. There is strong theoretical and observational evidence for gaps (see for instance, Debes et al., 2013) as well as density enhancements that appear as complex features such as spiral patterns (e.g. Brown et al., 2009; Muto et al., 2012; Juhasz et al., 2014) and dust traps (e.g. Isella et al., 2013; van der Marel et al., 2013) in protoplanetary disks and that can create asymmetric structures. Observations of protoplanetary disks have revealed that asymmetric disks are common. Such asymmetries are interpreted as being either due to density perturbations of a stellar or planetary companion (e.g. Kraus et al., 2013) or having a geometric nature (e.g. Brown et al., 2009; Jang-Condell & Turner, 2013). Investigating the sources of density enhancements and depletions can result in a better understanding of the processes of formation and evolution of single and multiple planetary systems in gas-rich disks.

In a protoplanetary disk, drag against the gas causes solid particles to collapse into a dynamically cold disk in which the particle orbital eccentricities and inclinations are very low. The gas is eventually blown away by stellar radiation once the star is born and leaves behind a nearly circular, coplanar solid particle disk. This disk may include planets as well as smaller

planetesimals or other bodies, like the Solar System’s asteroid belt. Dynamical interactions of planets with these second generation disks have not been studied as extensively as gas-rich disks. In this paper, we shall focus on this later stage in which little or no gas remains. Such gas-poor disks include for example, the Fomalhaut (Cataldi et al., 2015), Vega (Wilner et al., 2002) and  $\beta$  Pictoris (Kalas & Jewitt, 1995) disks. Structures in the Fomalhaut disk, for example, cannot be due to gas-dominated processes because of its low gas content (Cataldi et al., 2015), but must arise from other processes.

We will show that the interaction of a planet with a debris disk can create structures that are not azimuthally symmetric about the star. Non-axisymmetric structures have been commonly observed in debris disks. For instance, observations of the debris disk around  $\beta$  Pictoris revealed a warp in the inner disk around  $\sim 70 - 150$  AU (e.g. Burrows et al., 1995; Heap et al., 2000). Dynamical modeling had suggested that the warp could be explained by a misaligned planet (e.g. Mouillet et al., 1997; Augereau et al., 2001) which was later confirmed when a  $9 \pm 3$  Jupiter-mass planet was found on an inclined orbit  $8 - 9$  AU from the central star (Lagrange et al., 2010). Asymmetries in debris disks have also been attributed to mean-motion resonances (MMRs). For instance,  $N$ -body simulations of a collisional debris disk by Nesvold & Kuchner (2015) show a peak in the disk’s surface brightness at 1:1 MMR with the planet. A second peak is observed in their simulation of a 3 Jupiter-mass planet and falls between the 3:2 and 2:1 MMR with the planet, indicating a depletion of planetesimals at the two resonances. Formation of overdensities in debris disks has also been explained by migrating dust (e.g. Wilner et al., 2002) or migrating planets (e.g. Wyatt, 2003). While migrating inward due to Poynting–Robertson (PR) drag, dust grains can become trapped in resonances with a planet interior to their orbit or get scattered, thus forming asymmetric structures in the disk. The same scenario applies to particles that are captured in a migrating planet’s resonances.

Structures in dust disks in which particles are strongly affected by the radiation pressure of the central star as well as the PR drag have been investigated by some authors (see for instance Kuchner & Holman, 2003; Wyatt, 2006; Krivov et al., 2007). However, not much emphasis



has been placed on the dynamical interactions of planets with planetesimal belts with regards to understanding of the MMR gaps and how they can be used to extract information about the planets causing them. For instance, Chiang et al. (2009) briefly discuss gap formation at MMRs with a planet interior to the Fomalhaut disk in an attempt to constrain the mass of Fomalhaut b, but do not provide further details on how such gaps could yield measurements of planetary parameters. On the other hand,  $N$ -body numerical simulations by Reche et al. (2008) show gap structures similar to what we shall discuss in the present work, but were not addressed by the authors. Here we address the question of what structure might be induced in a gas-poor extrasolar planetesimal disk by a non-migrating planet, and in particular what observational signatures might indicate the presence of an unseen planet in the system and how they can be used to constrain the planet's mass and orbital parameters. It must be noted that for the rest of this paper, whenever the term debris disk is used, it means disks with particles having size distributions in the range of about 1  $mm$  to 100  $km$  that are nearly unaffected by the central star's radiation pressure. Such particles can be gravitationally perturbed due to the presence of one or more planets in the system which could result in either their removal (like the Kirkwood Gaps in our Solar System) or accumulations (like the Hilda family of Main Belt asteroids). Studying these resonances is not only an indirect way of detecting unseen extrasolar planets, it can also help put constraints on some parameters of the planets which are creating them, such as their mass, semimajor axis and eccentricity.

The astonishingly detailed image of a disk around HL Tau, a Sun-like star approximately 450 light-years away in the constellation Taurus that was recently obtained by the *Atacama Large Millimeter/submillimeter Array* (ALMA), is a perfect example of structures being formed in disks due to planets (NRAO, 2014). Although the disk imaged around HL Tau is a protoplanetary disk different from the second generation debris disks we concentrate on in the present work, the ALMA image of HL Tau illustrates the increasing resolving power that can be achieved with state of the art telescopes. With ALMA soon starting its full operation, more detailed images of debris disks will become available, revealing more and more detailed struc-

tures such as those discussed here.

This paper is organized as follows: In Section 2.2, we briefly describe the dynamics of MMRs and the theoretical calculations of their maximum libration widths. Our method is presented in Section 2.3 in which we explain the code that is used to generate the simulations as well as the initial conditions. We present the different results obtained for interior versus exterior MMRs in Section 2.4, followed by discussions in Section 2.5. Finally, a summary and conclusions are provided in Section 2.6.

## 2.2 The Dynamics of Mean-Motion Resonances

The existence of gaps in the Solar System’s asteroid belt was first noted by American astronomer Daniel Kirkwood in 1867 who saw non-uniformities in the number distribution of asteroids in the Main Belt as a function of semimajor axis, with some ranges having few or no asteroids (Kirkwood, 1867). We now understand that gravitational interactions between the asteroids and Jupiter result in the removal of planetesimals from these orbits, making gaps to appear in the disk where a particle’s orbital period would be a simple fraction of that of Jupiter’s (Murray & Dermott, 1999). The close link between orbital period of an asteroid and its semimajor axis means that these “MMRs” occur over narrow ranges of semimajor axes, often depleting them of their original complement of bodies.

However, if one were to take an image of our asteroid belt from outside the Solar System, the Kirkwood gaps would not be observable due to the eccentricity of the asteroids blurring the edges of the gaps (see Figure 2.1). Though asteroids are removed from a number of resonances in the Main Belt, the eccentricities of the remaining asteroids are large enough to blur the edges of the resonances and make the gaps invisible. We will show that this is not always the case, and that under realistic conditions, visible gaps can be opened in particle disks by resonances. This means that gaps in extrasolar disks do not necessarily contain planets, as often assumed. Planets can also generate other resonant structures that both indicate their presence and provide

diagnostic information about their mass, eccentricity and position. Therefore, not only is the observation of gaps in debris disks an indirect way of detecting undiscovered extrasolar planets, it can also be used to constrain some parameters of the perturbing body if the gap widths and locations can be measured.

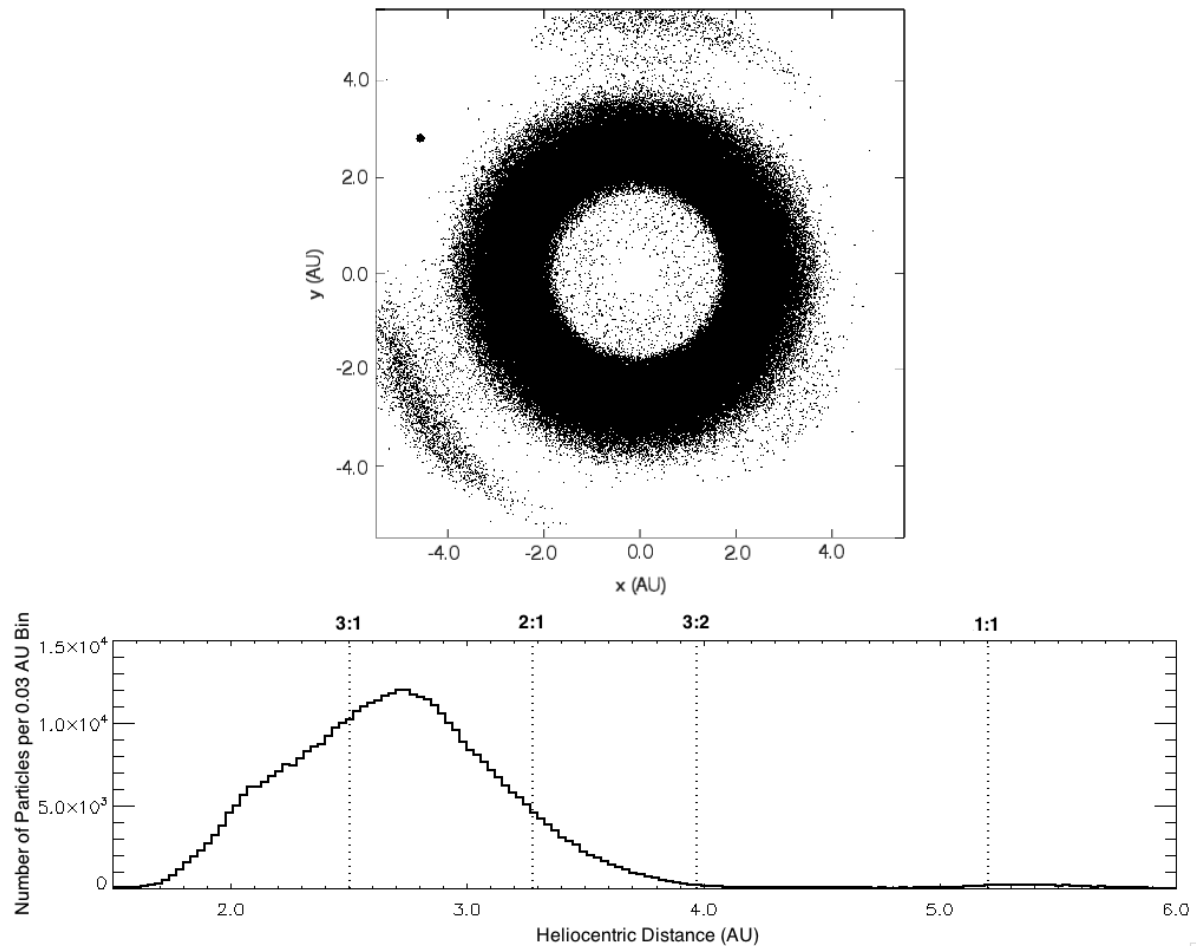


Figure 2.1: Orbits of known Solar System asteroids at or interior to Jupiter's as of 2015 June 27 plotted using data obtained from the Asteroids Dynamic Site (AstDyS). No Kirkwood gap due to MMR with Jupiter (shown with the black circle) can be seen in the disk (top panel) or the histogram (bottom panel) which shows the distribution of asteroids per distance from the Sun. This is due to the eccentricities of the asteroids that bring them in and out of the gaps. The theoretical locations of the three strongest resonances (2:1, 3:2, and 3:1) as well as the 1:1 resonance (Jupiter's Trojans) are shown on the histogram with vertical dotted lines.

Two objects are said to be in MMR if the following relation holds:

$$\frac{n}{n'} = \frac{p+q}{p}, \quad (2.1)$$

where  $n$  and  $n'$  are their mean-motions ( $= \frac{2\pi}{T}$ , with  $T$  the orbital period), and  $p$  and  $q$  are positive integers, with  $q$  denoting the order of resonance. The primed and unprimed quantities are the orbital elements of the particle being perturbed (the ‘‘asteroid’’) and the perturbing body (‘‘the planet’’), respectively. Equation 2.1 can, equivalently, be written in terms of the two objects’ semimajor axes,  $a$  and  $a'$ , as:

$$a' = \left( \frac{p+q}{p} \right)^{\frac{2}{3}k} a, \quad (2.2)$$

where  $k = +1$  for exterior resonance (i.e.  $a' > a$ ) and  $k = -1$  for interior resonance (i.e.  $a' < a$ ).

Following the discussion and derivations presented in Murray & Dermott (1999), to lowest order the resonant argument of the disturbing function,  $\phi$ , can be written as:

$$\phi = j_1 \lambda' + j_2 \lambda + j_3 \varpi' + j_4 \varpi, \quad (2.3)$$

where  $\lambda$  and  $\lambda'$  are the mean longitudes of the planet and the particle, respectively while  $\varpi$  and  $\varpi'$  are the longitudes of their periapse. Also,  $j_1 = p + q$ ,  $j_2 = -p$  and  $j_3$  and  $j_4$  are either zero or  $-q$ , depending on the relative locations of the two objects.

When a particle in a debris disk orbits in a MMR with a perturbing body, such as a planet, its orbit is perturbed in a consistent manner when the relative planet-asteroid geometry repeats itself. This often destabilizes the smaller body so that it either collides with the planet, crashes into the star, goes into a highly elliptical orbit or gets ejected. In either case, a gap forms in the disk whose width,  $\delta a'_{max}$ , can be approximated by the maximum libration width of its resonance. This can be calculated analytically at low eccentricities using Equation 2.4:

$$\frac{\delta a'_{max}}{a'} = \pm \left\{ \left( \frac{16|C'_r|}{3n'} e' \right)^{\frac{1}{2}} \left( 1 + \frac{1}{27j_2^2 e'^3} \times \frac{|C'_r|}{n'} \right)^{\frac{1}{2}} \right\} - \frac{2}{9j_2 e'} \times \frac{|C'_r|}{n'}, \quad (2.4)$$

where:

$$C'_r = \left( \frac{GM}{a'^2 a n'} \right) \times f_d(\alpha), \quad (2.5)$$

with  $G$  denoting the Universal Gravitational Constant,  $M$  the mass of the perturbing body,  $f_d(\alpha)$  a term containing Laplace coefficients and coming from three-body expansion of the two objects' orbital elements and  $\alpha = (\frac{a}{a'})^k$ . Equation 2.4 is given as Eq. (8.76) in Murray & Dermott (1999). Figure 2.2 shows the maximum libration widths at various eccentricities for the 2:1, 3:2, and 3:1 interior resonances with Jupiter. It is clear from this figure that in the case of first order resonances, the libration widths increase with eccentricity, except at very low eccentricities for which they become very large.

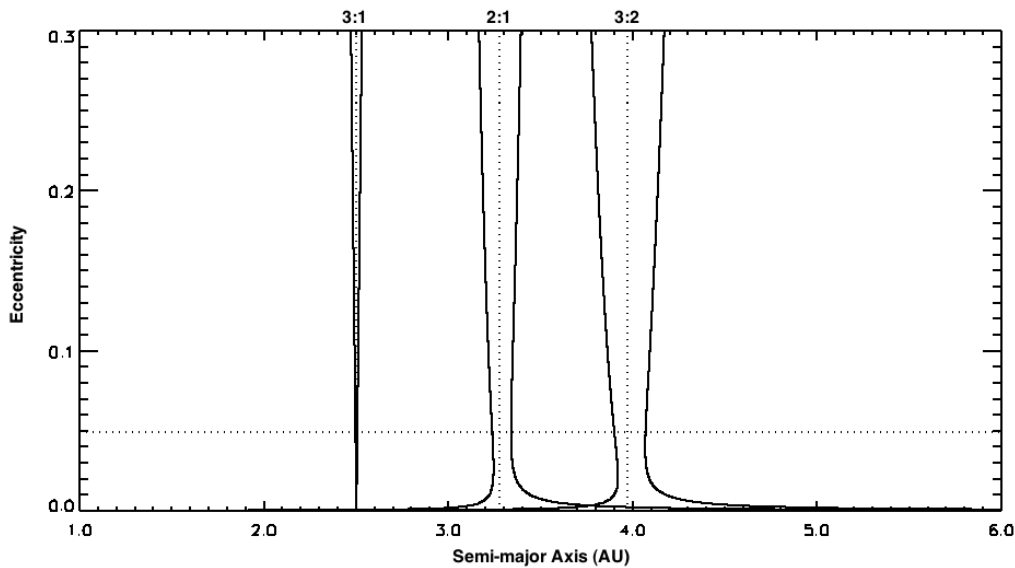


Figure 2.2: Maximum libration widths for 2:1, 3:2, and 3:1 Main Belt resonances with Jupiter. The vertical dotted lines are the locations of nominal resonances (calculated using Equation 2.2) and the horizontal dotted line shows Jupiter's eccentricity.

A MMR affects a narrow range of semimajor axes. The resulting resonant gaps will be visible in an optical or other telescopic image of the disk if (1) the resonance tends to destabilize particles (often but not always the case), (2) the eccentricity of the particles near the edges of the resonance is small enough to keep them from blurring the edges of the gap, and (3) the width of the gap is not smaller than the resolution of the telescope. The radial excursion,  $\Delta r$ , of the particles in the disk, given by  $\Delta r \sim 2ae$ , should be smaller than the resonance width. Thus the formation of MMR gaps is favored in dynamically cold particle disks, which have small eccentricities. It is the relatively high average eccentricities of asteroids that obscure the Kirkwood gaps in our own Main Asteroid Belt. From Figure 2.2, it is also clear that very low eccentricity disks may have very large resonant gaps since the resonance width increases sharply as the disk average eccentricity,  $e'_{ave}$ , approaches zero; hence very dynamically cold disks are good candidates for observing particularly large resonant gaps.

## 2.3 Simulations

### 2.3.1 The Method

Our simulations are performed with a symplectic integrator based on the Wisdom–Holman algorithm (Wisdom & Holman, 1991). A fixed timestep of 50 days is used for all simulations. The output is recorded at 10,000-year intervals and the total simulation time is taken to be 1 million years in length unless otherwise noted. A single planet on a circular or slightly elliptical orbit perturbs the disk, which orbits a 1 solar-mass star. Particles are removed if they have a close encounter with the planet or reach a distance less than 10 solar radii or greater than 1000 AU.

The gravitational effects of the star and planet are included but interactions between the particles themselves are ignored. Thus our simulations are applicable to low-mass debris disks, where the mass of the disk is much less than that of the planet. We also neglect the effects of the PR drag for simplicity; hence our simulations represent gas-poor planetesimal or debris

disks composed of solid bodies 1 *mm* to 100 *km* across and which are relatively free of dust. The presence of strongly reflecting or emitting dust can markedly affect the appearance of a disk, particularly if collision among the dust particles is considered. For instance, a study conducted by Stark & Kuchner (2009) shows that the ring structures created by the trapping of dust in resonance with a planet are smeared out by collisional interactions of the dust particles. On the other hand, Wyatt (2005) has argued that the collisional lifetime of dust in debris disk candidates is short enough that dust does not drift very far before its destruction. Here we model dynamically cold planetesimal disks with particle sizes upward of  $\sim 1$  *mm* that are not affected by radiation pressure and PR drag, a choice we justify in more detail in Section 3.2.3. Because disk emission is a function of the particle sizes, our simulations should be compared with observations such as mm observations by ALMA which detect these particle sizes. However, we note that the observational characteristics of disks observed at shorter (micron) wavelengths would be different due to the different dynamics of dust at these sizes. The mechanisms of dust production and removal in these disks are complex and their modeling is outside the scope of this paper. Nonetheless, it is reasonable to expect that at least some dust-poor systems exist, and it is to those that we turn our attention here.

The simulations are performed at scales appropriate to our Solar System (i.e., the perturbing planet is placed at Jupiter’s semimajor axis,  $\sim 5.204$  AU from the star). The physics involved scale with distance, however, and so our results are applicable to disks and planets in general, even if located at different distances from their parent stars. For clarity then, our figures are scaled so that the planet is at a unit distance. The exception to the scalability of our results is only the timescales for opening up the gaps, which are expected to be longer for larger systems or ones with less massive central stars.

### 2.3.2 Simulated Debris Disks

In order to investigate structures in debris disks that are caused by MMRs with a planet, we perform simulations of test particles in a flat disk (particle inclinations  $i' = 0.0^\circ$ ), containing

10,000 particles per 1 AU of the disk radial thickness. Running on a single CPU, the simulations take 12 hrs to complete for a disk with 20,000 particles and could last up to 4 days for three times the number of particles. The total simulation time also depends on the planet’s mass since more particles are ejected at the beginning of the simulations with more massive planets. The initial particle eccentricities are those of the forced eccentricity induced by the planet at each particle’s semimajor axis with their apses aligned with the planet’s. The forced eccentricity represents the eccentricity that the particle orbits are subject to due to the simple presence of the perturbing planet. By setting the initial conditions of the disk to this value, we create a disk which will be minimally perturbed by the planet. This choice represents a scenario where the planet and the disk have been in the same relative geometry for a significant fraction of the age of the system. Other choices result in a more heavily perturbed disk, with results that are highly dependent on the choice of the initial conditions. Such scenarios might be appropriate to cases of recent planetary migration but are not considered here. We note that for the case of a planet on a perfectly circular orbit, the forced eccentricity is also zero and the disk particles are started on circular orbits.

For simplicity, we assume that the planetary system contains one planet only and we choose the planet’s semimajor axis to be that of Jupiter ( $a = a_J = 5.204 \text{ AU}$ ), though as noted earlier the choice of this scale is arbitrary and the results apply equally to disk-planet systems of all sizes. Furthermore, in all of our simulations, we assume that the planet orbits in the same plane as the disk (i.e.  $i = 0.0^\circ$ ). However, we also tried some simulations with a small planet inclination ( $i = i_J = 1.304^\circ$ , Jupiter’s inclination). The results show no noticeable difference between the two cases. Therefore, even if the planet does not orbit exactly in the disk plane, we still expect the same features and to obtain similar results for small orbital inclinations.

The simulations are performed for the case of both interior and exterior resonances; and in both cases, the disk is placed 1 AU away from the planet ( $2.204 < a_{Disk} < 4.204$  for the interior resonance and  $6.204 < a_{Disk} < 12.204$  for the exterior case). The values for the disks’ inner and outer edges are chosen such that the three resonances being considered, the 2:1, 3:2, and 3:1,



fall within the debris disks. A range of planet masses is used, going from as small as  $1.0 M_{\oplus}$  to  $9.0 M_J$ , where  $M_{\oplus}$  and  $M_J$  are the mass of the Earth and Jupiter respectively. Furthermore, to study the effect of the planet's eccentricity on MMR gaps, two different planet eccentricity values are considered:  $e = 0.0$  and  $e = 0.0489$ , the eccentricity of Jupiter ( $e_J$ ), though we leave further investigations of eccentricity effects to a follow-up paper.

## 2.4 Results

As noted before, we choose our total simulation time to be a million years, which we find to be sufficient for the disks to achieve a quasi-steady state. Yet we observe gaps forming on much shorter timescales for more massive planets (e.g., less than 100,000 years, for a 5 Jupiter-mass planet exterior to the disk). More massive planets open gaps more quickly as would be expected, but we have not investigated this trend in the present work. At the end of the simulations, the disks are examined for structures, particularly those that would be observationally discernible in a telescopic image. Moreover, in order to be able to compare the widths of the gaps that are produced in the simulations with the analytical calculations of the maximum libration widths through Equation 2.4, we make histogram plots of the number of particles per heliocentric distance. The disk is divided azimuthally into four equal segments since the MMR gaps turn out to be azimuthally asymmetric, particularly in the case of the perturbing body having zero eccentricity.

It must be noted that although we calculate what the resonance widths should be analytically for the 3:2 and the 3:1 resonances as well as the 2:1, due to the narrower gaps these resonances produce we only measure the widths of the 2:1 gaps in our simulations. However, as we shall discuss in Section 2.5.6, we do observe a narrow feature at the 3:1 resonance.

### 2.4.1 Interior Resonance

Interior resonance refers to the case in which the planet is exterior to the disk and hence the resonances occur interior to the planet’s orbit. In this case, the 2:1 MMR opens gaps in two regions at inferior and superior conjunctions with the planet. This can be seen in Figure 2.3(a) which shows the case of a  $4.0 M_J$  planet on a circular orbit gravitationally interacting with the disk. The locations of the three prominent resonances are marked; the gap occurs at the 2:1 MMR with the planet. If we were to follow the double-arc gap over time, we would see it move around the star at the same rate as the planet. The appearance of such a gap in an image of a disk would both indicate the presence of a planet as well as its location (that is, along a line drawn through the deepest parts of each arc), though which side of the disk the external perturber is on cannot be unambiguously determined. This double-arc shape is a result of the removal of particles from the 2:1 interior resonance (see for example Fig. 8.4(a) of Murray & Dermott, 1999).

In order to measure the width of the gap seen in the simulation, we make a histogram for each of the four colored segments (separated by intervals of  $\pi/2$ , starting with  $-\pi/4 < \theta < \pi/4$ ) shown in Figure 2.3(a) for the number of particles as a function of their distance from the central star. This is shown in Figure 2.3(b) where the colors of the first four histograms correspond to the same colors used in Figure 2.3(a) while the last histogram shows the distribution of all the particles from the four segments put together. For simplicity, we will concentrate on the gap in the region closest to the planet (marked in red in Figure 2.3(a) and the top histogram of Figure 2.3(b)).

The dotted lines in Figure 2.3(b) are the theoretical locations of the three resonances that are being considered, calculated using Equation 2.2, while the dashed lines show the theoretical width of each resonant gap, obtained from Equation 2.4. In addition to the gaps that appear at the 2:1 MMR, the histograms also show a slight decrease in the number of particles in the region corresponding to the 3:1 MMR with the planet, although it is considerably narrower compared to the 2:1 resonance. The decrease at the 3:1 resonance in the sector nearest the

planet is a difference of about 50% which is 5 times the Poisson error for the bin and hence is statistically significant at this resolution. On the other hand, the 3:2 resonance which is closer to the planet cannot be seen since large numbers of particles in the outer edge of the disk have been removed due to strong gravitational interactions with the planet. To obtain a measure of the width of the 2:1 gap, we make a Gaussian fit to the histogram where the gap appears for comparison to the analytic results which we discuss in Section 2.5.3.

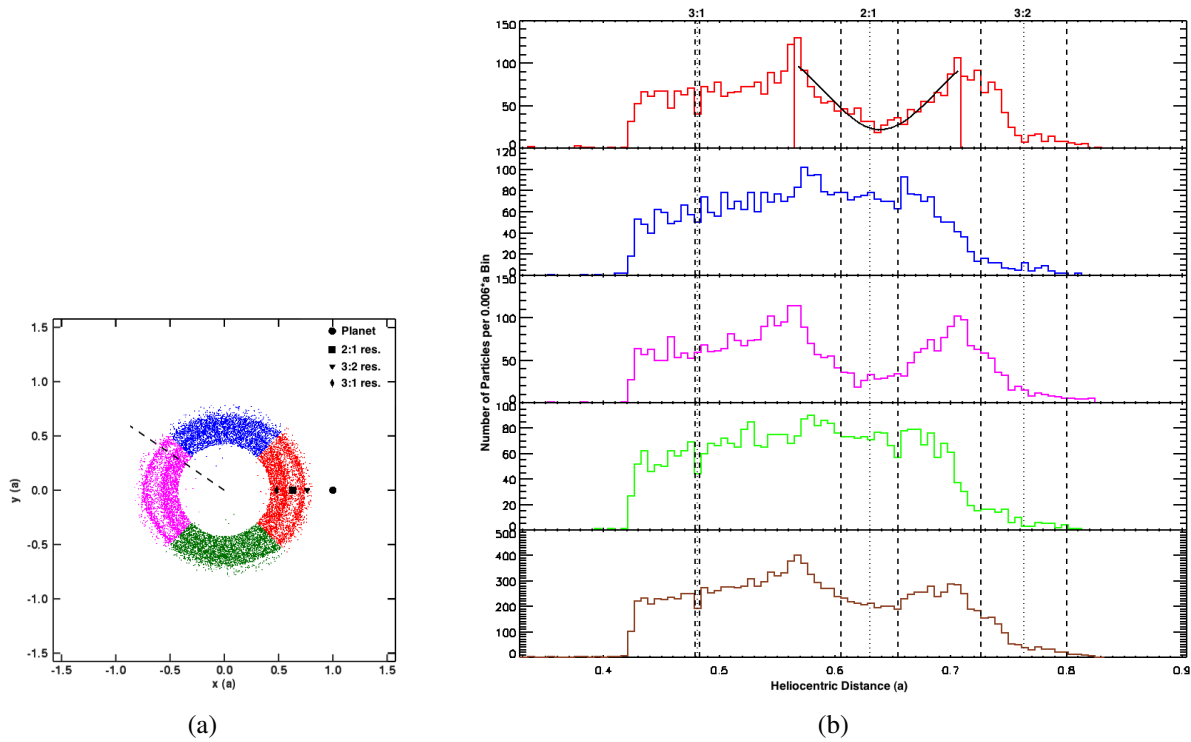


Figure 2.3: Simulation showing interior resonance structures formed by interactions of planetesimals in the disk with a  $4.0 M_J$  planet on a circular orbit exterior to the disk. (a) Interior resonances result in formation of two arcs of gaps in the disk. The dashed line shows the periastron of the planet's orbit and the symbols represent the three resonances considered while the filled circle is the planet. Different colors represent the different segments for which we make histograms of the distributions of particles in the disk (see Figure 2.3(b)). (b) Distribution of particles in the disk and MMR structures due to a planet exterior to the disk. The colors in the first four panels correspond to the same colors in Figure 2.3(a) for the different segments (from top to bottom: regions separated by intervals of  $\pi/2$ , starting with  $-\pi/4 < \theta < \pi/4$ ). The last panel shows the overall number distribution of the particles in the disk. The dotted lines are the theoretical locations of the 2:1, 3:2, and 3:1 resonances with the dashed lines defining the width of each gap calculated analytically. A Gaussian fit is made to the top histogram where the gap is to obtain a measure of the gap width from the simulations. The bin size is  $0.006 a$ , in the unit of the planet's orbital radius.

Figure 2.3 belongs to the case in which the planet perturbing the disk has zero eccentricity. When the planet's eccentricity is increased to 0.0489, features are seen in the disk that are similar to those of the zero eccentricity case. Additionally, the feature at the 3:1 MMR broadens. This feature, unlike the 2:1 gap, does not orbit the central star. This is shown in Figure 2.4 for a planet with  $e = e_J = 0.0489$ . We attribute the additional gap to the generation of tightly wound spiral waves at a Lindblad resonance in the disk, a phenomenon we explore in more detail in Section 2.5.6.

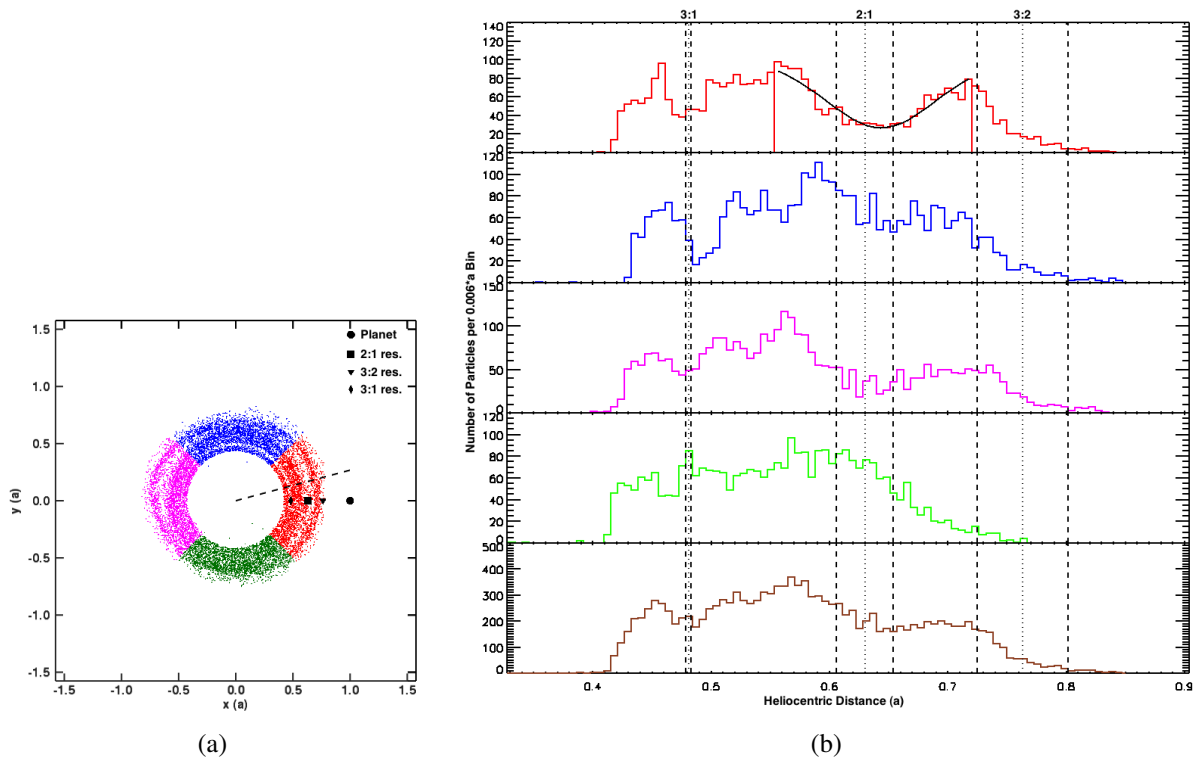


Figure 2.4: Same as Figure 2.3 but with planet's eccentricity increased to  $e = e_J = 0.0489$ . (a) Same as Figure 2.3(a) except that the planet's orbital eccentricity is increased to  $\sim 0.05$ . The extra feature at the 3:1 MMR is likely launched by Lindblad resonances and appears whenever the planet is given non-zero eccentricity. (b) Histogram plots for the disk shown in Figure 2.4(a) also indicate the presence of an extra gap at the 3:1 resonance with the planet.

## 2.4.2 Exterior Resonance

Resonance structures are different depending on whether the disk is internal or external to the orbit of the planet. For the case of exterior resonance (i.e., the planet being interior to the disk), we find the shape of the gap to be different. Instead of forming two arc-like sectors, the gap formed due to resonant interactions with a planet on a circular orbit is a single arc whose center aligns with the planet at opposition. This is shown in Figure 2.5(a) for a planet with  $M = 4.0 M_J$ . The arc again co-rotates with the planet and provides an indicator of the location of the perturbing body even if it were not visible in an image of the disk. We note again that the most prominent gap appears where the 2:1 MMR with the planet is (shown by the filled square). The different shape of the gap can also be explained in the same manner as for the interior resonance and is illustrated by Figure 8.4(c) of Murray & Dermott (1999). Thus the differing gap shapes for interior versus exterior resonances allow a great deal of information about a perturbing planet to be gleaned from images of disks that display gaps, even if the planet itself remains unseen.

Following the same analysis that is done for the interior resonance, we make a Gaussian fit to the gap that can be seen in the histogram for the region closest to the planet (see top panel of Figure 2.5(b)) to obtain the width and the mean location of the 2:1 MMR gap. We discuss the results of these measurements in Sections 2.5.3 and 2.5.4.

Figure 2.5 is obtained when the perturbing body (the planet) has no eccentricity. When the planet's orbital eccentricity is increased to that of Jupiter, the arc in the 2:1 gap remains easily visible but extends further, becoming more annular in shape. This is shown by Figure 2.6. In addition, the 3:1 feature observed in the case of the interior resonance (Figure 2.4) also becomes more prominent, and is explained in Section 2.5.6.

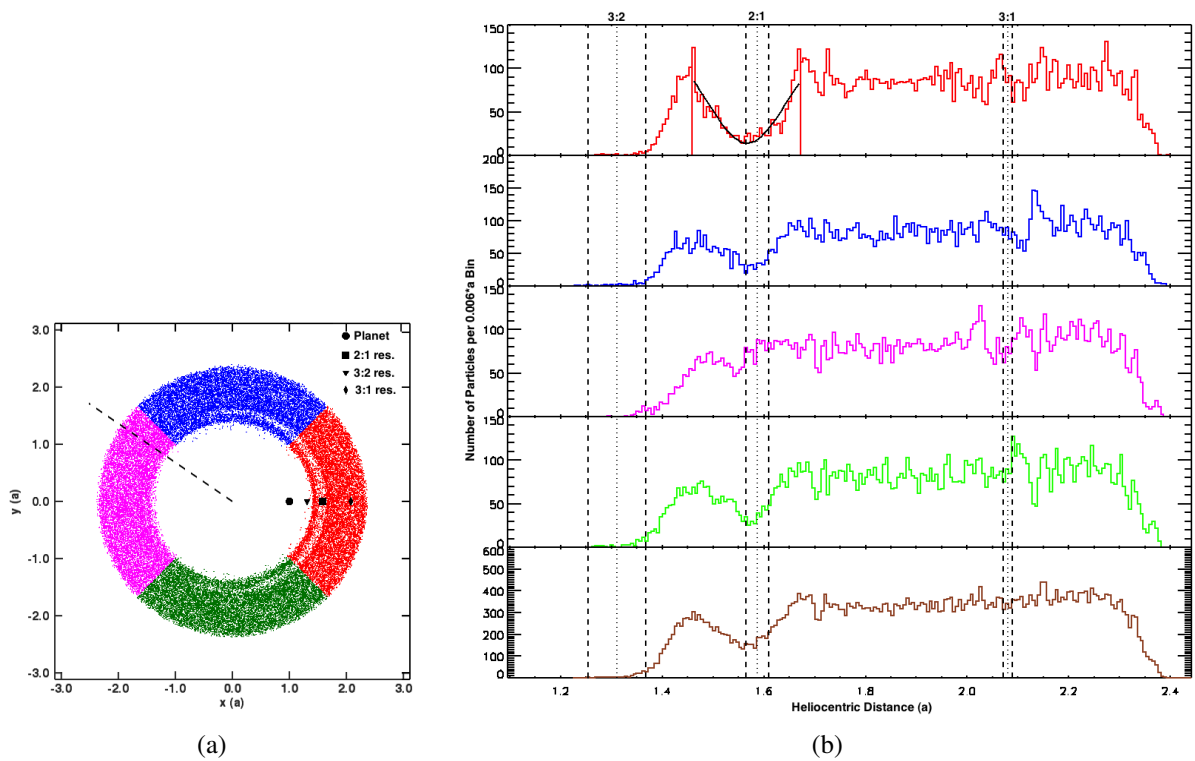


Figure 2.5: Structures formed by resonance interactions of planetesimals with a  $4.0 M_J$  planet on a circular orbit interior to the disk. (a) Exterior resonance with a planet on a circular orbit results in the formation of a gap that appears as a single arc in the region of the disk closest to the planet. (b) Distribution of particles in the disk for each segment marked in Figure 2.5(a).

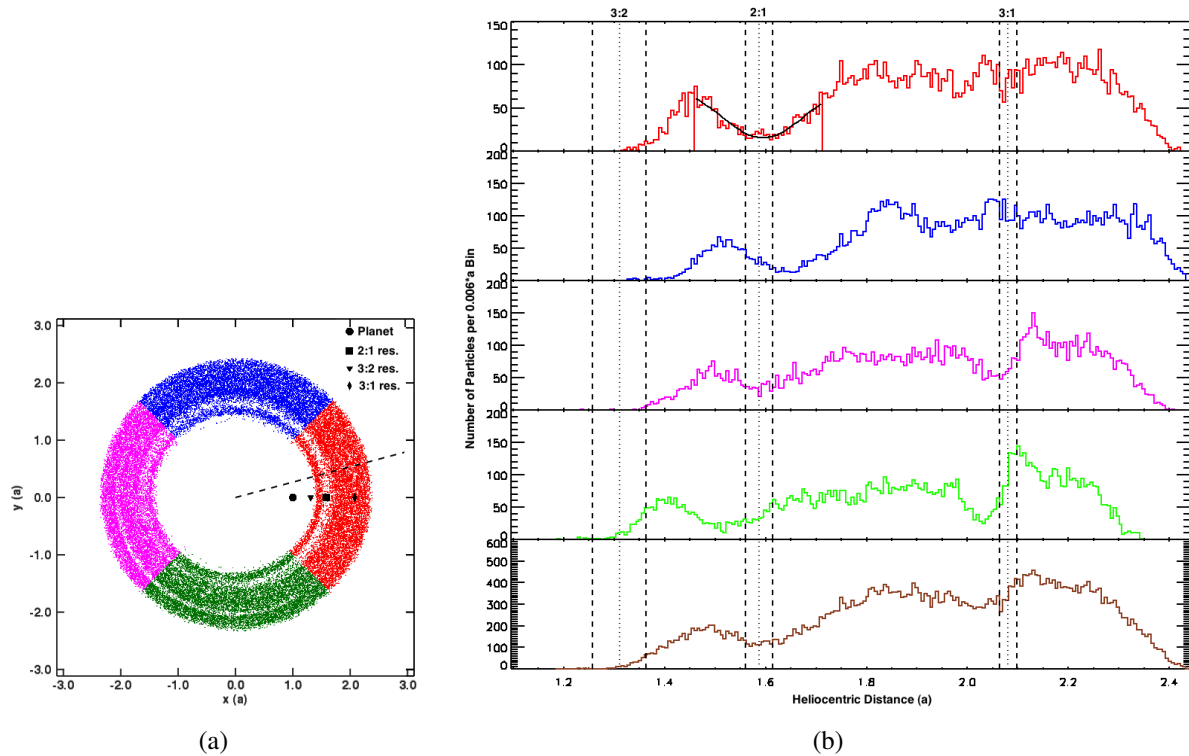


Figure 2.6: Same as Figure 2.5 but with planet's eccentricity increased to  $e = e_j = 0.0489$ . (a) Same as Figure 2.5(a) except that the planet is given some eccentricity ( $e \sim 0.05$ ). Similar to the case of the interior resonance with the perturbing planet on a non-circular orbit (Figure 2.4(a)), an extra gap appears in the disk with location corresponding to the 3:1 MMR with a planet interior to the disk. (b) Histograms corresponding to the different segments of the disk shown in Figure 2.6(a).

## 2.5 Discussion

The main purpose of this study is to provide the means of determining the properties of a perturbing planet in the case where a MMR gap is observed in a debris disk. This includes both the characterization of detected planets, as well as providing information on the mass and location of planets which remain as-yet unseen. We consider now how the results of our simulations provide insight into this issue.

### 2.5.1 Asymmetries in MMR Gaps

Our simulations suggest that the shape of a MMR gap is different for interior and exterior resonances. Therefore, by looking at the shape of a gap in a planetesimal disk we are not only able to immediately determine which side of the disk the perturbing planet is, the azimuthal asymmetry of the MMR gaps also allows us to easily distinguish between gaps formed due to MMRs with a planet that lies outside the gaps and those formed by planets in the gaps for which the gaps are azimuthally symmetric (such as the ones seen in the HL Tau disk). The only exception, according to our simulations, is the case of exterior resonance with a planet having non-zero orbital eccentricity for which we obtain nearly annular gaps at the 2:1 resonances. We note here that it is possible that increasing the eccentricity of the planet would result in the gap to eventually become completely annular, although we do not see that in a single sample simulation with  $e = 0.1$ . However, even in this case, we still observe an asymmetric feature at the 3:1 MMR with the planet. The presence of this additional gap at the 3:1 resonance, which occurs for both interior and exterior resonances, is indicative of the planet having non-zero eccentricity. We leave examining the effect of planet eccentricity on debris disk structures to a future paper.



### 2.5.2 Minimum and Maximum Detectable Planet Masses

We find that planets as small as  $M = 1.0 M_{\oplus}$  can produce MMR gaps (see Figure 2.7), but the practical lower limit on the mass of the planet that can open a detectable gap depends on the resolving capabilities of the observational facility taking the images. We are not aware of any disk with features meeting the above descriptions (i.e., disks with observed azimuthally asymmetric MMR gaps) that has yet been reported, but given the resolutions obtained by current facilities, we expect such features to be discovered in the near-future. For illustration, the disk around HL Tau has a radius of 120 AU (Kwon et al., 2011) and the recent ALMA image of the disk shows gap features as small as 5 AU across (Tamayo et al., 2015). For comparison, a 3 Jupiter-mass planet on a circular orbit just outside the edge of a planetesimal disk of similar size as the HL Tau disk would create a 2:1 resonance gap that is  $W = (0.015 \times 3.0 + 0.012) \times 80.0 \sim 4.6$  AU wide, comparable to the observed gaps that have been associated with planet formation, and easily distinguishable. ALMA probes particles that are  $\sim 1$  mm in size but since mm-sized particles that are collisionally produced do not drift far from their parent bodies, they can be used to study the planetesimal disks that we model here. Future work is needed to study MMR gaps when collision among millimeter and sub-millimeter particles and radiative forces are taken into consideration. On the other hand, if the planet becomes very massive, the edge of the disk thins under its perturbations as larger mass planets excite the particles and move them to higher eccentricity orbits. In our simulations, the disk becomes too heavily eroded to distinguish the 2:1 MMR at  $6 - 7 M_J$ , making this the practical upper limit for the use of this technique for characterizing extrasolar disk-planet systems.

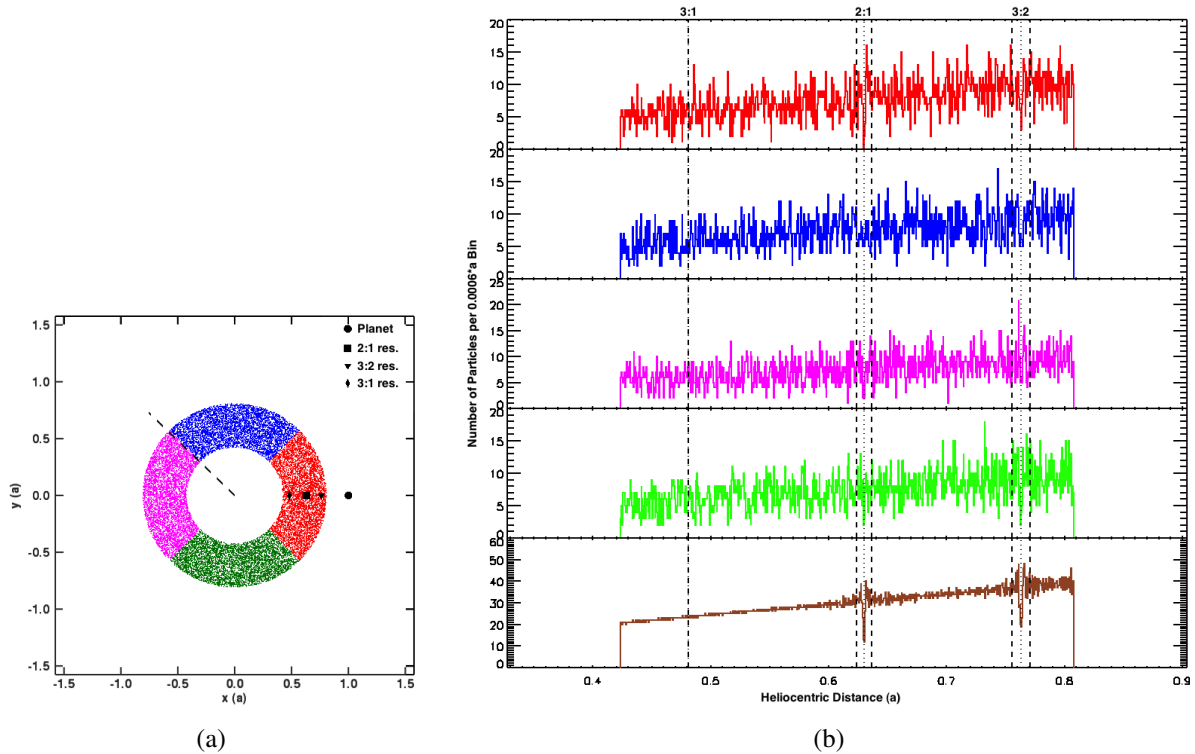


Figure 2.7: Though MMR gaps are not obvious in this example with a  $1.0 M_{\oplus}$  perturbing planet, examining the last histogram reveals two dips at the 2:1 and 3:2 MMR with the planet. Such small gaps might not be detectable in a telescopic image of the disk; nevertheless our simulations show that even an Earth-mass planet is able to open gaps in disks through MMRs. (a) No MMR gap is obvious in this simulated disk due to the small mass of the perturbing planet ( $M = 1.0 M_{\oplus}$ ). (b) Histograms for the four segments are noisy, but putting them together averages the noise out and reveals two narrow gaps at the 2:1 and 3:2 MMR with the planet.

### 2.5.3 Libration Width vs. Planet Mass

More massive planets are expected to open wider MMR gaps in disks. In Figure 2.8 we illustrate this effect by plotting libration width versus planet mass for interior (left) and exterior (right) resonances with planet's eccentricity  $e = 0.0$ , shown by the top two panels, while the bottom two panels show our results when the planet's eccentricity is increased to  $e = 0.0489$ . The different colors and symbols used and their least-square linear fits in each panel represent results obtained analytically using Equation 2.4 and from the simulations. It is clear that particularly in the case of interior resonances (left two panels), there is nearly perfect agreement between the 2:1 MMR gap widths obtained from the simulations and the ones calculated analytically while there is an offset between the measured and analytic results in the case of exterior resonances (right panels). Furthermore, as expected, increasing the planet's mass also increases the width of the MMR gap in all cases. Thus the mass of the perturbing planet, seen or unseen, can be estimated from the width of the resonant gap it produces.

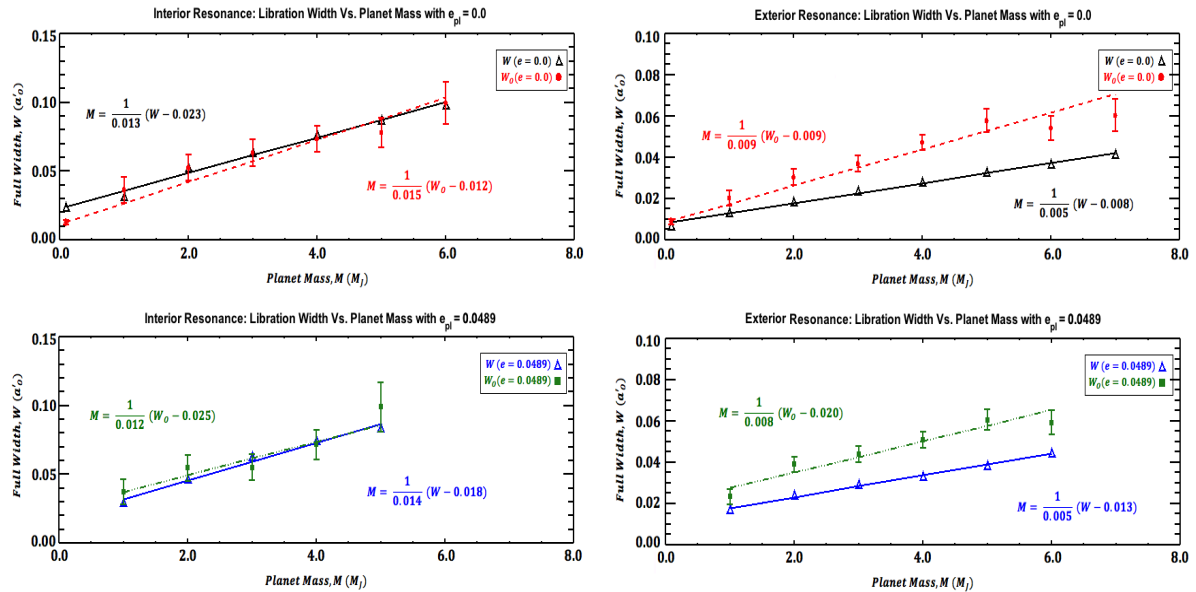


Figure 2.8: Libration width versus planet mass. Left panels: interior resonance with  $e = 0.0$  (top) and  $e = 0.0489$  (bottom). Right panels: exterior resonance with  $e = 0.0$  (top) and  $e = 0.0489$  (bottom).  $W$  and  $W_o$  are the theoretical and the simulated width of the gap, respectively, and are given in units of the observed mid-location of the gap ( $a'_0$ ). The vertical axis is the full width of the gap,  $2\sigma$  of the fitted Gaussian for the simulations.

Equations 2.6 through 2.9 are obtained from least square fits to the values we get from our simulations (see Figure 2.8). These equations allow one to easily calculate the planet's mass if the 2:1 MMR gap width can be measured observationally. To simplify the calculation, we normalize our results again, this time making the observed mid-location of the gap equal to one unit of distance. We do this so that the equations that are provided from this point forward can also be applied to cases where the planet is unseen but a MMR gap is detected in the debris disk.

(A) Interior Resonance with  $e = 0.0$ :

$$M = \frac{1}{0.015}(W_o - 0.012), \quad (2.6)$$

(B) Interior Resonance with  $e = 0.0489$ :

$$M = \frac{1}{0.012}(W_o - 0.025), \quad (2.7)$$

(C) Exterior Resonance with  $e = 0.0$ :

$$M = \frac{1}{0.009}(W_o - 0.009), \quad (2.8)$$

(D) Exterior Resonance with  $e = 0.0489$ :

$$M = \frac{1}{0.008}(W_o - 0.020), \quad (2.9)$$

where  $M$  is the planet mass (in Jupiter masses,  $M_J$ ) and  $W_o$  is the observed width of the gap (in units of the distance between the star and the observed gap).

The error bars are calculated by taking three main sources of uncertainty into account that are added in quadrature:

1) The Gaussian fit to the histogram is made by least-square fitting using *Interactive Data Language* (IDL) and the goodness of fit is recorded as one source of uncertainty. This value is

generally small in the examples we tried.

2) Since the Gaussian fit is made to points that mark half the bin size, the measurements have uncertainties that are affected by the choice of the bin size (taken to be 0.006 times the planet’s distance from the star in this work). However, the uncertainty in each bin position goes as  $\sqrt{N}$ , where  $N$  is the number of particles in the bin; and since we chose the bin size such that on average each bin contains not more than 0.25% of the total number of particles in the disk, the uncertainty due to the finite size of the bin is usually not significant.

3) Examining the shapes of the MMR gaps in our simulations revealed that gaps are not always perfectly Gaussian in shape. This is illustrated, for instance, in the top panel of Figure 2.3(b) where the gap is higher at one end. Therefore, in order to find the width of the gap, the Gaussian fit is made three times by normalizing to either side and also without normalization. The standard deviation between the three values obtained is then taken as the uncertainty in the gap width and is the dominant source of uncertainty in our calculations. It must be noted that our results for the gap widths are shown in terms of each gap’s standard deviation while an observer measuring the width of the gap might define the edges by measuring the peak brightness in the disk near the edge, then locating the radius in the gap at which the brightness of the disk is half that value. This method of using the “half-maximum radius” is used by Chiang et al. (2009) for simulations of the Fomalhaut disk. Nevertheless, the two quantities are related by a simple formula shown by Equation 2.10:

$$FWHM = 2 \sqrt{2 \times \ln 2} \sigma, \quad (2.10)$$

where  $FWHM$  is the full width at half maximum and  $\sigma$  is the standard deviation ( $W_o$  in our equations).

### 2.5.4 Resonant Location Versus Planet Mass

Examining the 2:1 MMR gaps in our histograms suggest that there is a shift in the position of the gap (the peak of the Gaussian fit) from the nominal resonance location (the dotted lines on the histograms). In fact, our simulations show that the offset from the gap's theoretical position is proportional to the mass of the planet. This is shown in Figure 2.9 where the top and bottom panels are for interior and exterior resonances, respectively. The red squares show the location of the 2:1 resonance with a zero-eccentricity planet while the diamond symbols in green are for the case of higher eccentricity planet with  $e = 0.0489$  and the dotted lines denote the location of the nominal resonance calculated using Equation 2.2 for interior and exterior resonances. The uncertainties in the observed gap locations are calculated in the same manner as those for the gap widths, explained in Section 2.5.3.

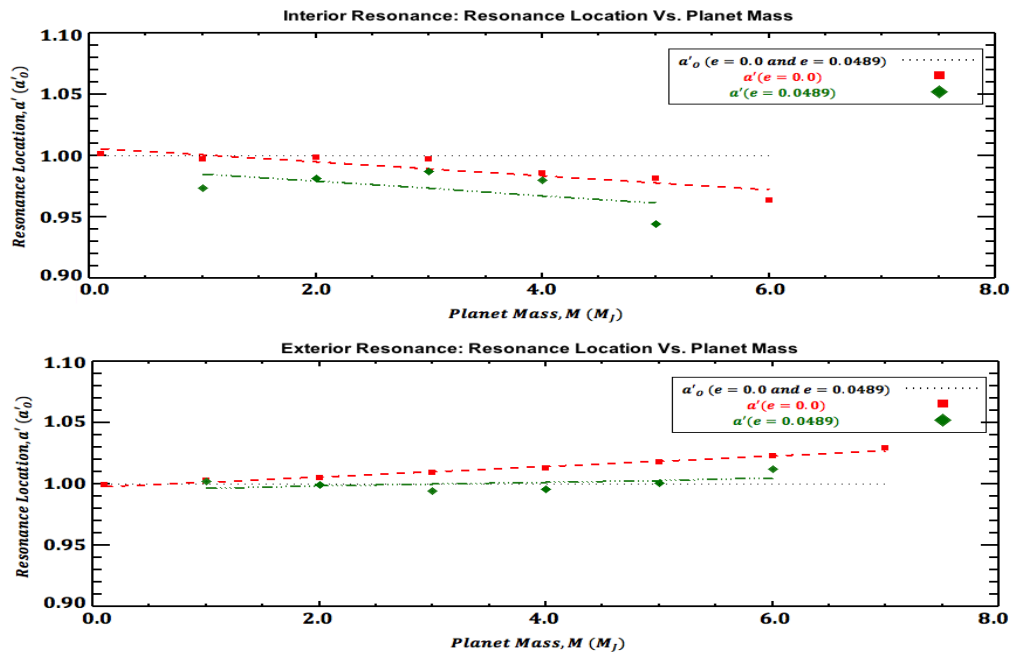


Figure 2.9: The effect of planet's mass and eccentricity on the resonant location for interior (top) and exterior (bottom) resonances. The red squares and the green diamonds show the theoretical gap locations for cases with  $e = 0.0$  and  $e = 0.0489$ , respectively while the dotted lines show the locations of the observed gaps.

In addition to a shift in the resonance location, we note from Figure 2.9 that the MMR gaps always tend to shift toward the planet as can be seen from the negative slope in the top panel and the positive slope in the bottom panel. We find that there is small contribution from the planet's eccentricity in shifting the locations of the MMR gaps. In addition, our results indicate that the location of the 2:1 gap agrees better with the theoretical prediction for the higher eccentricity planet in the exterior resonance case. Note that in Chapter 3 we interpret this offset as an effect that is due to the planet's forced eccentricity onto the disk particles which causes the disk's center of symmetry to be offset from the star and forces the particles into pericenter alignment. We therefore propose a different method to calculate the planet's semimajor axis in 3 which we recommend to be followed for the calculation of the planet's semimajor axis.

### 2.5.5 Finding the Planet's Semimajor Axis based on the Observed Gap Width and Location

If the mid-location and the width of a MMR gap can be obtained through observations, this information can be used to calculate the planet's semimajor axis. This could be useful for calculating the orbit of a known planet or determining the location of an unseen one. This calculation is done by first measuring the distance from the star to the center of the gap,  $a'_o$  and then finding the gap width in units of the observed star-gap separation. Then Equations 2.6 through 2.9 can be used to obtain the planet's mass. The theoretical location of the gap,  $a'$ , (i.e. the nominal resonant location) can then be found through the following equations:

(A) Interior Resonance with  $e = 0.0$ :

$$a' = -0.003 M + 0.002 + a'_o, \quad (2.11)$$

(B) Interior Resonance with  $e = 0.0489$ :

$$a' = -0.002 M - 0.015 + a'_o, \quad (2.12)$$

(C) Exterior Resonance with  $e = 0.0$ :

$$a' = 0.004 M - 0.001 + a'_o, \quad (2.13)$$

(D) Exterior Resonance with  $e = 0.0489$ :

$$a' = 0.001 M - 0.002 + a'_o, \quad (2.14)$$

where  $M$  and  $a'$  have units of Jupiter mass ( $M_J$ ) and  $a'_o$ , respectively. Finally, the semimajor axis of the planet can be calculated using Equation 2.2. Equations 2.11 through 2.14 were obtained by subtracting the observed gap location from its theoretical location in our simulations. This is shown by Figure 2.10 which can be used to obtain the theoretical MMR gap location from which the planet's semimajor axis is found.

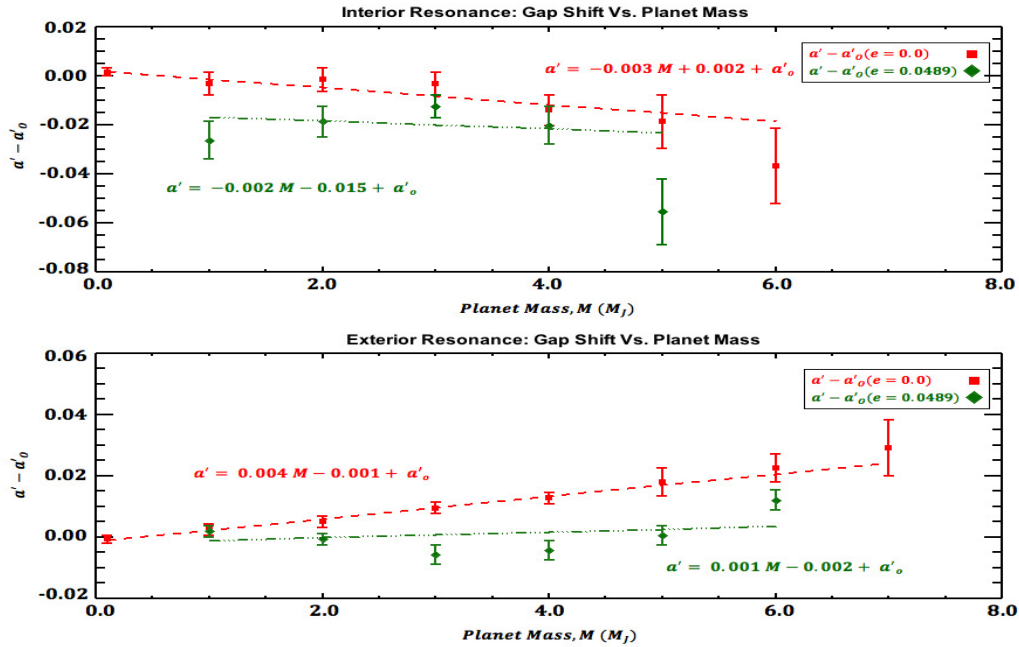


Figure 2.10: The shift in the gap location versus the planet's mass for interior (top) and exterior (bottom) resonances for two different planet eccentricities. The symbols used are the same as those in Figure 2.9.  $a'$  and  $a'_o$  are the theoretical and observed location of the gap, respectively.



### 2.5.6 The Effect of Planet's Orbital Eccentricity and Lindblad Resonances

When the planet is given a small but non-zero eccentricity, the 2:1 MMR properties remain largely unaffected. However, tightly wound spiral waves originating from the 3:1 MMR appear in some cases. These features are potentially valuable sources of information about the disk's properties, but are far more challenging to detect in real telescopic images than the gaps associated with the MMRs that we have been discussing so far. In fact, they often appear at scales below those shown in the previous figures, their primary visible tracer being a narrow arc-like gap at the 3:1 interior or exterior resonance.

We interpret these features as forced eccentricity waves originating at Lindblad resonances (Shu, 1984). These waves are similar to those seen in Saturn's rings (e.g. Holberg et al., 1982; Lane et al., 1982) and have the characteristic decrease in wavelength as one moves away from the resonance (Murray & Dermott, 1999). This is illustrated by Figure 2.11 which shows a series of density waves originating from the 3:1 resonance.

These waves are seen to be produced primarily at the 3:1 MMR for both internal and external planetary perturbers and are likely the reason we see an extra feature at the 3:1 resonance with the planet whenever the planet is given non-zero eccentricity in our simulations (see Figures 2.4 and 2.6). These coincide with the location of the  $m = 2$ ,  $k = \pm 1$ ,  $p = 0$  inner/outer Lindblad resonances, which are associated with similar waves in Saturn's rings. Though such structures are a rich source of information about the planet and the disk itself, the propagation of waves in real systems depends on effects such as self-gravity and collisions (Fridman & Gorkavyi, 1999) which are not modeled here, and we will leave their examination for future work.

Although the 3:1 MMR gaps are narrower and more difficult to measure than the 2:1 gaps, if they can be detected, their relative location with respect to that of the 2:1 resonance can be used to also distinguish interior from exterior resonances as the 3:1 resonance gap is formed farther from the planet than the 2:1. We will leave detailed examination of resonant interaction between disk particles and higher eccentricity planets to a follow-up paper.

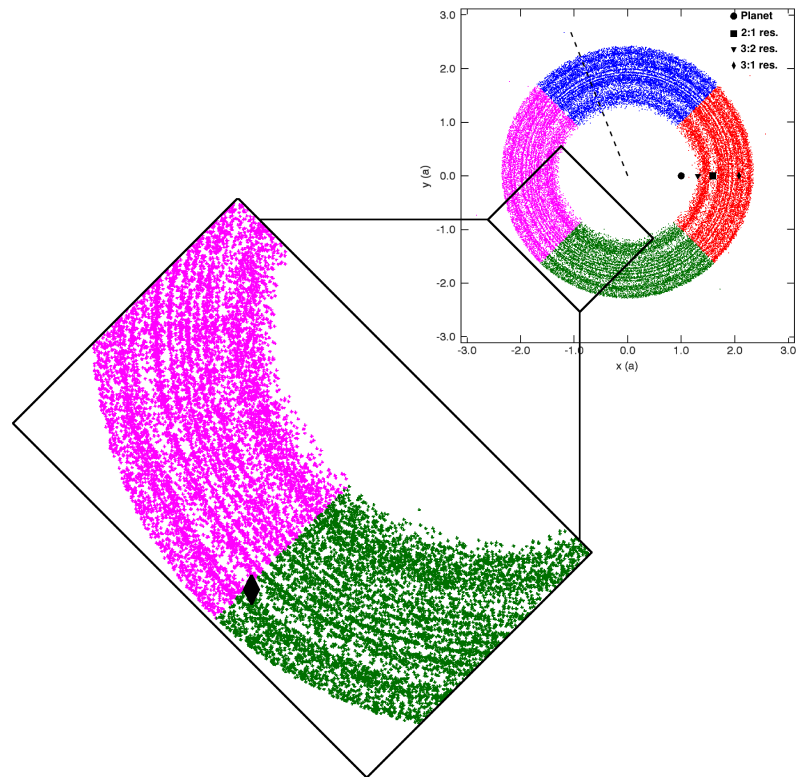


Figure 2.11: Spiral patterns appear commonly in our simulations when the perturbing planet has non-zero orbital eccentricity. These are likely forced eccentricity waves originating at Lindblad resonances. Our simulations indicate that these waves are generated at a location corresponding to the the 3:1 MMR with the planet, marked by a diamond on this figure.

### 2.5.7 Disk Optical Depth and Gap Contrast

Though the gap widths can easily be measured in simulations, this may prove more difficult observationally. In particular, the optical depth in the gap versus the disk as a whole will determine the amount of contrast in the image. Figure 2.12 shows the ratio of the average disk surface density to that at the deepest part of the 2:1 MMR gap (the “contrast”), as a function of planet mass. Because of the difficulty of defining the edges of the gaps, we do not try to define an edge-to-center contrast. Though higher mass planets form larger gaps, the contrast is somewhat diminished by particles “bleeding” in from the edges of the gaps. There is a trend for the contrast to increase with mass for a planet that is interior to the disk (Figure 2.12, bottom panel) but there is little effect for an external perturber (Figure 2.12, top panel). Thus the gap contrast itself can provide a measure of the planet mass in some cases, though this approach is observationally more difficult. Nonetheless, the contrast remains at large values through the range of planet masses considered here, indicating that the MMR features discussed here should be detectable if the disks themselves are.

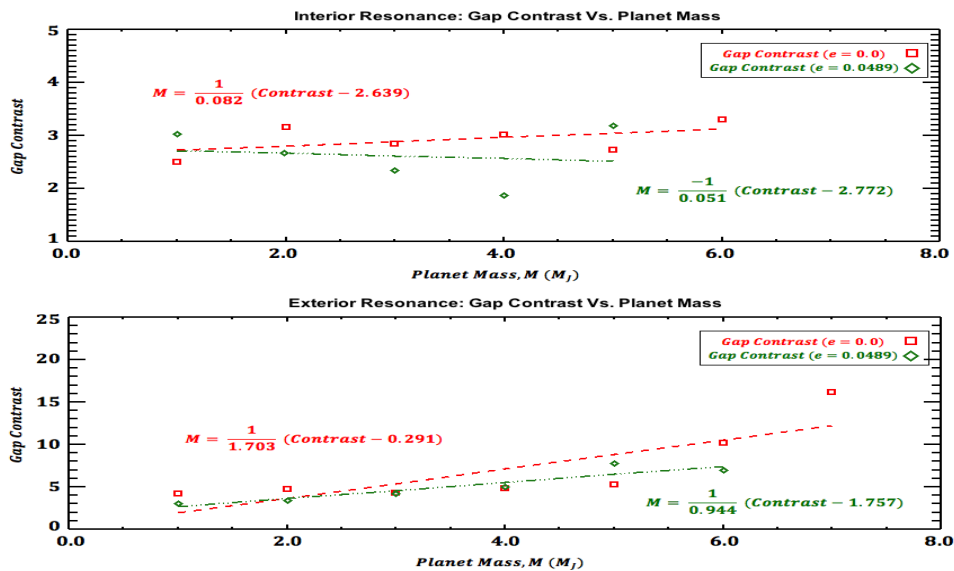


Figure 2.12: MMR gap contrast vs. planet’s mass (in Jupiter mass) for interior (top) and exterior (bottom) resonances.

We note from our results that the contrast grows almost linearly with planet mass, except

for exterior resonance with a planet on a circular orbit in which case there seems to be an exponential trend. However, we feel it is unwarranted to fit an exponential to this case for two reasons: First, the appearance of exponential growth is only present for one of the four cases (exterior resonance with a planet having  $e = 0$ ) and rests on only the two rightmost points. Moreover, those two points are near the largest masses beyond which the gaps disappear due to heavy erosion of the disk edge; and so the graphs should not be extrapolated beyond the presented maximum value.

Simulated observations of the disks shown earlier in Figures 2.3(a) and 2.5(a), are illustrated in Figures 2.13 and 2.14 assuming an inverse-square dependence of particle emission on distance from the central star. It must be noted again that in this study, we assume that disks are optically thin. These simple figures are free of additional noise that would certainly be present in real observations. The pixel size is chosen to match ALMA's highest resolution at 1 mm wavelength (15 mas for the 16 km configuration) at the distance of HL Tau (130 pc) if the disk's outer radius is 100 AU. Since the MMR gaps can still be seen in these images, we conclude that the MMR features described here are nominally within the reach of current observational facilities.

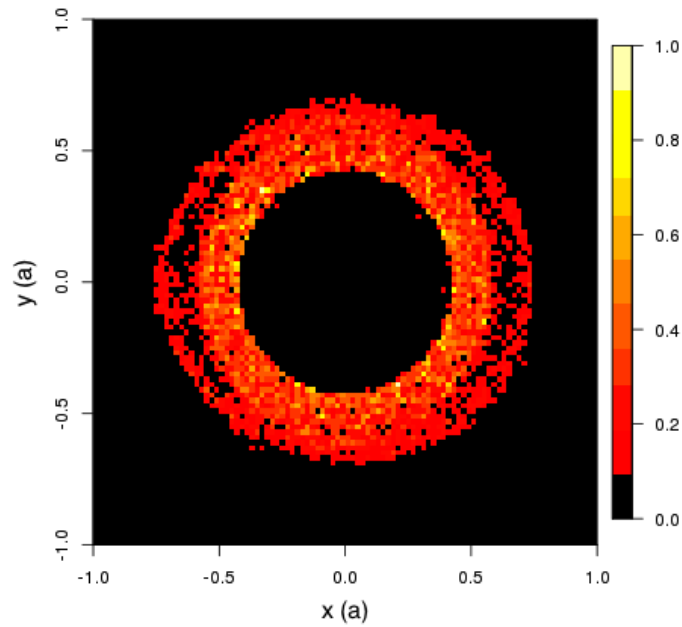


Figure 2.13: Same as Figure 2.3(a) for interior resonance except that particles in  $x$  and  $y$  are binned and assigned a color based on the total emission from each bin, normalized to the peak intensity. Darker colors correspond to less emission.

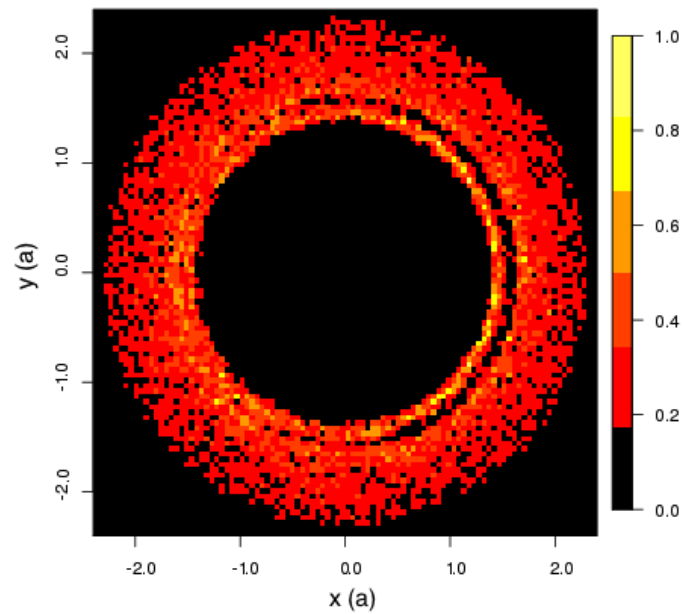


Figure 2.14: Same as Figure 2.13 but for the case of exterior resonance. The same disk is shown in Figure 2.5(a).

## 2.6 Summary and Conclusions

We investigated the dynamical effects of a planet on a planetesimal disk through MMRs for both interior and exterior resonances. Our purpose is to use the observed properties of MMR structures to characterize the planet producing them, even if that planet remains as-yet undetected.

Structures arising from MMRs can be highly diagnostic of the properties of the planet disturbing the disk particles. MMR gaps become wider as the planet’s mass increases; we found a linear relationship between the gap width and the perturbing planet’s mass that agreed well with theoretical calculations. Therefore, measurement of the width of a 2:1 MMR gap would help determine the perturbing planet’s mass, even if it remains unseen. We found gaps at the 2:1 and 3:2 MMRs even for a planet as small as  $1.0 M_{\oplus}$ , although their small widths make them observationally more challenging to detect than those at Jupiter masses. On the other hand, at planet masses beyond  $6 - 7 M_J$ , the resonance structures are destroyed as the disk is eroded by the planet’s growing Hill Sphere.

We found an offset in the gap’s position in the disk from the nominal resonant location with more massive planets causing a larger shift in the observed location of the gap. Thus if the planet’s location is already known, the shift from the theoretical location of the 2:1 MMR gap can be used to confirm the planet’s mass, which can alternatively be calculated using the gap width. On the other hand, for cases in which the planet remains undetected, we proposed a set of equations that take the planet’s mass, calculated using the gap width, to determine the planet’s location based on that of the observed 2:1 gap.

We further extended our studies to simulations of systems in which the perturbing planet has non-zero orbital eccentricity. In this case, disk structures due to MMRs become more complicated and the 2:1 MMR gaps formed by an internal perturber become more annular in shape. Moreover, an extra arc-like feature was seen at the 3:1 MMR with the planet when the planet’s eccentricity was increased and is associated with spiral waves generated at Lindblad resonances. Thus the appearance of an arc-shaped gap at the 3:1 resonance with the planet

is indicative of the planet having non-zero eccentricity. If detected, it could also be used to distinguish interior from exterior resonance. This would be helpful, particularly for the case of exterior resonance with a non-zero eccentricity planet for which we found the 2:1 gaps to become azimuthally symmetric. We obtained nearly perfect agreement between the 2:1 gap widths measured analytically and through our simulations for a planet exterior to the disk with 0 or 0.0489 orbital eccentricity. On the other hand, the difference between the two measurements seems to grow with mass for a planet on a circular orbit interior to the disk while a systematic shift is seen when the planet's eccentricity is increased to that of Jupiter's in this case. All the simulations we report on here were performed for flat disks with the perturbing planet in the same orbital plane as the disk particles, but we found no significant difference in our results when the planet, and thus the particles, were given a small orbital inclination.

The results of our simulations indicated that the shapes of the gaps opened by the 2:1 MMRs are different for interior versus exterior resonances, with the former making two sectors at the planet's inferior and superior conjunctions while the latter forms a single arc at opposition. Since direct detection of extrasolar planets still remains observationally challenging, detection of such structures in a planetesimal disk allows one to not only infer the presence of an unseen planet, the two distinct gap shapes would also make it possible to easily determine the relative location of the planet with respect to the disk and to distinguish MMR gaps from azimuthally symmetric gaps formed by a planet that is embedded in the disk. As ALMA and other facilities continue to advance the frontiers of extrasolar planetary science, the ability to detect and characterize unseen planets based on their effects on a more-easily observable disk will become an increasingly powerful tool.

# Bibliography

Asteroids Dynamic Site (<http://hamilton.dm.unipi.it/astdys/>).

Augereau, J. C., Nelson, R. P., Lagrange, A. M., et al., *A&A*, 370, 447.

Aumann, H. H., Beichman, C. A., Gillett, F. C., et al., 1984, *ApJ*, 278, L23.

Brown, J. M., Blake, G. A., Qi, C., et al., 2009, *ApJ*, 704, 496.

Burrows, C. J., Krist, J. E., Stapelfeldt, K. R., & WFPC2 Investigation Definition Team., 1995, in *BAAS*, Vol. 27, 1329.

Cataldi, G., Brandeker, A., Olofsson, G., et al., 2015, *A&A*, 574, L1.

Chiang, E., Kite, E., Kalas, P., et al., 2009, *ApJ*, 693, 734.

Debes, J. H., Jang-Condell, H., Weinberger, A. J., et al., 2013, *ApJ*, 771, 45.

Fridman, A. M. and Gorkavyi, N. N., 1999, *Physics of Planetary Rings. Celestial Mechanics of Continuous Media* (New York: Springer).

Heap, S. R., Lindler, D. J., Lanz, T. M., et al. 2000, *ApJ*, 539, 435.

Holberg, J. B., Forrester, W. T., and Lissauer, J. J., 1982, *Nature*, 297, 115.

Isella, A., Pérez, L. M., Carpenter, J. M., et al. 2013, *ApJ*, 775, 30.

Jang-Condell, H. and Turner, N. J., 2013, *ApJ*, 772, 34.



- Juhász, A., Benisty, M., Pohl, A., et al. 2014, MNRAS, in press, arXiv:1412.3412.
- Kalas, P. and Jewitt, D., 1995, AJ, 110, 794.
- Kirkwood, D., 1867, *Meteoric Astronomy: A Treatise On Shooting-stars, Fireballs, & Aerolites*, Philadelphia, PA: J. B. Lippincott & Co.
- Kley, W. and Nelson, R. P., 2012, ARA&A, 50, 211.
- Kraus, S., Ireland, M., Sitko, M., et al. 2013, ApJ, 768, 80.
- Krivov, A. V., Queck, M., Löhne, T., et al., 2007, A&A, 462, 199.
- Kuchner, M. J. and Holman, M. J., 2003, ApJ, 588, 1110.
- Kwon, W., Looney, L. W., and Mundy, L. G., 2011, ApJ, 741, 3.
- Lagrange, A. M., Bonnefoy, M., Chauvin, G., et al., 2010, Science, 329, 57.
- Lane, A. L., Hord, C. W., West, R. A., et al. 1982, Science, 215, 537.
- Mouillet, D., Larwood, J. D., Papaloizou, J. C. B., et al., 1997, MNRAS, 292, 896.
- Murray, C. D. and Dermott, S. F., 1999, *Solar System dynamics* (Cambridge: Cambridge Univ. Press).
- Muto, T., Grady, C. A., Hashimoto, J., et al. 2012, ApJ, 748, L22.
- Nesvold, E. R. and Kuchner, M. J., 2015, ApJ, 798, 83.
- NRAO, 2014, “*Birth of Planets Revealed in Astonishing Detail in ALMA’s ‘Best Image Ever’*”, National Radio Astronomy Observatory (Press Release).
- Reche, R., Beust, H., Augereau, J. C., et al., 2008, A&A, 480, 551.
- Shu, F. H. 1984, in IAU Colloq. 75: Planetary Rings (Tucson, AZ: Univ. Arizona Press), ed. R. Greenberg & A. Brahic, 513.

Smith, B. A. and Terrile, R. J., 1984, *Science*, 226, 1421.

Stark, C. C. and Kuchner, M. J., 2009, *ApJ*, 707, 543.

Tamayo, D., Triaud, A. H. M. J., Menou, K., et al., 2015, *ApJ*, 805, 100.

van der Marel, N., van Dishoeck, E. F., Bruderer, S., et al. 2013, *Science*, 340, 1199.

Wilner, D. J., Holman, M. J., Kuchner, M. J., et al., 2002, *ApJ*, 569, L115.

Wisdom, J. and Holman, M., 1991, *AJ*, 102, 1528.

Wyatt, M. C., 2003, *ApJ*, 598, 1321.

Wyatt, M. C., 2005, *A&A*, 433, 1007.

Wyatt, M. C., 2006, *ApJ*, 639, 1153.

## **Chapter 3**

# **Detection and Characterization of Extrasolar Planets through Mean-Motion Resonances. II. The Effect of the Planet’s Orbital Eccentricity on Debris Disk Structures**

*This chapter is adapted from: Tabeshian, M. & Wiegert, P. A., 2017, ApJ (submitted).*

### **3.1 Introduction**

Stars that exhibit excess infrared emission are thought to host disks of circumstellar material known as “debris disks”, with the extra emission being linked to heating and re-radiation by the constituent particles. Such disks are believed to be remnants of the cloud of gas and dust that formed the star but which have not coagulated to form planets. Particles that make up debris disks range in size from planetesimals with radii of a few hundreds of kilometers to

small sub-micron size dust grains. The infrared excess comes from the smaller grains which produce a second “bump” in the star’s blackbody curve. In this manner, in 1984 a debris disk was discovered outside the Solar System for the first time. Using *IRAS* data, the Spectral Energy Distribution of the main-sequence star Vega was found to have an infrared excess. Detailed analysis indicated the presence of circumstellar dust particles with radii greater than a millimeter and the mean distance of 85 AU from the star (Aumann et al., 1984). Since then, many extrasolar debris disks have been detected using optical to submillimeter observations (see the review paper by Wyatt, 2008).

Particles in the smallest end of the size distribution (sub-micron) are blown away by stellar radiation pressure over very short (orbital) timescales. At slightly larger sizes, the Poynting-Robertson (PR) drag is effective in removing dust grains on bound orbits with  $1 \mu\text{m} < s < 1 \text{mm}$  over timescales of  $\sim 10^4$  years (Klačka & Kocifaj, 2008). However, this effect can safely be ignored when studying debris disks since the timescale for the inspiralling of dust due to the PR drag is typically longer than its collisional lifetime and therefore particles are collisionally ground down to small sizes and blown out of the system by stellar radiation before spiralling inward (Wyatt et al., 1999). The justifications for neglecting radiation effects in our simulations will be examined in more detail in Section 3.2.3.

A planet in the vicinity of a debris disk may leave its signature in the disk structure. Before the gas in a protoplanetary disk is blown away by stellar radiation, drag against the gas causes dust particles to settle into circular orbits in the same plane as the plane of rotation of the star. However, if the system contains a planet on an elliptical orbit, particle orbits are perturbed such that the disk would lose its circular shape and the center of its symmetry becomes offset from the star (see Section 3.2.2 below). Moreover, if the planet is not in the same orbital plane as the disk, its dynamical effect on the disk particles may reveal itself as a warp in the disk. For instance, the warped inner disk around the star  $\beta$  Pictoris, first noted by Burrows et al. (1995) through imaging in optical scattered light using the Hubble Space Telescope and followed up by ground-based Adaptive Optics observations in the near-infrared by Mouillet et al. (1997),

was believed to be an indication of dynamical interaction with a previously undetected planet on an inclined orbit to the disk particles' (see Augereau et al., 2001). This hypothesis was later endorsed and confirmed when direct imaging revealed an inclined planet just outside the innermost belt of  $\beta$  Pic (Lagrange et al., 2010).

In addition to offsets and warps which are believed to be caused by the perturber's orbital eccentricity and inclination, structures can be formed in the disk through the particles' gravitational interactions with the planet via mean-motion resonances (MMRs). Two bodies are said to be in mean-motion resonance if their orbits are commensurable, meaning that for every  $p$  number of times one of them orbits the star, the other completes  $p + q$  orbits, where  $p$  and  $q$  are positive integers, with the latter ( $q$ ) defining the order of the resonance. This could have one of two consequences for the orbit of the less massive body: If it avoids close encounter with the planet at conjunction, a stable resonance is formed, otherwise the repeated perturbation of the orbit of the less massive body results in a change of its orbital elements.

If the former scenario occurs, particles accumulate at MMRs. In fact, dust density enhancements have been observed in debris disks and are attributed to the trapping of dust particles in exterior MMR with a planet. This was suggested theoretically by Gold (1975) who proposed that as interplanetary dust spirals inward due to the PR drag, dust particles can fall into MMR with a planet interior to their orbits. This could make their orbits temporarily stable despite the PR effect and their lifetime can be extended by a factor of a few to 10 up to  $\sim 100,000$  yrs (Jackson & Zook, 1989). In this case Gold (1975) argued that ring-like circumstellar structures with particle densities in the order of  $10^4$  times larger than average could be formed. This also explains the stability of some dust particles in the Solar System's zodiacal cloud, observed in the *IRAS* and *COBE* data, where particles are trapped by the Earth (Dermott et al., 1994).

Alternatively, Wyatt (2003) suggests that planet migration at an earlier stage in the life of a planetary system could also trap particles in resonances and result in the formation of clumpy structures in debris disks. Wyatt (2003) proposes that migration history of a system can be understood by studying the planet's signature in the observed spatial distribution of particles in

the debris disk. This scenario has been used to explain the capture of Pluto and the Plutinos in Neptune's 3:2 MMR. The outward migration of Neptune's orbit could have resulted in trapping of smaller bodies in exterior 3:2 MMR (see for instance, Malhotra, 1995; Hahn & Malhotra, 1999).

Density enhancements due to resonant dust trapping might have been observed in some extrasolar dust disks. For instance, submillimeter observations of the debris disk around  $\epsilon$  Eridani using the James Clerk Maxwell Telescope showed a dusty ring 60 AU from the star with four emission peaks (Greaves et al., 1998). These could be explained as structures formed by dust particles captured in 3:2 exterior MMR with a  $\sim 0.2$  Jupiter-mass ( $M_J$ ) planet on a circular orbit 55-65 AU from the star (Ozernoy et al., 2000). Later works have come to somewhat different conclusions (the mass, semimajor axis and eccentricity of the planet have been determined to be  $0.1 M_J$ , 40 AU and 0.3, respectively, while the four peaks of emission have been attributed to the trapping of dust particles in 3:2 and 5:3 exterior MMR with the planet at periastron (Quillen & Thorndike, 2002)); nevertheless, the existence of resonant structures in disks has not been disputed. In another example, Wilner et al. (2002) detected two dust emission peaks in Vega's dusty disk using the *IRAM* interferometer at 1.3 mm wavelength. They attributed this to the trapping of dust, via dust migration under PR drag, into 2:1 and 3:1 resonances with a  $3 M_J$  planet having an orbital eccentricity  $e = 0.6$ . Again in this case, alternative resonant models were shown to be consistent with observations. Wyatt (2003) proposed that the observed dust overdensity is due to particles trapped in 2:1 and 3:2 MMR by migration of a Neptune-mass planet from 40 to 65 AU over a period of 56 Myr. Regardless of the capture mechanism, the formation of dust density structures due to MMR can be taken as an indication of the presence of a planet, whose mass and orbital parameters may be determinable through the properties of the affected dust population.

Whereas resonant dust trapping and its implication on planet detection and characterization have been discussed to some extent in the literature, not much emphasis has been placed on understanding structures formed by resonant gap formation in extrasolar debris disks which is

the focus of the present study in an attempt to understand how such resonant gaps could be diagnostic of planetary parameters without the need to observe the planet itself.

The location of each resonance can be found analytically by simply considering the definition of MMR, which occurs when the mean-motion of one particle is a simple fraction of that of the other. Expressed in terms of the two particles' semimajor axes,  $a$  and  $a'$ , the resonance location for any  $p$  and  $q$  combination is expressed by Equation 3.1:

$$a' = \left( \frac{p+q}{p} \right)^{\frac{2}{3}k} a, \quad (3.1)$$

where  $k = +1$  for exterior resonance (i.e.  $a' > a$ ) and  $k = -1$  for interior resonance (i.e.  $a' < a$ ). Note that we adopt the same notation we used in our earlier paper, Tabeshian & Wiegert (2016), hereinafter referred to as *Paper I*, where the primed and unprimed quantities denote the orbital elements of the particle being perturbed (the “asteroid”) and the perturbing body (“the planet”), respectively. Also note that here we are interested in the effect of MMRs at locations specifically away from the planet’s orbit, and so we do not investigate the 1:1 MMR, neither are we concerned with gap clearing that occurs in the feeding zone of a planet due to its tidal interaction with the disk.

Periodic perturbations of a particle’s orbit by a more massive one can eventually result in significant changes in the orbit of the less massive body. Such perturbations cause the resonant argument of the disturbing function,  $\phi$  defined by Equation 3.2, to librate about a fixed value. If the amplitude of the libration becomes large enough, MMRs could eventually either remove the less massive particle from its orbit or the particle can stay in a bound orbit but it could gain some eccentricity. In either case, a gap develops due to the particles having been ejected from their orbits or having developed a large radial excursion that makes them spend a large fraction of their orbital period away from the location of the resonance. The resonant angle  $\phi$  is given by Murray & Dermott (1999) as:

$$\phi = j_1 \lambda' + j_2 \lambda + j_3 \varpi' + j_4 \varpi, \quad (3.2)$$

where  $j_1 = p+q$ ,  $j_2 = -p$ , and  $j_3$  and  $j_4$  are either zero or  $-q$  depending on the relative locations of the perturbing body and the one being perturbed, while  $\lambda$  and  $\lambda'$  are their mean longitudes and  $\varpi$  and  $\varpi'$  are their longitudes of pericenter. Therefore, the resonant argument,  $\phi$ , defines the angle between the longitude of the conjunction of the two bodies and the longitude of the pericenter of the object with the larger semimajor axis. To lowest order in eccentricity, the maximum libration width,  $\delta a'_{max}$  at each first and second order resonance can also be calculated using equations (8.76) and (8.58) of Murray & Dermott (1999).

In debris disks, resonant interaction with planets could cause the formation of gaps which may or may not be observable telescopically depending on disk particle eccentricities as will be discussed briefly in Section 3.4. Such gaps have been observed in numerical simulations of debris disks by some authors but have not been extensively studied. For instance, in an attempt to understand gravitational sculpting of a single planet orbiting interior to the Fomalhaut disk, Chiang et al. (2009) shows that resonance gaps could form for a variety of planet mass-semimajor axis combinations. However, the authors do not take the discussion further to describe how such structures would help characterize the planet causing them. Furthermore, simulations by Nesvold & Kuchner (2015) show a gap in the disk's surface brightness distribution at the 2:1 MMR with a  $3 M_J$  planet at 50 AU. Though the authors address depletion of planetesimals at this resonance, they do not discuss how it can yield measurements of planetary parameters. Similarly, in Reche et al. (2008) an example of a non-migrating planet interior to a simulated disk that has three gaps whose locations correspond to the 3:2 and 2:1 exterior MMR with the planet is shown, but they are not addressed by the authors. Nevertheless, the locations and appearance of the 2:1 gap in their figure resemble our results in this paper. These illustrate the rich variety of structures that can be created by resonances, and the need to understand this process and what it tells us about the system.

This work focuses on structures formed by resonant gap formation in debris disks through gravitational interaction with a single non-migrating planet and the consequent formation of what would be analogous to the Solar System's Kirkwood gaps (Kirkwood, 1867). Our Solar



System's Kirkwood gaps are complicated by multi-planet effects such as secular resonances, but we leave to a future work the study of MMR gap formation in planetary systems with more than one planet.

We argue that under certain conditions, the gaps discussed in this paper could be visible in telescopic images of debris disks. We showed in *Paper I* that dynamical interactions of a single planet with a gas-poor and dynamically cold planetesimal disk can result in formation of azimuthally asymmetric gaps whose widths and locations are diagnostic of the perturber's mass and semimajor axis, even if the planet remains unseen. We restricted our analysis to systems in which the perturbing planet was either on a circular orbit or had a small,  $\sim 0.05$ , orbital eccentricity. However, unlike planets in our own Solar System, most exoplanets found to date have significant eccentricities (see the review paper by Winn & Fabrycky, 2015). Therefore, here we extend our analysis of planet-disk interactions and resonance gap formation to systems with the planet on a range of higher eccentricity orbits in order to provide a more complete picture of the gap formation that results from resonant interactions between a single planet and a planetesimal disk. Here we study dynamic structures of planetesimals in dynamically cold systems and assume that radiation and PR drag forces can be neglected as will be addressed in more details in Section 3.2.3 and following a similar treatment in our previous work. We find that MMR gap structures would be detectable in telescopic images of disk systems hosting planets on moderately eccentric orbits, though the resulting disk structures are more complex than in the low eccentricity case.

We start this paper by describing in Section 3.2 how the disk is dynamically affected by a planet on a non-circular orbit where we also discuss the importance of radiation forces in debris disks. For our simulations, we use the same numerical method as in *Paper I* (which we go over briefly in Section 3.3) but our initial conditions are different, appropriate to a debris disk with a planet on an eccentric orbit. We present our results for both interior and exterior MMRs in Section 3.4 and discuss their implications in Section 3.5 where we also show how our simulated disks would look like if observed by the *Atacama Large Millimeter/submillimeter*

Array (ALMA). We end by a summary and conclusions in Section 3.6.

## 3.2 Disk Dynamics

Here we will assume for simplicity a quiescent and dynamically cold disk perturbed by a single non-migrating planet. However, the addition of a massive eccentric planet means that the particles in the disk cannot travel on perfectly circular orbits but are forced to take on minimally eccentric orbits. Such a disk, which corresponds to particles with a forced eccentricity but no free eccentricity, will be briefly outlined.

### 3.2.1 Forced Eccentricity and Longitude of Pericenter

When the perturbing planet has non-zero orbital eccentricity, it imposes an eccentricity onto the disk particles. This is referred to as the particles' *forced eccentricity* ( $e'_f$ ) and is given under the secular approximation by Equation 3.3 below (Murray & Dermott, 1999):

$$e'_f(a') = \frac{b_{3/2}^{(2)}(\alpha)}{b_{3/2}^{(1)}(\alpha)} e, \quad (3.3)$$

where  $\alpha = (\frac{a}{a'})^k$  while the  $b_s^j(\alpha)$  terms are the Laplace coefficients given by (Murray & Dermott, 1999):

$$b_s^j(\alpha) = \frac{1}{\pi} \int_0^{2\pi} \frac{\cos(j\psi)}{(1 - 2\alpha \cos(\psi) + \alpha^2)^s} d\psi. \quad (3.4)$$

Equation 3.3 is independent of the perturber's mass and applies if the system contains one perturber only. The forced eccentricity in such systems is also independent of time as the particles do not undergo any secular evolution (Wyatt et al., 1999). Therefore, forced eccentricity only depends on the eccentricity of the perturber and diminishes with distance from it. The particles could in principle have an additional component of their eccentricity, called the *free eccentricity*, but we will take this to be zero, as is appropriate to a dynamically

cold disk. In this case, the line of apses of the particles,  $\varpi'$ , aligns parallel to that of the planet.

In this study, we determine the maximum libration width at each MMR location by considering the forced eccentricity induced by a planet at the semimajor axis of each resonance, assuming that disk particles have negligible free eccentricity. Also the disk particles are taken to orbit the star in the same plane as the planet; therefore, we do not consider warps in the disk that could be caused by the forced inclination of the planet.

### 3.2.2 Disk Offset

The result of the eccentricity of the particles together with the alignment of their orbits with that of the planet is that the disk's center of symmetry is offset from the star by an amount that is related to the forced eccentricity of the particles' orbits. This causes an azimuthal brightness asymmetry in the disk.

The observed brightness asymmetry in the circumstellar disk around HR4796A was first postulated to be due to an offset caused by gravitational perturbations of the disk by a low-mass stellar companion or a planet on a non-circular orbit (Telesco et al., 2000). The nearly edge-on disk was found to be  $5.9\% \pm 3.2\%$  brighter in the northeast lobe than it is in the southwest lobe with a statistical significance of  $1.8\sigma$ . Dynamical modeling of the HR4796A disk by Wyatt et al. (1999) had suggested that a stellar or a planetary companion that could impose a forced eccentricity as small as 0.02 on the disk can cause the disk's center of symmetry to be offset from the star by  $\sim 2$  AU and could, therefore, be responsible for its observed brightness asymmetry. According to their model, in the absence of a stellar companion, a single planet with a mass of  $> 10 M_{\oplus}$  and an eccentricity of  $> 0.02$  can result in a 5% brightness asymmetry in the HR4796A disk, indicating that planets of moderate eccentricity could cause measurable offsets in debris disks. This phenomenon was dubbed the *pericenter glow* (since it results in the side of the disk closest to the star becoming warmer, and hence brighter, than the other) and has since been observed in other debris disks such as the the dusty disk around Fomalhaut, a disk that has an azimuthal brightness asymmetry and which is offset by 15.3 AU (Kalas et al.,

2005). The offset in the center of symmetry of debris disks is now known to be a signature of a companion, stellar or planetary, that is on an eccentric orbit and forces the orbital elements of disk particles into pericenter alignment. The resulting pericenter glow is, therefore, caused by the disk being closer to the star on the forced pericenter side, and hence warmer and brighter in the wavelength of observation.

In a recent study, Pan et al. (2016) show that azimuthal temperature asymmetries due to disk offset could be compensated by azimuthal asymmetries in dust density. At apocenter, particles travel more slowly and hence spend more time there, and so higher particle densities at apocenter could result in an apocenter glow instead. The authors argue that the apocenter/pericenter flux ratio is dependent on the wavelength of observation and suggest, through numerical modeling of the debris disks around Fomalhaut and  $\epsilon$  Eridani, that apocenter glow wins over the enhanced flux due to disk offset away from pericenter if observed at far-infrared and submillimeter wavelengths while the opposite happens at shorter wavelengths. We will revisit disk offset and apo/peri glow in Section 3.5.4.

### 3.2.3 The Importance of Radiation Forces in Debris Disks

In addition to the gravity of the star and the planet, important dynamical effects may in principle arise in debris disks from stellar radiation pressure and Poynting-Robertson (PR) drag. Here we will ignore these radiative effects, partly for simplicity and partly because there is a wide range of debris disks for which these effects will be negligible. This point has been argued more thoroughly elsewhere (see Wyatt et al., 1999) but it is important enough to our study that the main points will be reviewed here as an order-of-magnitude calculation.

Radiative effects can be parametrized by the ratio of the radiation force to the star's gravitational force ( $\beta$ ) which is a constant for a particular particle of a particular radius  $r_d$ . Extending the results of Weidenschilling & Jackson (1993) to stars of different luminosities ( $L_*$ ) the two are related through  $\beta = \frac{0.57 \times 10^{-6} L_*}{r_d L_\odot}$  at a density of  $1000 \text{ kg/m}^3$ , where  $r_d$  is in meters.

There are three broad classes of particle behaviors based on their size. The smallest par-

ticles ( $r_d \lesssim 0.57 \mu\text{m}$ ) are blown out of the system by radiation pressure. Intermediate-sized particles spiral into the star under PR drag, while the largest particles ( $r_d \gtrsim 500 \mu\text{m}$ ) are essentially unaffected. For example, a dust particle of radius  $500 \mu\text{m}$  has a PR inspiral timescale from 100 AU around a Sun-like star of order a Hubble time. The effects of radiation forces on such large particles can safely be ignored; it is the intermediate particles where they are most pronounced.

In a debris disk with a power-law size distribution like that of a collisional cascade,  $r^{-3.5}$  (Dohnanyi, 1969), most of the mass is in the largest objects (i.e. asteroids or planetesimals). However, the smaller dust particles will dominate the emission, and hence the observations. We expect the emission to be dominated by particles of sizes comparable to the wavelength at which we are observing. As a result, the above determination that PR drag is most effective on particles sizes from roughly 1 to  $500 \mu\text{m}$  means that radiation forces cannot be dismissed out of hand.

However, PR drag will have a negligible effect on our simulations if the collisional lifetime of dust is short compared to the PR timescale. That is, if inter-particle collisions reduce the dust to small particles (which will be blown out of the system by radiation pressure on a very short timescale, essentially the orbital timescale) quickly enough, they would not drift far enough to smear out any disk structures. Here we argue that the collisional lifetime of dust will be much shorter than the PR timescale in many (though not all) physically realistic debris disks. It must be noted that the small dust that is blown out of the system under the stellar radiation pressure can, in fact, smear or even completely wipe out exterior MMR gaps (see for instance the study by Kuchner & Stark, 2010); however, sub-micron dust does not dominate the emission at long wavelengths made by ALMA and other high resolution facilities that operate in the mm/sub-mm regime which we chose to focus on in this study. Therefore, observations taken at shorter (sub- $\mu\text{m}$ ) wavelengths are more subject to radiation forces; and any studies of disk structures at these wavelengths must include these effects.

For the PR timescale, Weidenschilling & Jackson (1993) calculate that for particles on

near-circular orbits, the rate of change of the heliocentric radius,  $R$ , is:

$$\frac{dR}{dt} = \frac{GM_*\beta}{Rc}, \quad (3.5)$$

where  $G$  is the Universal Gravitational Constant,  $M_*$  is the star's mass, and  $c$  is the speed of light. From this, the time to spiral into the star under the PR effect is just:

$$t_{PR} = \frac{R^2 c}{GM_*\beta}. \quad (3.6)$$

The collision timescale is more complicated. Here we will assume a power-law size distribution of the disk material like that of a collisional cascade (see Dohnanyi, 1969), with most of the mass in the large bodies (the asteroids) which are unaffected by the PR drag. The dust observed telescopically from Earth is continuously regenerated by asteroid collisions. A dust particle of radius  $r_d$  cannot be disrupted by a collision with a particle much much smaller than itself, and collides only rarely with particles larger than its size. Thus, it is most likely collisionally disrupted in a collision with a particle of roughly its own size or somewhat greater (see for instance, Wyatt et al., 1999). We approximate its collisional lifetime as the time until it takes to sweep out a volume which should include one other particle its own size:

$$t_{coll} = \frac{1}{n_d \pi r_d^2 v_{rel}}, \quad (3.7)$$

where  $v_{rel}$  is the particle's relative velocity, that is, the velocity above that of a purely circular orbit  $v_{orb} = \sqrt{\frac{GM_*}{R}}$ . The number density of dust particles,  $n_d$ , is the dust production rate,  $q_d$ , times the length of time dust survives, all divided by the disk volume  $V \sim \pi \frac{v_{rel}}{v_{orb}} R^3$ . If we consider survival against collisions only here, the survival time is  $t_{coll}$ , and  $n_d = q_d t_{coll} / V$ .

The dust production rate  $q_d$  is  $Q$  times the rate of asteroid collisions,  $c_a$ , times the relative asteroid and dust masses, where  $Q$  is the fraction of asteroid mass converted to dust per asteroid collision. Let's assume all asteroids are the same size,  $r_a$ , for simplicity. Then the collision

timescale for asteroids would be:

$$t_{coll,a} = \frac{1}{n_a \pi r_a^2 v_{rel}}, \quad (3.8)$$

where  $n_a$  is the number density of asteroids,  $N_a/V$ .  $N_a = \frac{3M_d}{4\pi r_a^3 \rho}$  is the total number of asteroids in a disk with mass  $M_d$ . From this, the dust production rate is:

$$q_d = Q \left( \frac{r_a}{r_d} \right)^3 c_a = Q N_a n_a \pi r_a^2 v_{rel} \left( \frac{r_a}{r_d} \right)^3, \quad (3.9)$$

and the dust number density is:

$$n_d = Q N_a n_a \pi r_a^2 v_{rel} t_{coll} \left( \frac{r_a}{r_d} \right)^3 / V. \quad (3.10)$$

Putting this back into our expression for  $t_{coll}$ , making the needed substitutions and rearranging, we get:

$$t_{coll} \sim \frac{4\pi R_d^3 \rho}{3M_d} \sqrt{\frac{r_a r_d}{QGM_*}} R^{0.5}. \quad (3.11)$$

In Figure 3.1, we plot the results for an asteroid size  $r_a = 1$  km, a star with mass  $M_* = 1 M_\odot$ , an asteroid and dust density  $\rho = 1000$  kg m<sup>-3</sup>, a dust production fraction  $Q = 0.01$ , and a disk with mass  $M_d = 1$  Earth-mass and radius  $R_d = 100$  AU. Four different particle sizes are considered from  $r_d = 3$   $\mu$ m to 100  $\mu$ m. The collisional lifetime of the dust is much shorter than the PR lifetime over most of the disk, though they cross over in the inner regions. Thus we expect that PR drag will be less important in the outer regions of debris disks, and when observations are taken at longer wavelengths. It is on the basis of this result that we choose to neglect radiation forces in this first look at the dynamical effects of planets on debris disks.

We do not claim that the PR drag is unimportant in all regions of all debris disks: indeed it is likely to be important in some physically realistic disks, particularly those of low mass where the dust component is sparse (and hence the collisional lifetime of dust is very long). However

such dust-poor disks are also likely to be fainter. Here we choose to study the brighter and simpler disks, recognizing the possible importance of the PR drag in some cases, particularly when observing at shorter (sub-micron) wavelengths, but leaving that work to a further study.

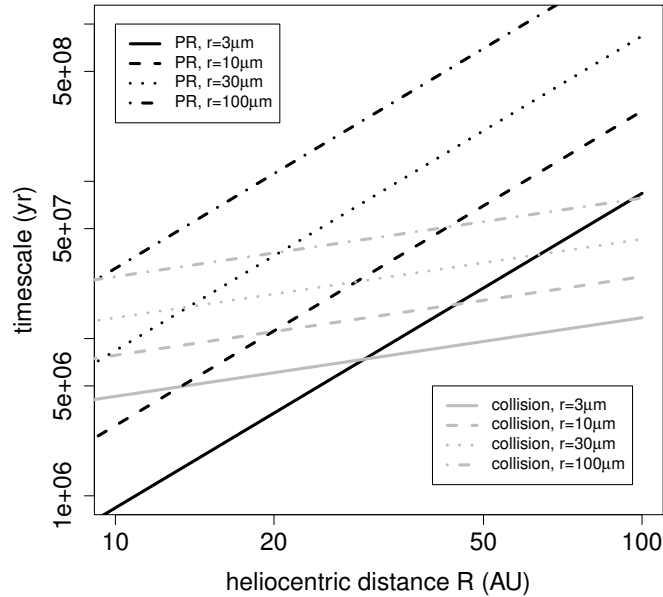


Figure 3.1: Comparison of the Poynting-Robertson inspiral timescales to the collisional life-times of dust particles in a debris disk. See the accompanying text for more details.

## 3.3 Simulations

### 3.3.1 The Method

The symplectic integrator used for our simulations is the same as in *Paper I*, which is based on the Wisdom-Holman algorithm (Wisdom & Holman, 1991). We examine two possible cases, of either interior or exterior MMR in a disk of planetesimals that interact gravitationally with a single planet orbiting a 1 Solar-mass star. For simplicity, we ignore gravitational interaction among disk particles as well as the radiation pressure and PR drag. Furthermore, we assume that little or no gas is remained in the disk. Thus our simulations represent planetesimal or debris disks that are gas-poor and dynamically cold (or at least as dynamically cold as they can



be, given the presence of the planet). Given that dust subject to drag forces was found by Wyatt (2005) to be quickly removed, we will neglect such particles and set  $\beta$ , the ratio of the force due to radiation pressure to the force of gravity, to zero as justified by our discussion presented in Section 3.2.3.

The simulations are run for 1 million years. This is found empirically to be more than long enough for MMR gaps to open up and for the disks to reach a quasi-steady state; indeed the formation of MMR gaps in our simulations typically becomes apparent in only a few orbital timescales of the planet and the gaps are already well established by  $\sim 10^4$  years. Timesteps of approximately 25 and 50 days are chosen when the planet is exterior and interior to the disk, respectively. The timestep is adjusted slightly at the beginning of the simulation so that the planet will be at apocenter at the end of the simulation for reasons of convenience that will be discussed in Section 3.4.

We measure the width and location of each MMR gap by means of fitting a Gaussian function to where the gap appears in a histogram of the particle distribution in the disk, as will be discussed in Section 3.4. The uncertainties in MMR gap widths and locations are calculated in the same way as in *Paper I* and come from three independent sources: (1) goodness of fit from least-square fitting to the histogram bins, (2) Poisson statistics of the particles in each bin, associated with the choice of bin size, and (3) the fit model. The different factors that contribute to the uncertainty in our calculations are then added in quadrature. Uncertainties due to the first two factors are generally small, particularly with our choice of the bin size (i.e.  $0.006 a$ ) which is small enough to ensure that at the beginning of the simulation and before the disk is perturbed, each bin contains about 1% of the total number of particles in the disk. However, given the fact that the MMR gaps we see in our simulations are not perfectly Gaussian, fitting such a model introduces uncertainty, particularly since the gaps are not necessarily symmetric about the mean. Therefore, we perform the Gaussian fitting three times and take the standard deviation between the values obtained for the median and width of the gap. The three ways that we do this are by first normalizing the height of each bin to the lower and higher edges of

the gap separately and fitting a Gaussian each time as well as applying no normalization before the Gaussian fitting. We find this to be the dominant source of uncertainty in our calculations.

### 3.3.2 Simulated Debris Disks

The simulations are set up with the perturbing planet having a semimajor axis equivalent to that of Jupiter (i.e.  $\sim 5.204$  AU); however, this choice is arbitrary since the physics involved scales with distance. As a result, our simulations are applicable to debris disks of all sizes; and so we normalize the scales by the planet's semimajor axis to have the planet at roughly unit distance. We vary the mass and the eccentricity of the planet over a range of values at the extremes of which the the disk is largely destroyed and/or the resonance gaps are completely eroded. Note that the planet is always placed either interior or exterior to the debris disk, as our interest here is not in the gap the planet clears about its orbit, but rather in structures that appear away from the orbit of the planet itself.

We place 10,000 particles per 1 AU of the disk's radial extent to be consistent with our previous work and choose the location of the inner and outer edges of the disk such that the three resonances being studied, i.e. the 2:1, 3:2 and 3:1, fall in the disk ( $1.204 AU < a'_D < 4.204 AU$  for the interior resonance and  $6.204 AU < a'_D < 12.204 AU$  for the exterior case). Note that the inner edge of the disk is extended 1 AU further inward for the interior resonance case compared to *Paper I* for the purpose of catching higher order resonance structures as the planet's eccentricity is increased (see Section 3.5.2). Also, we set initial particle eccentricities to the value of the eccentricity induced by the planet at each particle's semimajor axis, i.e. the forced eccentricity.

## 3.4 Results

The simulation results allow an examination of the spatial distribution of the disk and any resulting structures. Unlike our Solar System's Main Asteroid Belt where an externally-taken

telescopic image would not reveal the Kirkwood Gaps due to particle eccentricities smearing them out, the appearance and the size of MMR gaps in our simulated disks suggest such structures would likely be observable in telescopic images of some quiescent debris disks, as will be discussed in Section 3.5.5.

In order to study structures formed by MMRs, histograms of the number distribution of disk particles in heliocentric distance for different quadrants of the disk are made. The MMR gaps can be fit by a Gaussian function as a first approximation for comparison with the analytic measurements. Observers often measure gap widths by locating where the disk brightness drops to half the peak value around a gap (see for instance, Chiang et al., 2009). We choose the range for our Gaussian fitting in the same way here; however, it is often challenging to define the edges of the gaps in our simulations as the particle distribution is not smooth. The difficulty in defining the edges of the gaps and their asymmetries introduce an uncertainty in our calculations which was already addressed in Section 3.3.1.

In *Paper I*, it was shown that MMR gaps are often azimuthally asymmetric. Therefore, we again divide the disk into four equal segments, this time about the line of apses of the planet's orbit. This coincides with the line of apses of the disk particles due to their pericenter alignment with the planet (see Section 3.2.2). We then fit Gaussian functions to where the gaps appear and compare the width and location of each MMR gap to those analytical values found using the equations discussed in Section 3.1. Also provided are expressions for calculating the mass and some orbital parameters of the perturbing planet even if the planet itself is not resolved in the observations. Therefore, our technique is an indirect method to detect and characterize extrasolar planets in systems with debris disks.

One key finding of *Paper I* was that a slight increase in the eccentricity of the planet (i.e. when  $e = e_J = 0.0489$  with the subscript  $J$  referring to Jupiter) resulted in an extra gap appearing in the disk which opened at the 3:1 MMR with the planet. That work is extended here by varying the planet eccentricity to much higher values. We find that this gap becomes more prominent and that other higher order resonances also appear in the disk as the planet

eccentricity is increased further. Furthermore, we saw in *Paper I* that the width of a MMR gap is related to the perturber’s mass, and here again find that the properties of the gaps allow us to constrain the mass of the planet.

The eccentricity of the disks examined here means that one side is narrower by  $a'_{D_o} e'_{D_o} - a'_{D_i} e'_{D_i}$  at the pericenter side and wider by the same amount at the apocenter where  $a'_D$  and  $e'_D$  are the semimajor axis and eccentricity of the disk with the subscripts  $o$  and  $i$  denoting the outer and inner disk edges, respectively. Therefore, the theoretical locations and widths of MMR gaps in each segment need to be adjusted by  $\frac{1-e_f^2}{1+e'_f \cos(\nu')}$  where  $\nu'$  is the true anomaly of the particles’ orbits at the center of each segment and is taken to be  $0^\circ$  and  $180^\circ$  in the two segments whose centers lie on the line of apses at pericenter and apocenter, respectively, and  $90^\circ$  and  $-90^\circ$  in the other two segments.

At the same time, increasing the mass of the perturber causes the disk edge to erode due to gravitational scattering by the more and more massive planet. The combination of the two effects, i.e. large perturber mass and large perturber eccentricity, leads us to expect the resonance structures to be eventually destroyed. Our initial planetary orbital eccentricity is set at 0.1 and is increased by increments of 0.05. The mass is increased by increments of  $1.0 M_J$  starting with a one Jupiter-mass planet, until the first and second order resonance gaps can no longer be observed. It must be noted that our earlier work (i.e. *Paper I*) shows that MMR gaps can theoretically be opened by much less massive planets of the order of one Earth-mass, though these gaps would be very narrow. Thus we chose to focus on planets with  $M > 1.0 M_J$  in this study since they would be relatively more likely to be revealed in high resolution telescopic images of debris disks. The results are discussed in Sections 3.4.1 and 3.4.2 for interior and exterior MMR, respectively.

### 3.4.1 Interior Resonance

If a resonance is caused by the more massive object having a larger orbit than the orbit of the object it is perturbing, it is referred to as “interior resonance”. MMRs caused by Jupiter on the

Asteroid Belt are an example of this type of resonance.

In *Paper I*, we noted that not only is the 2:1 interior MMR with a disk of debris material not azimuthally symmetric about the star, it forms two arc-shaped gaps whose centers are at the planet's inferior conjunction and the other at superior conjunction, both of which orbit the star at the same rate as the planet itself.

Here, we see the same double-arc feature at the 2:1 MMR at higher planet eccentricity values as well (see Figure 3.2(a)). Furthermore, the additional gap at the 3:1 again appears when  $e > 0$  and becomes more prominent as the eccentricity is increased further. This 3:1 MMR gap forms a single arc at the disk's apocenter. Unlike the 2:1 MMR, which travels around the disk at the same rate as the planet, the 3:1 resonance gap remains at the apocenter, regardless of where the planet is along its orbit. This difference can help localize the planet if it does not appear in a telescopic image of a real disk system. Thus the two resonances together provide information on planetary position and orbit geometry.

The appearance of the 3:1 gap at apocenter makes it more visible than it would be if it were at pericenter. The disk is thicker near the forced apocenter and the MMR gaps that are in this part of the disk are wider by a factor of  $1 + e'_f$ . This will not be the case for exterior resonances as will be discussed in Section 3.4.2.

Since the 3:1 gap remains fixed at the disk's apocenter while the 2:1 moves with the planet, for clarity the simulation time is modified slightly so that the planet finishes at apocenter when the simulation ends. An example is shown in Figure 3.2 for MMR with a planet with  $M = 3.0 M_J$  and  $e = 0.1$ . The theoretical locations of the 2:1, 3:2 and 3:1 interior MMR are shown by symbols in Figure 3.2(a) and by dotted lines in Figure 3.2(b) and are calculated using Equation 3.1. The dashed lines on the histograms show the theoretical width of each gap found by the equations for  $\delta a'_{max}$ .

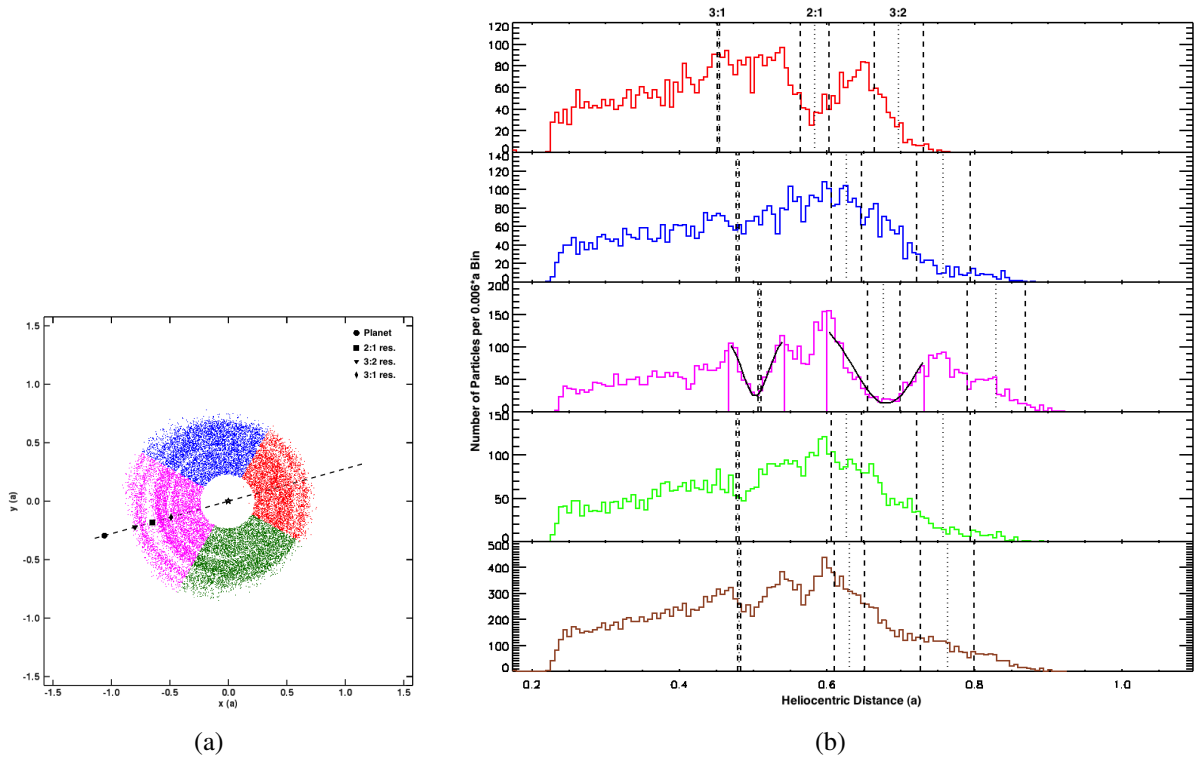


Figure 3.2: Simulation result illustrating interior MMRs with a single planet of mass  $M = 3.0 M_J$  and eccentricity  $e = 0.1$ . (a) Interior 2:1 resonance with a single planet (the filled circle) forms two arc-shaped gaps in the disk whose centers trace the planet as it orbits the star while the 3:1 MMR gap appears as a single arc of less width and is fixed at the disk's apocenter. The dashed line is the planet's line of apses. Note the alignment of the disk's line of apses with the planet's. The symbols represent the theoretical (or nominal) locations for the 2:1, 3:2, and 3:1 MMRs. (b) Distribution of disk particles in heliocentric distance. Colors in the top four panels correspond to segments of the same color in Figure 3.2(a) while the last panel represents the overall distribution of the disk particles from the four segments put together. The dotted lines are the nominal locations of each gap at the 2:1, 3:2 and 3:1 interior resonance with the planet found through Equation 3.1 while the dashed lines show the width of each gap calculated analytically. For consistency, we chose the same bin size we did in *Paper I* which is  $0.006 a$ , where  $a$  is, again, the planet's semimajor axis. Gaussian fits are made to both gaps in the middle histogram which corresponds to the region close to the planet's (and hence the disk's) apocenter.

As noted earlier, the presence of MMR gaps does not necessarily mean that the particles have been ejected from their orbits or destroyed by collision with the star or a planet. They are often caused by an increase in the particles' orbital eccentricities which shifts them away from the heliocentric distance in question. Whether a particle gets physically removed by resonant interaction with a planet or stays bound to the system but increases its eccentricity can be examined by plotting particle distributions in semimajor axis. This is shown by Figure 3.3 which is the same as the bottom panel of Figure 3.2(b) but plotted in semimajor axis instead of heliocentric distance. Note that in our simulations, particles are removed both when they go into a hyperbolic orbit *or* when they go beyond  $0.05 AU < r'_p < 1000 AU$ , where  $r'_p$  is the particle-star distance. So the gaps seen in Figure 3.2(b) are of particles being both shifted in their orbits as well as removed outright. Plotting particle distribution in semimajor axis reveals a few other MMR gaps in addition to the ones that we study here. In fact, the Solar System's Kirkwood gaps only appear when asteroid distribution is plotted in semimajor axis. This is because gaps can be smeared out due to particle eccentricities which can bring them in and out of the gaps (see Figure 1 in Tabeshian & Wiegert (2016) for a plot of Main Belt asteroid distribution in heliocentric distance). However, here we argue that this may not necessarily be the case for all debris disks and a telescopic image of these disks may reveal MMR gaps.

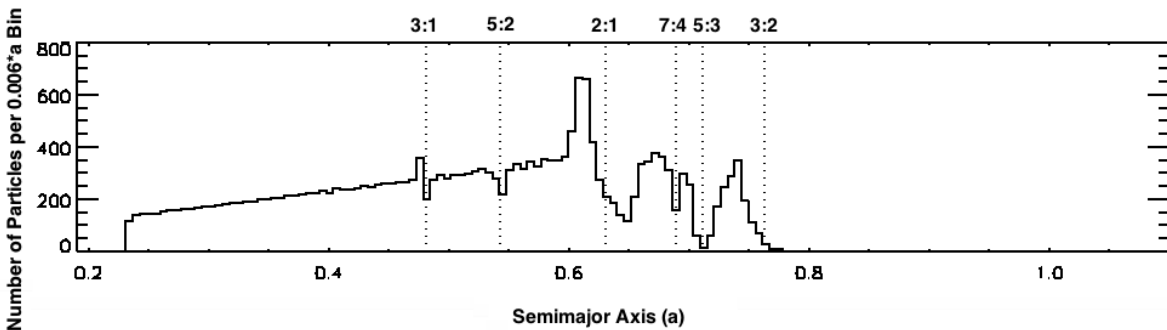


Figure 3.3: Distribution of particles shown by Figure 3.2 but in semimajor axis instead of heliocentric distance. The vertical dotted lines show the nominal resonance locations of the gaps. We note the appearance of additional gaps in this figure at 5:2, 7:4, 5:3 MMR with the planet that are not revealed when particles are plotted in heliocentric distance. We also note a pile-up of particles inward of the 2:1 gap but we have not explored how to disentangle particles near MMRs being removed vs shifting their positions, though both result in gap formation in the disk.

Increasing the planet’s eccentricity eventually erodes the disk, and destroys the 2:1 arc there. This is illustrated by Figure 3.4 for MMR with a planet with  $M = 1.0 M_J$  and  $e = 0.3$ .

In some cases, particles persist outside the main disk, ahead of and behind the planet, as seen in Figure 3.4. These are analogous to the Hilda asteroids in the Solar System’s Main Asteroid Belt which are trapped in 3:2 MMR with Jupiter and form a triangular shaped pattern with their apexes fixed relative to Jupiter. We see this in our simulations of low mass planets with moderate orbital eccentricities.

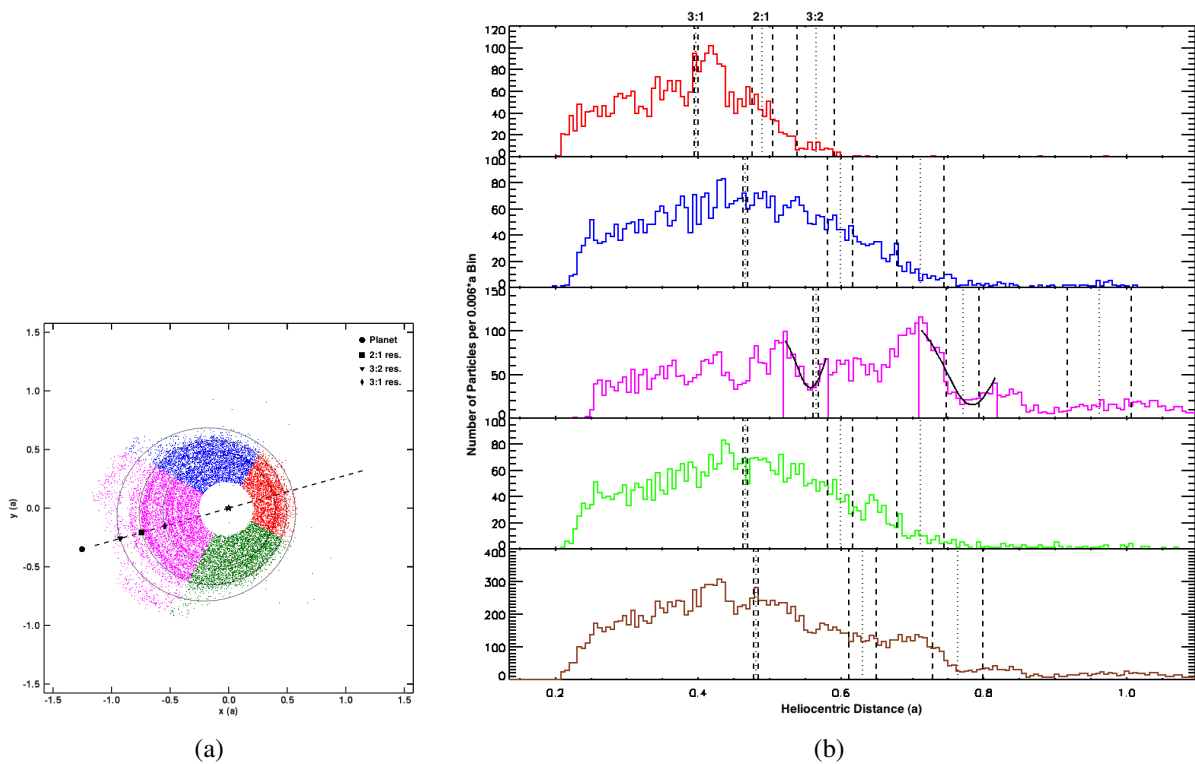


Figure 3.4: Interior resonance gaps formed by interaction of planetesimals with a planet of mass  $M = 1.0 M_J$  and  $e = 0.3$ . (a) Ellipses are drawn on the disk to show the theoretical locations of resonances in all segments. Note that the 2:1 MMR gap is almost at the edge of the disk in the red region (pericenter) while the same gap is more evident in the region near apocenter (magenta). There is particle trapping at 3:2 MMR with the planet. (b) Histograms showing particle distribution for each segment marked with the same color as in Figure 3.4(a).

While increasing planet eccentricity makes the disk narrower at the disk’s pericenter, increasing its mass erodes the disk on both sides (i.e. near apocenter and pericenter) as seen in Figure 3.5 where  $M = 6.0 M_J$  and  $e = 0.1$ .



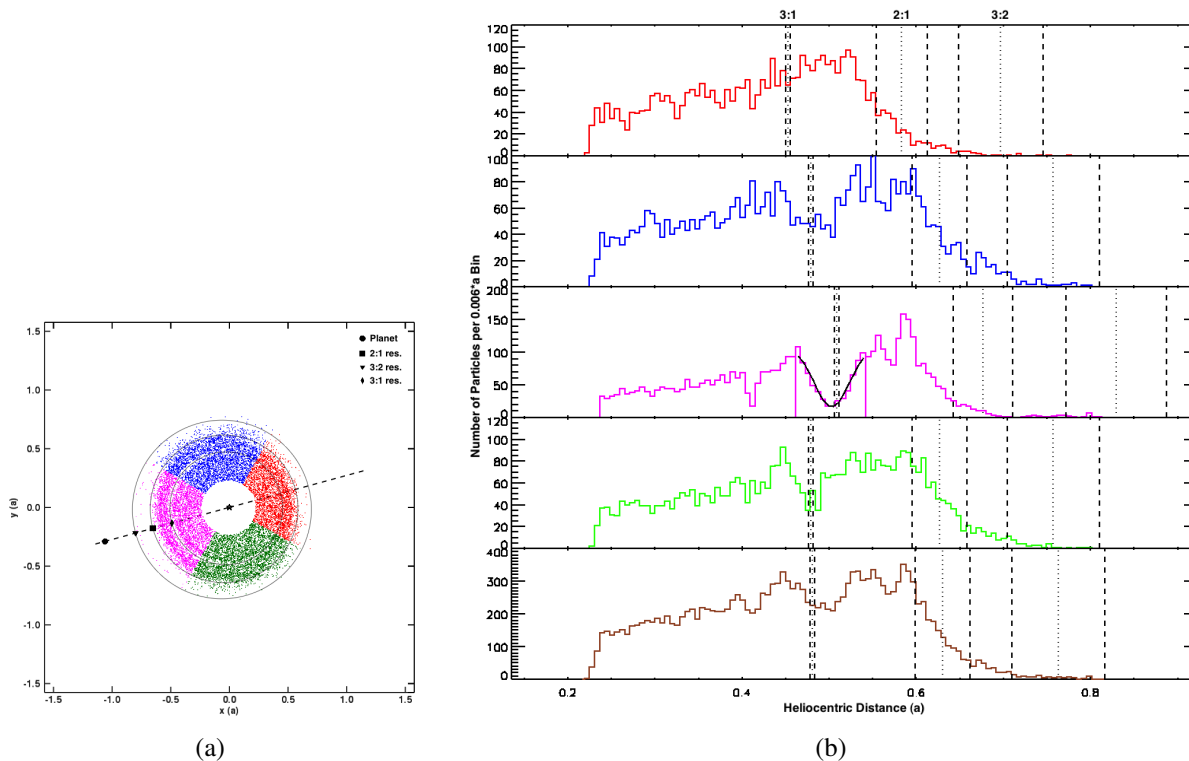


Figure 3.5: Same as Figure 3.4 but with  $M = 6.0 M_J$  and  $e = 0.1$ . Note that the 2:1 gap is destroyed on both sides of the disk. This happens when the perturber’s eccentricity is low, but its mass, and hence its Hill radius, is increased. The most prominent gap in this case is the 3:1, though the 4:1 also now becomes distinguishable (see Section 3.5.2 and Figure 3.7 for a discussion on higher order resonances).

### 3.4.2 Exterior Resonance

An exterior resonance occurs when the more massive object perturbs the orbit of an object exterior to its orbit. One key result in *Paper I* was that, whereas the 2:1 interior MMR forms two-arc shaped gaps, the gap formed at the 2:1 exterior resonance with a planet is a single arc at the perturber’s opposition. This difference allows one to distinguish interior from exterior resonance even if the planet that is causing them remains unseen.

In *Paper I*, increasing the orbital eccentricity of the planet to  $\sim 0.05$  resulted in the 2:1 exterior gap to be extended azimuthally, while at the same time a second gap appeared at a location corresponding to the 3:1 exterior resonance with the planet. Furthermore, for low orbital eccentricities, we observed what seemed to be a series of tightly-wound spiral waves

originating from the 3:1 MMR which we interpreted as forced eccentricity waves due to Lindblad resonances, similar to what is seen in Saturn’s rings. Here we report these waves become weaker and eventually disappear when the planet’s orbital eccentricity is increased beyond 0.2 or when  $m > 2.0 M_J$ .

The gap at the 3:1 exterior MMR also becomes wider as the planet eccentricity is increased, more so if the mass of the planet is increased along with its eccentricity. The behavior of this gap is similar to that in 3:1 interior MMR in that neither of them move around the disk in the inertial frame. However, whereas the latter is found to be fixed at the disk’s apocenter, exterior MMR gap at the 3:1 is fixed at the disk’s pericenter. Resonance structures formed at the 2:1 and 3:1 exterior resonances are shown in Figure 3.6.

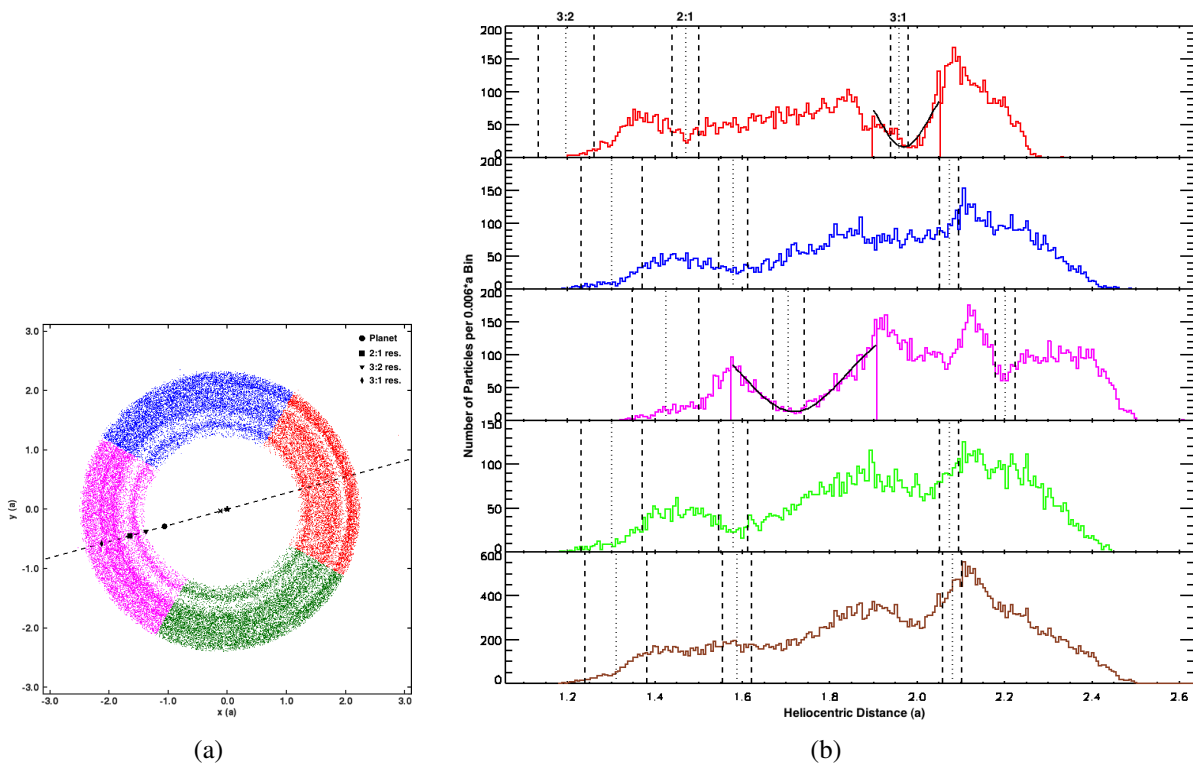


Figure 3.6: Same as Figure 3.2 with mass  $M = 3.0 M_J$  and eccentricity  $e = 0.1$  but with the perturber interior to the disk. (a) Exterior gap at the 2:1 MMR with a single planet forms a single arc in the part of the disk closest to the planet while its center tracks the planet. The 3:1 MMR also appears as a single arc but has a smaller width and is fixed at the disk’s pericenter. The cross shows the geometric center of the disk, taken to be midway between the inner edges of the disk along the major axis. (b) Particle distribution for each segment of the same color as in Figure 3.6(a) along with Gaussian fits to the two gaps.

## 3.5 Discussion

The main results of this work are twofold. First, if a planet is observed near a debris disk, the planet's semimajor axis, orbital eccentricity and mass can in principle be determined from its resonant features within the disk. Second, the presence of unseen planets can be inferred from resonant structures within the disk, but more importantly, 1) the planet's position can be narrowed down for more efficient targeted searches and 2) the planet's properties can still be determined, almost as easily as if the planet itself had been detected. Because it is typically easier to detect the debris disk structures than the planet itself, and since the planet does not need to be detected for these measurements to be made, we discuss below an algorithm for the determination of the properties of the planet on the assumption that the resonant structures have been observed at a single epoch, but the planet itself is unseen. Where relevant, shortcuts available when multi-epoch observations are available will be outlined.

First, we discuss in sections 3.5.1 and 3.5.2 how the appearance and shape of these gaps alone can reveal some information about an unseen planet.

### 3.5.1 Locating an Unseen Planet from Asymmetries in MMR Gaps

The azimuthal asymmetry as well as the difference in the physical appearance of MMR gaps for interior and exterior resonances can be used to not only distinguish resonance gaps from those formed by the dynamical clearing of a planet's orbit, but also to determine which side of the disk the perturber lies if it is unseen.

Gaps cleared out by planets sweeping up their surroundings are azimuthally symmetric and have been observed in both protoplanetary disks (e.g. HL Tau, see for instance, ALMA Partnership et al., 2015) as well as in debris disks (e.g. Epsilon Eridani, see Backman et al., 2009). It must be noted, however, that gaps that are formed by dynamical clearing of planets in their surroundings can become asymmetric if there is a substantial number of particles trapped in the planet's 1:1 MMR, such as the so-called Trojan asteroids. This could make it more

challenging to distinguish a MMR gap from that formed in the feeding zone of a planet, unless there are additional resonance gaps in the disk in which case the relative locations of the gaps may be used to identify them (see below).

Based on our simulations, MMR gaps do not show azimuthal symmetry. As described in Sections 3.4.1 and 3.4.2, the 2:1 gap forms two arcs whose centers are at the planet's inferior and superior conjunctions when the planet is placed exterior to the disk (i.e. when  $a > a'$ ) while forming a single arc with its center at the planet's opposition when the perturber is interior to the disk (i.e. when  $a < a'$ ). The different shapes of resonant structures can be understood through geometrical arguments and are discussed in Chapter 8 of Murray & Dermott (1999). Nevertheless, the two distinctive gap shapes observed in our simulations for interior and exterior resonances suggest that even if the planet's location is unknown, the appearance of either of these gaps can be used to direct targeted searches to locate the planet.

Moreover, if there is an additional arc-shaped gap in the disk, it is likely to be the 3:1 resonance structure if the following three conditions are met: (1) if one gap is narrower than the other, (2) if the narrower gap is interior to the double-arc gap and the ratio of their locations is approximately  $(\frac{3}{2})^{-2/3} = 0.8$  or if it is exterior to the wider single arc gap with the ratio of their locations being about  $(\frac{3}{2})^{2/3} = 1.3$ , and (3) if the narrower gap is fixed at either the apocenter or the pericenter of the disk while the other gap orbits the star. The last condition requires multi-epoch observation of the disk; nevertheless, even if the disk is only observed once, we can still distinguish the 2:1 from the 3:1 gap based on the other two conditions.

### 3.5.2 Higher Order Resonances

As the planet's eccentricity is increased, the 2:1 gap disperses first as the disk around it is scattered by the planet, followed by the destruction of the 3:1 gap as well if the planet's eccentricity is increased further. Nevertheless, though the 2:1 and 3:1 MMR gaps get eroded as the orbital eccentricity of the planet is increased, higher order resonances start appearing in the disk even before the other two gaps disappear, particularly at higher planet masses. This is shown by

Figure 3.7 where the mass and eccentricity of the planet are  $6 M_J$  and 0.2, respectively. The extra gap seen in this figure is at 4:1 interior resonance with the planet. This gap already appears at lower planet mass-eccentricity combinations such as when  $M = 3.0 M_J$  and  $e = 0.1$  or  $M = 1.0 M_J$  and  $e = 0.15$  and becomes more prominent as the two parameters are increased.

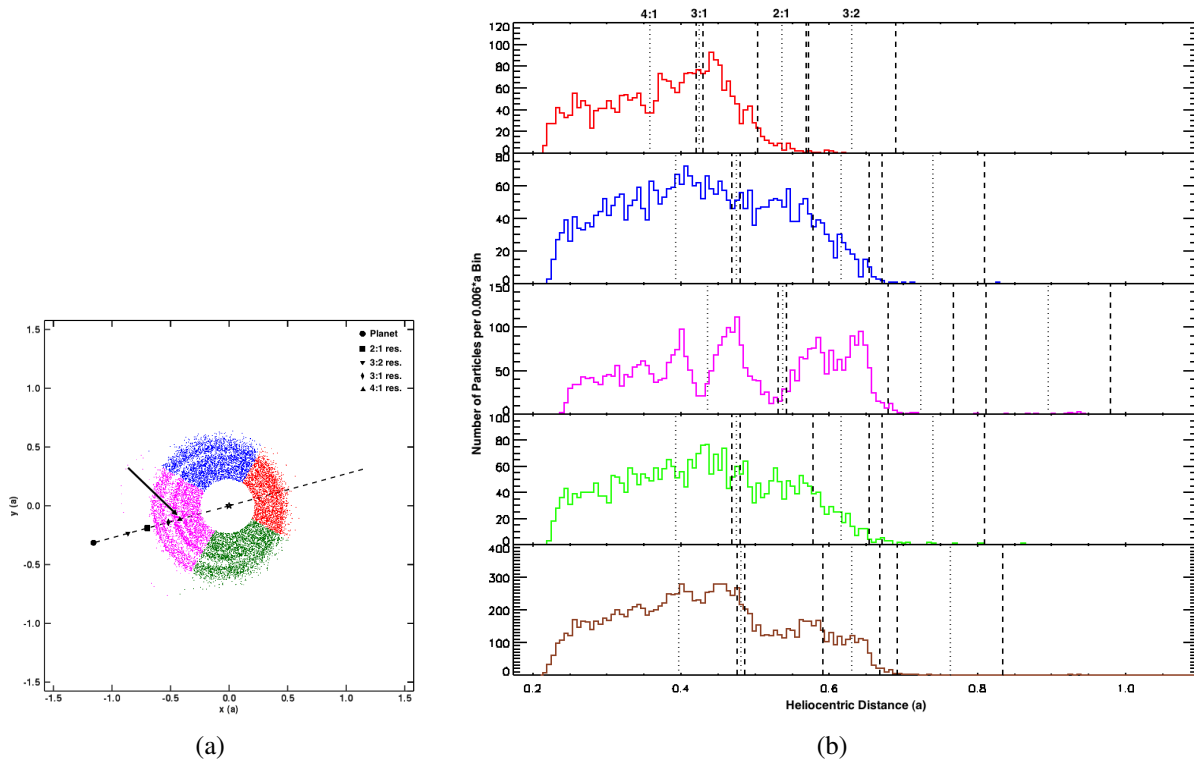


Figure 3.7: Interior MMR with a planet of mass  $6 M_J$  and eccentricity 0.2. (a) Increasing the perturber eccentricity results in formation of an additional gap, corresponding to the 4:1 interior MMR and shown with an upright triangle and an arrow pointing to it, which becomes wider as the perturber’s mass is increased along with its eccentricity. (b) Theoretical location of the 4:1 gap is also overplotted on the histograms.

### 3.5.3 Determining Planetary Parameters

In this section, we discuss how MMR gaps can be used to obtain the perturbing planet’s orbital eccentricity, semimajor axis and hence its orbital period, as well as its mass. Thus observers can detect and characterize extrasolar planets based on their resonant effects on debris disks even if the planets themselves are yet to be detected directly or through other methods.

### **Eccentricity**

In order to determine the orbital eccentricity,  $e$ , of a planet that perturbs a debris disk, an ellipse should be fitted to the gap in order to calculate its eccentricity. The gap eccentricity is equal to the forced eccentricity,  $e'_f$ , induced by the planet; so we can then use Equation 3.3 to calculate the eccentricity of the perturber. The advantage of using this equation for the measurement of planet eccentricity based on the eccentricity of a MMR gap is that the semimajor axis of the gap or the planet need not to be known as long as the particular resonance gap can be identified. This is due to the fact that Equation 3.3 only requires the *ratio* of the two semimajor axes, which can be found from  $p$  and  $q$  through Equation 3.1, without the need for individual parameters to be first determined. If both the 2:1 and the 3:1 gaps are observed, this may be established with confidence. If not, then a single gap is most likely the 2:1, the most prominent unless the disk is heavily eroded due to large planet mass and/or eccentricity as discussed in Section 3.5.2.

### **Semimajor Axis**

Calculating the semimajor axis,  $a$ , of an unseen planet from a single epoch observation of MMR gaps requires the distance to a debris disk to be known; we will assume this is at least approximately known here. Again, the MMR gap must be identified and the  $p$  and  $q$  should be known. The angular separation between a gap seen in the disk to the star can be used to determine the gap distance from the star,  $r'$ . If the disk has non-zero eccentricity, its center of symmetry is offset from the star away from the disk's pericenter. Using the equation for an ellipse in polar coordinates, shown by Equation 3.12 below, one can determine the semimajor axis of the gap's center,  $a'$ :

$$r' = \frac{a'(1 - e_f'^2)}{1 + e_f' \cos(\nu')} , \quad (3.12)$$

where  $e'_f$  is the forced eccentricity of the gap found as described earlier. Again,  $\nu'$  is the true

anomaly of the gap's center, and corresponds to the angle from pericenter to the gap. If no offset is observed, then  $a'$  is simply equal (or close to)  $r'$ . In either case, once  $a'$  is determined, Equation 3.1 can be used to calculate the planet's semimajor axis,  $a$ , provided that we can determine which MMR gap is observed in the disk based on its shape and/or location.

### **Semimajor Axis from Multi-epoch Observations**

As mentioned previously in Section 3.4, we find that the 2:1 gap orbits the star at the same rate as the planet. Wyatt (2003) also finds patterns formed by resonant trapping of particles to co-orbit with the planet, much like the pattern formed by the Hilda asteroids which appears fixed with respect to Jupiter. Though the particles themselves are on Keplerian orbits and orbit at a rate that depends on their semimajor axis, the pattern formed by their resonant trapping goes around the star at the same rate as does the planet. The same is true for patterns formed by resonant gaps at the first order interior or exterior 2:1 resonance. This means that if multi-epoch observations of the disk are available, the orbital period of the planet, and hence its semimajor axis, can be determined by measuring the rate at which the gap moves around the disk. Of course, if the planet itself can be seen in multi-epoch observations, the orbital period is trivial to compute.

Multi-epoch ALMA observations of debris disks should soon be available. For instance, a Jupiter-mass planet at 40 AU orbiting interior to the outer belt of the Epsilon Eridani system, as proposed by Quillen & Thorndike (2002), could form a gap at the 2:1 MMR,  $19''$  from the star, considering the distance to Epsilon Eridani which is 3.22 pc. If the gap co-orbits with the planet around the  $0.82 M_{\odot}$  star, its orbital period would be about 280 years which corresponds to a motion of  $0.''42 \text{ yr}^{-1}$ . This means that the gap's orbital motion could be detectable in high-resolution observations within a few years. The advantage of finding the semimajor axis of the planet from its orbital period is that it eliminates the need to know the distance to the system being studied. Once the semimajor axis of the planet is known, the semimajor axis of the gap can be calculated directly from Equation 3.1 without the need to find  $r'$  first, provided

that  $p$  and  $q$  are known.

### Mass

More massive planets carve out wider resonance gaps in the disk. The change in gap width with planet mass is plotted in Figure 3.8 for interior resonance and in Figure 3.9 for exterior resonance. The triangles show libration widths calculated analytically while the filled squares are found by fitting Gaussians to the gaps as explained in Section 3.4. The solid and the dashed lines are our linear fits to the calculated and measured values, respectively; the different colors are for different planet eccentricities.

Our results show an increasing trend in gap width with increasing planet mass and eccentricity, as the theoretical calculation of the resonance width also suggests. Therefore, we propose a set of equations that allow the mass of the perturbing planet to be calculated for the different perturber eccentricities without the need to directly detect the planet or infer its mass through other means if (a) we can determine which MMR gap we observe in the disk and (b) a measure of the MMR gap width and eccentricity can be obtained observationally. The relation between a MMR gap width and the perturber's mass when a range of moderate planet eccentricity values are used is shown by the equations in Table 3.1 for the 2:1 and 3:1 interior as well as exterior MMRs. These are drawn from least-square fits to the values we obtain by Gaussian fitting to the simulation histograms where the gaps appear, as discussed in Section 3.4. In these equations,  $M$  is the planet mass (in Jupiter masses,  $M_J$ ) and  $W_o$  is the observed MMR gap width (in units of the distance between the star and the observed gap,  $r'_o$ ).



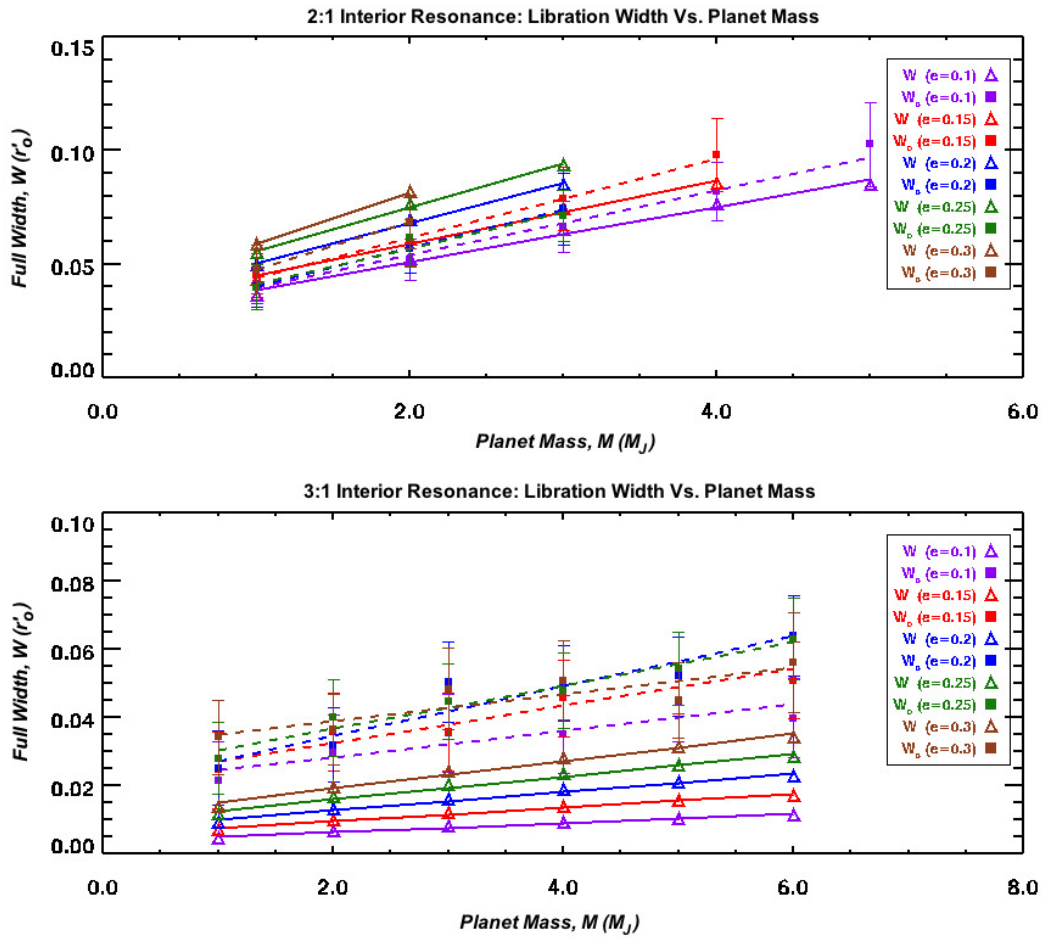


Figure 3.8: Change in MMR libration width with planet mass for 2:1 (top) and 3:1 (bottom) resonance with a planet exterior to the disk (i.e. interior resonance). Different colors represent different planet eccentricities used in the simulations while the solid and the dashed lines are least-square fits to measurements obtained analytically (shown by triangles) and by Gaussian fitting to gaps in particle distribution (shown by filled squares), respectively.

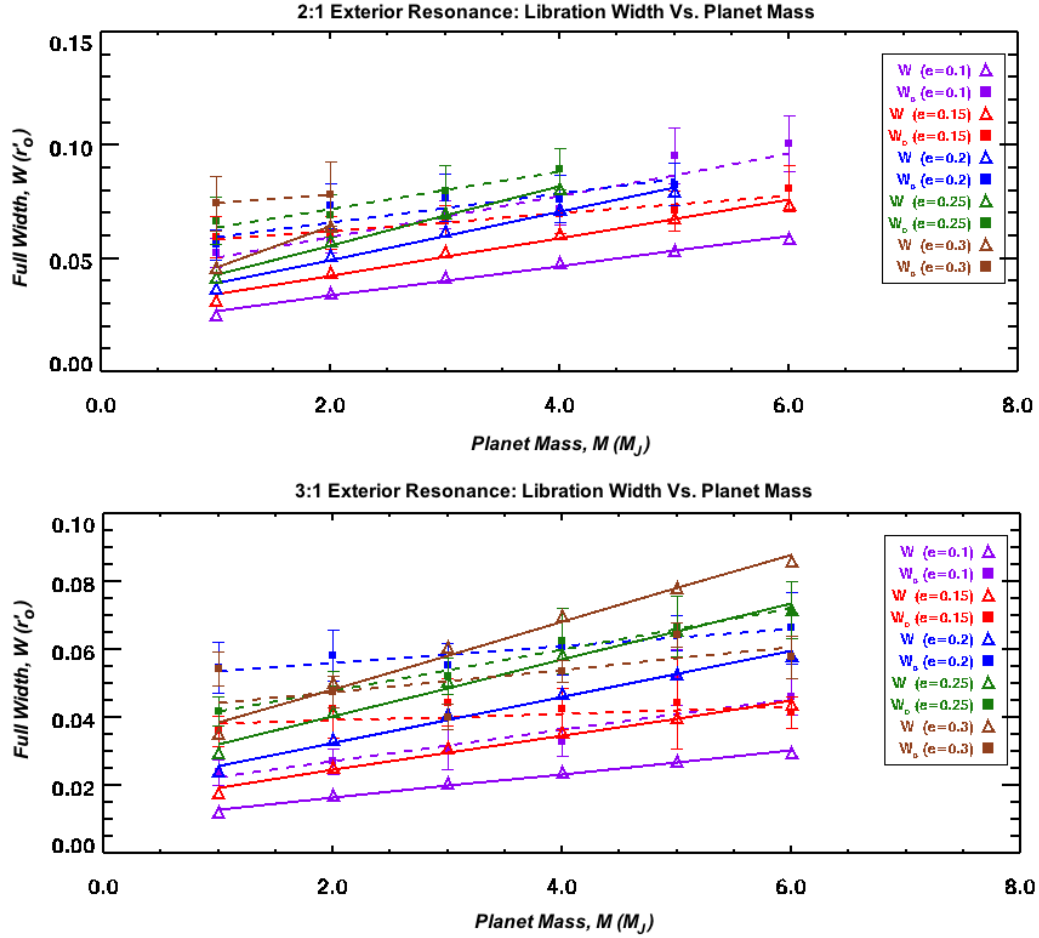


Figure 3.9: Same as Figure 3.8 but for exterior resonance.

Table 3.1: Equations relating the mass of a perturber,  $M$  in  $M_J$ , having various orbital eccentricities to the observed width of a gap,  $W_o$  in  $r'_o$  (the observed gap location), at the 2:1 and 3:1 interior and exterior MMR drawn from our measurements of gap widths.

e	Interior Resonance		Exterior Resonance	
	2:1	3:1	2:1	3:1
0.1	$M = \frac{1}{0.014}(W_o - 0.025)$	$M = \frac{1}{0.004}(W_o - 0.021)$	$M = \frac{1}{0.009}(W_o - 0.041)$	$M = \frac{1}{0.005}(W_o - 0.018)$
0.15	$= \frac{1}{0.018}(W_o - 0.026)$	$= \frac{1}{0.005}(W_o - 0.022)$	$= \frac{1}{0.004}(W_o - 0.054)$	$= \frac{1}{0.001}(W_o - 0.037)$
0.2	$= \frac{1}{0.017}(W_o - 0.023)$	$= \frac{1}{0.007}(W_o - 0.020)$	$= \frac{1}{0.006}(W_o - 0.053)$	$= \frac{1}{0.003}(W_o - 0.051)$
0.25	$= \frac{1}{0.016}(W_o - 0.025)$	$= \frac{1}{0.006}(W_o - 0.024)$	$= \frac{1}{0.008}(W_o - 0.056)$	$= \frac{1}{0.006}(W_o - 0.036)$
0.3	$= \frac{1}{0.021}(W_o - 0.027)$	$= \frac{1}{0.004}(W_o - 0.031)$	$= \frac{1}{0.004}(W_o - 0.070)$	$= \frac{1}{0.003}(W_o - 0.041)$

Our measurements of gap widths for structures formed at the 2:1 interior MMR with a single planetary perturber are within 25% of theoretical values. The difference is larger when the analysis is done on the 3:1 interior resonance gap as there seems to be a systematic offset between the calculated and the measured values for the gap width. We attribute the difference between the measured and the calculated widths to the fact that the equations to calculate  $\delta a'_{max}$  presented in Murray & Dermott (1999) are only first order approximations when eccentricities are greater than zero. Furthermore, in *Paper I* we saw spiral patterns forming in the disk when the planet was placed interior to the disk (i.e. exterior resonance) which we believed were due to Lindblad resonances generating from the 3:1 MMR. This makes defining the edges of the gaps more difficult in this case and may be the reason why our results for the exterior resonance case shown in Figure 3.9 have an inconsistency in slope with the theoretical values, more so than in the interior resonance case. Nevertheless, we propose that the set of equations presented in this study (Table 3.1) can be used to estimate the mass of the planetary perturber to within 1  $M_J$ .

### 3.5.4 Disk Offset and Peri/Apocenter Glow

As the planet eccentricity increases, so does the forced eccentricity of the disk, causing a net offset in the overall particle distribution away from the central star. This offset is away from the direction of the forced pericenter of the disk particle orbits, confirming the findings by Wyatt et al. (1999) discussed earlier in Section 3.2.2 that a physical disk offset toward apocenter is to be expected if there is a perturbing body with non-zero orbital eccentricity. Therefore, we also find that the presence of a disk offset may be evidence for a planetary (or a stellar) companion on an eccentric orbit.

Furthermore, we investigate the wavelength dependence of the apo/peri-center brightness variations, the “pericenter (or apocenter) glow”. To do so, we bin particles in  $x$  and  $y$  and assign a flux to each bin, assuming that the particles emit as perfect blackbodies. The pixel values on opposing sides of the disk are then added and compared. We note that the peri-

versus apocenter glow depends on the wavelength of observation, as was found by Pan et al. (2016). The magnitude of the effect depends on the disk and star parameters. While a thorough study of this phenomenon is outside the scope of this paper, particularly since we have not included sub-micron dust in our simulations, we note that the peri/apo difference can easily reach several percent. For instance, a Jupiter-mass planet with  $e = 0.3$  placed 1 AU away from a debris disk orbiting a solar-mass star would result in 8% more flux from the apocenter side of the disk when observed at  $1300 \mu\text{m}$ . However, when the same disk is observed at  $10 \mu\text{m}$ , we find a pericenter glow of 10%. Here we note again that resonant structures may not be visible in the observed disks if studied at sub-micron wavelengths due to the gaps being washed out by sub- $\mu\text{m}$  size dust as it migrates outward in the disk by stellar radiation pressure (Kuchner & Stark, 2010).

### 3.5.5 Simulating ALMA Observations

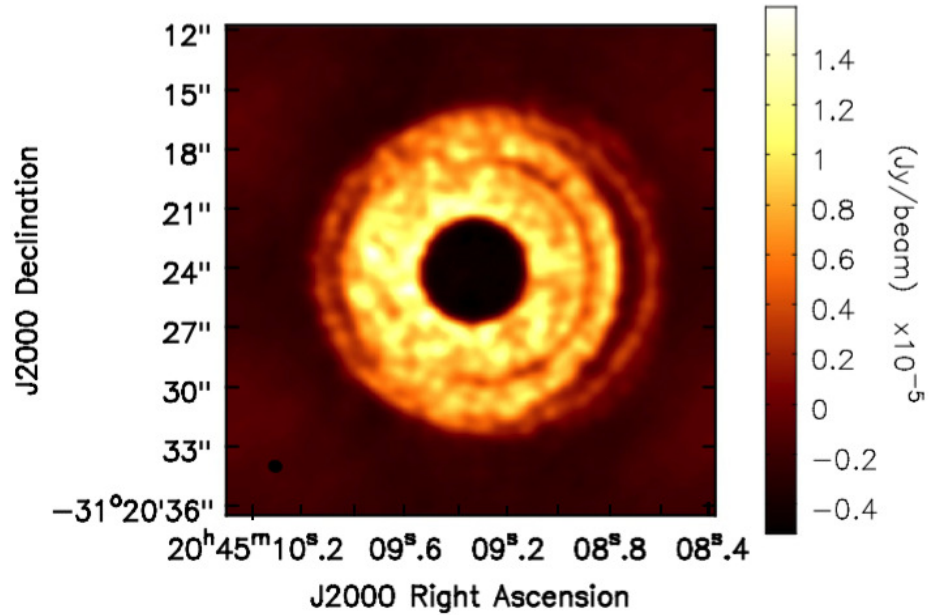
Whereas MMR gaps are clearly visible in our simulated disks, whether or not they can be detected in a telescopic image of a debris disk depends largely on current observing capabilities. The technology is reaching the point at which we should start seeing a variety of structures including the resonance gaps discussed in this paper as ALMA images of second generation disks emerge. Therefore, we discuss here the observability of MMR gaps as seen by powerful interferometers such as ALMA. For this purpose, we use the Common Astronomy Software Applications (CASA) offered by the National Radio Astronomy Observatory (NRAO) to simulate ALMA observations (McMullin et al., 2007).

We use as our fiducial example the *AU Microscopii* debris disk, which has already been well studied with ALMA (MacGregor et al., 2013). Synthetic images of our simulated disks are created, on the assumption that they are the same size (140 AU radius), distance (9.91 pc) and overall brightness (7.14 mJy) as the one around AU Mic. AU Mic is a  $\sim 10$  Myr-old M-type star with  $R = 0.83 R_{\odot}$  and  $T = 3600 \text{ K}$  (Matthews et al., 2015) that has an edge-on debris disk first discovered by Kalas et al. (2004).

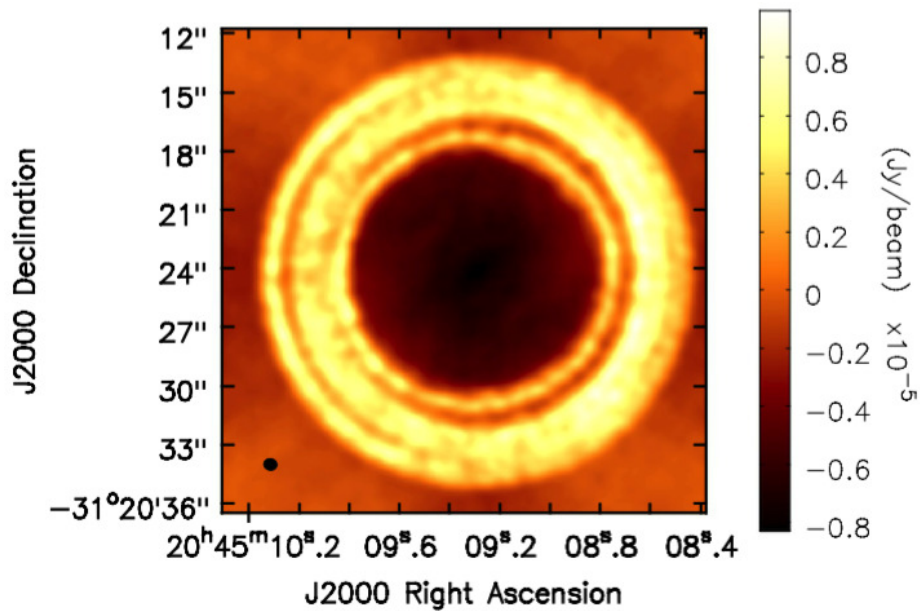
Our simulated disk is taken to be optically thin and composed of perfect blackbodies emitting at the local equilibrium temperature. We then use CASA to determine how our simulated disks would appear if observed with the same resolution used to image the AU Mic disk with ALMA at 230 GHz or 1.3 mm (see MacGregor et al., 2013) if they were to be viewed face-on. This would correspond to a resolution of  $0.6''$  or about 6 AU.

When ALMA was used for the first time to observe the debris disk around AU Mic in 2012, there were only 20 operational 12 m antennas. However, we utilize all 50 antennas available in the 12 m array to make our simulated images to achieve the desired resolution. Furthermore, we set the integration time to 10 s per pointing and assume that the disk is observed for a total of 4 hours. The RA and Dec of the source are also taken from MacGregor et al. (2013) to be  $\alpha = 20^h45^m09^s.34$  and  $\delta = -31^\circ20'24''.09$ , J2000. Figure 3.10 illustrates an example of two beam-deconvolved images that we made with CASA where the top and bottom figures show the same disks as in Figures 3.2(a) and 3.6(a), respectively. In both examples, the MMR structures in the simulated disks are easily visible.

In order to assess the observability of the structures in our simulated disks, we calculated the edge-to-center contrast for each gap and noted that for the 2:1 and the 3:1 gaps in our simulated images, the contrast is about 60% and 30%, respectively (see Figure 3.11). This means that both the 2:1 and 3:1 gaps in Figures 3.10(a) and 3.10(b) would produce high contrast and should be visible by ALMA. Therefore, we argue that given the high sensitivity and resolving power that can be achieved with ALMA, the structures discussed in this paper are, in fact, within current detectability limits.



(a)



(b)

Figure 3.10: Using the CASA simulator, this is how the disks in Figures 3.2(a) (top) and 3.6(a) (bottom) would look like after beam deconvolution if they were placed at the AU Mic distance and observed with the same resolution used in observing its debris disk ( $0.''6$ ). The arcs seen in these images correspond to gaps formed at the 2:1 and 3:1 interior (top) and exterior (bottom) MMR with a planet. Although the 2:1 gap has a better contrast compared to the 3:1 in both simulated images, both gaps would be visible. The color bar shows the flux in (Jy per beam)  $\times 10^{-5}$ . The synthesized beam is shown by a black ellipse in the lower left corner and is  $0.''68 \times 0.''60$ .

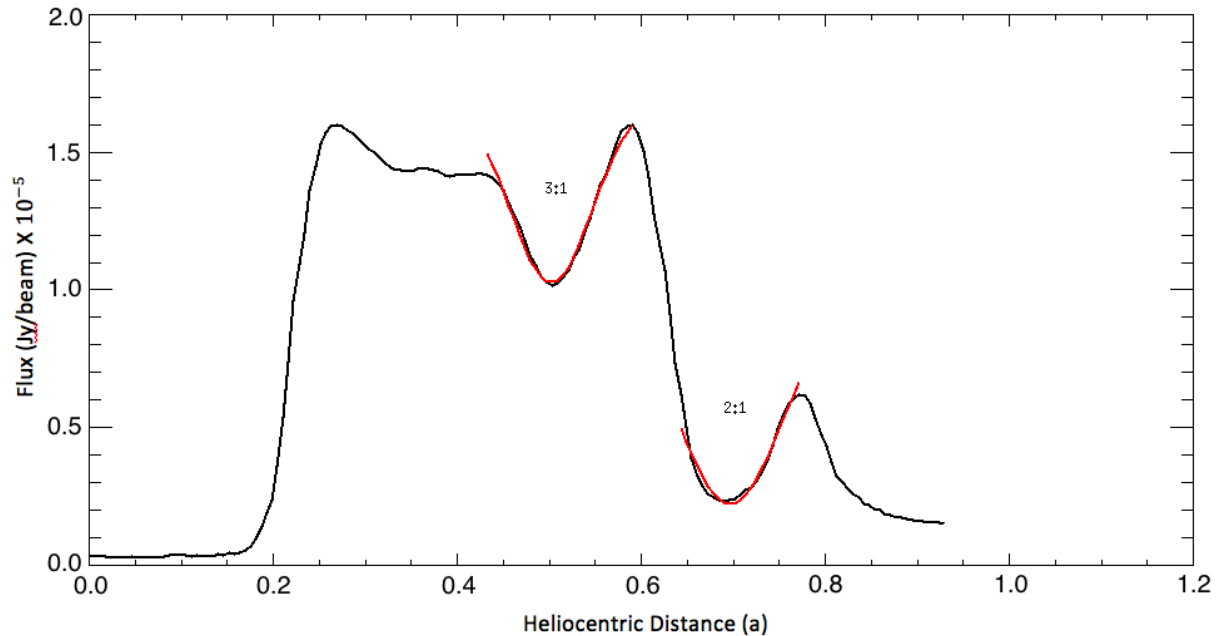


Figure 3.11: Surface brightness profile of the disk shown in Figure 3.10(a) along the major axis. A Gaussian function is used to fit each gap to measure its depth. The gap edge-to-center contrast is 60% for the 2:1 gap and 30% for the 3:1, indicating that both gaps are deep enough to be detectable.

### 3.6 Summary and Conclusions

We extended our study of gaps formed through resonant interactions of a single planet with a gas-poor dynamically cold debris disk, presented in an earlier paper (Tabeshian & Wiegert, 2016), to include systems in which the planet has moderate orbital eccentricity. Gravitational perturbation of the particles by a planet forms gaps whose locations correspond to the mean-motion resonances with the planet.

Unlike gaps cleared by planets around their orbits, we found that the MMR gaps, formed away from the orbits of the planets, are not azimuthally symmetric about the star. For the 2:1 MMR, a planet orbiting exterior to the disk leaves its resonance imprint as two arc-shaped gaps at inferior and superior conjunctions, but forms a single arc at opposition if placed interior to the disk. This difference allows observers to distinguish between interior and exterior resonances solely based on the shape of the 2:1 gap.

We thus provided a simple procedure for determining the mass, semimajor axis and ec-

centricity of the planetary perturber from single-epoch measurements of a debris disk. If multi-epoch observations are available, the determination becomes easier. Nevertheless, the planetary parameters can be determined from the resonant structures even if the planet itself remains unseen by analyzing the resonance gaps in the following way:

(A) The eccentricity at the center of a MMR gap can be measured by least-square fitting of ellipses to the gap edges (Section 3.5.3).

(B) The distance between a gap and the host star can be determined observationally if the distance to the system being studied is known, which is often the case for nearby debris disks that have been observed. This information together with the eccentricity of the gap as well as the true anomaly of its center can then help calculate the gap's semimajor axis,  $a'$  using Equation 3.12.

(C) If we can determine which resonance gap is observed in the disk, calculating the planet's semimajor axis is trivial and can be done using Equation 3.1. Alternatively, the planet's semimajor axis can be found if its orbital motion is detected in multi-epoch observation of the disk (Section 3.5.3).

(D) Once the semimajor axes of the planet and the gap are found, the eccentricity of the planet can be determined using the forced eccentricity at the center of the gap and Equation 3.3. This is true since in a dynamically cold debris disk, where disk particles can be assumed to have zero or negligible free eccentricities, orbital eccentricity anywhere in the disk is defined by the forced eccentricity induced by the planet at that location.

(E) Finally, since the libration width of a MMR gap is related to the perturber's mass and eccentricity, a measurement of the gap width can help determine the mass of the planet using the formulae that we presented in this work (see Table 3.1 in Section 3.5.3).

In addition to the 2:1 gap, we found that increasing the perturber's eccentricity resulted in formation of a second gap at the 3:1 MMR which forms a single arc. Increasing the perturber's orbital eccentricity also resulted in formation of higher order resonance gaps in the disk. Furthermore, we noted that while the 2:1 gap orbits the star at the same rate as the planet, the 3:1



gap remains stationary in the inertial frame. It appears at apocenter for interior and at pericenter for exterior MMR. This difference can be important if multi-epoch observations of the disk are available.

Furthermore, we independently confirmed the result of Pan et al. (2016) of the wavelength dependence of the apocenter/pericenter glow phenomenon, which is a trade-off between larger number of particles at apocenter and enhanced flux caused by the disk offset away from pericenter in debris disks that are perturbed by a planet with non-zero orbital eccentricity.

By means of the CASA simulator, we showed that resonance structures should be detectable in images of suitable debris disks using ALMA or other high resolution facilities. We conclude that the analysis of MMR gaps in extrasolar debris disks is a useful indirect technique to not only detect, but also characterize extrasolar planets.

# Bibliography

ALMA Partnership, Brogan C. L., Pérez L. M., et al., 2015, ApJL, 808, L3.

Augereau, J. C., Nelson, R. P., Lagrange, A. M., et al., A&A, 370, 447.

Aumann, H. H., Beichman, C. A., Gillett, F. C., et al., 1984, ApJ, 278, L23.

Backman, D., Marengo, M., Stapelfeldt, K., et al., 2009, ApJ, 690, 1522.

Burrows, C. J., Krist, J. E., Stapelfeldt, K. R., & WFPC2 Investigation Definition Team., 1995, in BAAS, Vol. 27, , 1329.

Chiang, E., Kite, E., Kalas, P., et al., 2009, ApJ, 693, 734.

Dermott, S. F., Jayaraman, S., Xu, Y. L., et al., 1994, Nature, 369, 719.

Dohnanyi, J. S., 1969, Journal of Geophysical Research (JGR), 74, 2531.

Gold T., 1975, Icarus, 25, 489.

Greaves, J. S., Holland, W. S., Moriarty-Schieven, G., et al., 1998, ApJL, 506, L133.

Hahn, J. M. and Malhotra, R., 1999, AJ, 117, 3041.

Jackson, A. A. and Zook, H. A., 1989, Nature, 337, 629.

Kalas, P., Liu, M. C., and Matthews, B. C., 2004, Science, 303, 1990.

Kalas, P., Graham, J. R., and Clampin, M., 2005, Nature, 435, 1067.

- Kirkwood, D. 1867, *Meteoric Astronomy: A Treatise On Shooting-stars, Fireballs, & Aerolites* (Philadelphia, PA: J. B. Lippincott & Co.).
- Klačka J. and Kocifaj M., 2008, *MNRAS*, 390, 1491.
- Kuchner, M. J. and Stark, C. C., 2010, *AJ*, 140, 1007.
- Lagrange, A. M., Bonnefoy, M., Chauvin, G., et al. 2010, *Science*, 329, 57.
- MacGregor, M. A., Wilner, D. J., Rosenfeld, K. A., et al. 2013, *ApJ*, 762, L21.
- Malhotra R., 1995, *AJ*, 110, 420.
- Matthews, B. C., Kennedy, G., Sibthorpe, B., et al. 2015, *ApJ*, 811, 100.
- McMullin, J. P., Waters, B., Schiebel, D., et al., 2007, in Shaw R. A., Hill F., Bell D. J., eds, *Astronomical Data Analysis Software and Systems XVI Vol. 376 of Astronomical Society of the Pacific Conference Series, CASA Architecture and Applications*. p. 127.
- Mouillet, D., Larwood, J. D., Papaloizou, J. C. B., et al., 1997, *MNRAS*, 292, 896.
- Murray, C. D. and Dermott, S. F., 1999, *Solar System dynamics* (Cambridge: Cambridge Univ. Press).
- Nesvold, E. R. and Kuchner, M. J., 2015, *ApJ*, 798, 83.
- Ozernoy, L. M., Gorkavyi, N. N., Mather, J. C., et al., 2000, *ApJL*, 537, L147.
- Pan, M., Nesvold, E. R., and Kuchner, M. J., 2016, *ApJ*, 832, 81.
- Quillen, A. C. and Thorndike S., 2002, *ApJL*, 578, L149.
- Reche, R., Beust, H., Augereau, J. C., et al., 2008, *A&A*, 480, 551.
- Tabeshian M. and Wiegert P. A., 2016, *ApJ*, 818, 159.
- Telesco, C. M., Fisher, R. S., Piña, R. K., et al., 2000, *ApJ*, 530, 329.

Weidenschilling, S. J. and Jackson, A. A., 1993, *Icarus*, 104, 244.

Wilner, D. J., Holman, M. J., Kuchner, M. J., et al., 2002, *ApJ*, 569, L115.

Winn, J. N. and Fabrycky, D. C., 2015, *ARA&A*, 53, 409.

Wisdom, J. and Holman, M., 1991, *AJ*, 102, 1528.

Wyatt, M. C., Dermott, S. F., Telesco, C. M., et al., 1999, *ApJ*, 527, 918.

Wyatt, M. C., 2003, *ApJ*, 598, 1321.

Wyatt, M. C., 2005, *A&A*, 433, 1007.

Wyatt, M. C., 2008, *ARA&A*, 46, 339.

# Chapter 4

## Detection and Characterization of Extrasolar Planets: Applying a Particle-only Model to the HL Tau Disk

*This chapter is adapted from: Tabeshian, M. & Wiegert, P. A., 2017 (in prep).*

### 4.1 Introduction

Planets are believed to form in protoplanetary disks. While doing so, they create complex symmetric and asymmetric morphological structures. These include density enhancements due to particle trapping in a planet's pressure bumps and mean-motion resonances (MMRs), as well as gap clearing due to dynamical ejection of disk particles as they come into close encounter with the forming planets. In fact, numerical simulations have shown that a planet with only 0.1 Jupiter-mass ( $M_J$ ) is capable of pushing the dust away and significantly changing the dust-to-gas ratio of a protoplanetary disk in its vicinity and hence can clear a gap in dust distribution while a planet mass of at least 1  $M_J$  is needed to also form a gap in gas surface density (see for instance, Paardekooper & Mellema, 2004; Price et al., 2017). Such structures

provide a wealth of information about the planets that are otherwise difficult to directly observe (such as a planet's mass); and many studies have attempted to put constraints on the planetary parameters based on how planets affect the distribution of gas and dust in protoplanetary disks (see for instance, Casassus et al., 2013; van der Marel et al., 2013; Andrews et al., 2011).

Protoplanetary disks are gas-rich and a full exploration of their dynamics by numerical methods is expensive in terms of computing power. Such disks also show many features which are similar to those observed in debris disks - disks of solid particles whose interactions are much easier to model computationally than gas-rich disks. Here we ask the question "How well can the parameters of planets embedded in a protoplanetary disk be extracted using simpler 'particle-only' methods?" Indeed we find that the masses and semimajor axes of the planets that may be sculpting the gaps in the HL Tau disk can be extracted with accuracy comparable to that of full hydrodynamic simulations, assuming that there are 3 hidden planets in the disk. Thus quick particle-only simulations of protoplanetary disks may be a useful tool for preliminary analyses, and provide useful initial starting points for parameter searches with more complete models. It should be noted that planet formation is not the only mechanism that is thought to explain the origin of the gap structures in protoplanetary disks. For instance, in a study by Zhang et al. (2015), volatile condensation and rapid pebble growth beyond the snow line are used to reproduce structures such as those observed in the HL Tau disk. On the other hand, secular gravitational instability is also discussed as one mechanism that could create ring structures in protoplanetary disks (see for instance Takahashi & Inutsuka, 2014). Although these mechanisms may alternatively be used to explain the structures observed in the HL Tau disk, gap opening by planets embedded in this disk remains a strong possibility, and this is what we will consider in the present study. The fact that the eccentricities of the rings increase with increasing distance and that many of the rings are nearly in a chain of mean-motion resonances indicate that the architecture of the HL Tau disk likely arises from embedded planets (see ALMA Partnership et al., 2015).

We begin here with a description of the literature on the topics of HL Tau's embedded

planets in Section 4.1.1, before turning to our own modelling efforts in Section 4.2 where we discuss our simulations to match the observed intensity profile of the HL Tau disk including the fitting procedure as well as uncertainty measurements. We discuss our results in Section 4.3 including a discussion of MMR gaps in the HL Tau disk. Finally, a summary and conclusions are provided in Section 4.4.

### 4.1.1 Hydrodynamic Studies of HL Tau to Date

Recent high resolution observation of a protoplanetary disk around the young ( $\sim 1$  Myr) T-Tauri star HL Tauri by the *Atacama Large Millimeter/submillimeter Array* (ALMA) has revealed unprecedented detailed structures, which are considered to be likely the signatures of planets in the making. This image was taken as part of ALMA's science verification phase in October 2014 and was released a month later (see NRAO (2014)). The disk was observed in dust continuum emission at 233 GHz or 1.28 mm using 25-30 antennas and a maximum baseline of 15.24 km as part of ALMA's Long Baseline Campaign, and achieved an angular resolution of 35 milliarcsecond, equivalent to 5 AU at HL Tau's distance of 130 parsecs. It reveals a series of concentric gaps that have become the subject of many studies, with the hope of shedding light on the properties of the planets that are believed to be carving out these gaps and ultimately gaining a better understanding of the processes involved in the formation and evolution of planets and planetary systems. ALMA Partnership et al. (2015) identify 7 pairs of distinct dark and bright rings in the ALMA image of the HL Tau disk which they label D1...D7 and B1...B7 (more on this in Section 4.4). They approximate the radial distance of the center of each ring by making a cross-cut along the disk's major axis and find the dark rings to be at  $13.2 \pm 0.2$ ,  $32.3 \pm 0.1$ ,  $\sim 42$ ,  $\sim 50$ ,  $64.2 \pm 0.1$ ,  $73.7 \pm 0.1$ , and  $\sim 91.0$  AU, placing the first four dark rings in a chain of mean-motion resonances, specifically 1:4:6:8. Pinte et al. (2016) measure the missing dust mass in each of the 7 gaps by integrating the dust surface density of each gap and comparing it to its surrounding bright rings. These would provide the mass of the rocky cores of their potentially embedded planets (see Table 4.1 for mass measurements of the planets in 5

of the 7 gaps).

Other works have also attempted to constrain the masses of the planets that are believed to be shepherding the HL Tau gaps. Based on the depth of the gap seen  $\sim 30$  AU from the central star in the HL Tau disk, Kanagawa et al. (2015) estimate the mass of its embedded planet to be at least  $0.3 M_J$ , where  $M_J$  denotes Jupiter’s mass. They do so by using the relationship between the depth of a gap formed by a planet in its feeding zone in a protoplanetary disk and the mass of the planet as well as the disk’s viscosity and scale height (Duffell & MacFadyen, 2013; Fung et al., 2015; Kanagawa et al., 2015, see), given by Equation 4.1 (Kanagawa et al., 2015):

$$\frac{M_p}{M_\star} = 5 \times 10^{-4} \left( \frac{1}{\Sigma_p/\Sigma_0 - 1} \right)^{1/2} \left( \frac{h_p}{0.1} \right)^{5/2} \left( \frac{\alpha_{ss}}{10^{-3}} \right)^{1/2}, \quad (4.1)$$

where  $M_p$  is the planet’s mass in stellar mass unit  $M_\star$ ,  $\Sigma_p/\Sigma_0$  is the gap depth which is the ratio of the surface density of the planet-induced gap to that of the unperturbed disk,  $h_p$  is the disk’s aspect ratio at the planet’s orbital radius ( $h/r$ , with  $h$  being the scale height), and  $\alpha_{ss}$  is the Shakura-Sunyaev kinematic viscosity parameter (Shakura & Sunyaev, 1973).

Adopting a stellar mass of  $1 M_\odot$ , a viscosity parameter of  $10^{-3}$ , and estimating the gap depth and the disk’s aspect ratio to be  $\sim 1/3$  and  $\sim 0.07$  respectively, Kanagawa et al. (2015) are able to constrain the mass of the planet at 30 AU to be  $> 0.3 M_J$ .

Using hydrodynamic simulations and radiative transfer models, Jin et al. (2016) attempt to match the width and depth of the three prominent gaps in the HL Tau disk, located at 13.1, 33.0, and 68.6 AU and constrain the masses of the planets that are believed to be in those gaps to be 0.35, 0.17, and  $0.26 M_J$ , respectively, assuming no planet migration through the disk. The model also assumes a disk mass of  $\sim 7.35 \times 10^{-2} M_\odot$  and the same  $\alpha_{ss}$  parameter as Kanagawa et al. (2015) while the dust to gas ratio is taken to be 1%. Furthermore, the authors also try to match the eccentricities of the gaps where they place the three planets and find them to be 0.246, 0.274, and 0.277, respectively. On the other hand, smoothed particle hydrodynamic (SPH) models by Dipierro et al. (2015) constrain the masses of the planets embedded in the HL Tau disk to be 0.2, 0.27 and  $0.55 M_J$  with planets at 13.2, 32.3 and 68.8 AU.



Gas and dust interact differently with the planet. Numerical simulations by Jin et al. (2016) also show that the three gaps formed by tidal interaction with the embedded planets in the HL Tau disk are shallower in gas distribution and deeper in dust, though both have similar morphologies (see their Figure 1). The difference in the gap's gas and dust surface density arises from the fact that submillimeter dust is pushed toward the edges of the gap as it starts to open since gas drag tends to accumulate dust particles in high pressure regions as suggested by the enhanced dust emission near gap edges (see Haghhighipour & Boss, 2003; Maddison et al., 2007; Fouchet et al., 2007).

Most authors place three planets in the HL Tau disk; however, the possibility of additional planets in this disk has also been discussed in the literature. For instance Tamayo et al. (2015) consider the presence of up to 5 planets in the HL Tau disk at nominal radii of 13.6, 33.3, 65.1, 77.3 and 93.0 AU. This places the outer three planets nearly in a chain of 4:3 mean-motion resonance. The authors constrain the masses of the five planets under two different scenarios: If the planets are not in mean-motion resonance, they find a maximum mass of  $\sim 2$  Neptune masses for the outer three bodies. However, if the outer three planets are in resonance, as suggested by the locations of the gaps, they can grow to larger masses via resonant capture as they migrate through the disk during which their masses can reach at least that of Saturn. The masses of the two inner planets are not well constrained in this study since these planets are dynamically decoupled from the other three.

Planets forming in a multi-planet system can grow up to a certain mass beyond which the system becomes unstable simply because of the growth in the sizes of the planets' Hill spheres. The Hill sphere defines the region around a planet where its gravity dominates over that of the star: systems of moons, for example, must reside well within a planet's Hill sphere to be stable. Planets whose orbits around the star are separated by less than several of their mutual Hill spheres are also unstable: this stability criterion is defined by Gladman (1993) who suggests planets that are separated by less than  $3.46 r_H$  destabilize on a timescale that is roughly their conjunction period, where the Hill radius,  $r_H$ , is defined as  $(\frac{M}{3M_*})^{(1/3)} a$ , with

$M$  and  $M_*$  the masses of the planet and the star, respectively, and  $a$  the semimajor axis of the planet's orbit (Murray & Dermott, 1999). On the other hand, Tamayo et al. (2015) show through numerical simulations that planets can still survive well beyond the above stability criterion if they capture in mean-motion resonance at low masses and grow together. This is because resonance mitigates the effect of close encounters and allows the planets to become more massive without disrupting the other planet's orbit quickly as is the case for non-resonant planets. For the system to be Hill stable, the maximum masses for the three outermost planets in the HL Tau disk are found by Tamayo et al. (2015) using Equation 4.2, taking the stellar mass to be  $M_* = 0.55 M_\odot$ :

$$M \lesssim M_{crit} = 8 \left( \frac{M_*}{M_\odot} \right) \left( \frac{\Delta a/a}{0.1} \right)^3 M_\oplus, \quad (4.2)$$

where  $\Delta a$  is the planet separation and  $M_{crit}$  is the maximum mass to ensure stability.

Therefore, according to numerical simulations of the HL Tau disk by Tamayo et al. (2015), if the outer three planets are not in mean-motion resonance they become unstable at conjunction timescale once they exceed the mass threshold beyond which their separation becomes less than  $\sim 3.5 r_H$ . However, if they are captured at resonances while they migrate through the disk, they can grow well past the above limit until they become so massive ( $\sim 40\%$  beyond mass of Saturn or  $0.44 M_J$ ) that their mutual gravitational perturbation at conjunctions brings them out of resonance at which point swift instability ensues (Tamayo et al., 2015). Moreover, their numerical simulation suggests that the system would be substantially more stable if not all the gaps were made by planets, particularly the more closely spaced gaps at 65.1 and 77.3 AU. They suggest that these two gaps may not be made by two different planets; there may instead be a single planet at 71.2 AU that has shaped a horseshoe-like gap in the disk of HL Tau. If four planets are considered instead of five in the HL Tau system, their numerical simulation puts a final mass limit of at least  $230 M_\oplus$  for the outer two planets if they are in mean-motion resonance.

Table 4.1 summarizes the masses and locations of the possible planets in the HL Tau system

obtained by the studies mentioned above and a few more. It shows that despite many attempts to constrain planetary parameters in the HL Tau disk, especially since the release of the ALMA image, much work is still needed to determine the number and parameters of its potentially embedded planets. This is what we present in this work where we try to reproduce the key features of the HL Tau disk using the dynamic model of a gas-poor disk to address whether some parameters of its planets, specifically their mass and semimajor axis, can be determined without the need for sophisticated models which are, nevertheless, required to fully describe gas-rich disks. Yet as mentioned earlier, our particle-only approach may be able to serve as a first step in characterizing planets in protoplanetary disks.

Table 4.1: Estimated locations and masses of possible planets forming HL Tau’s 5 major gaps. If the last two gaps are formed by a single planet at 71.2 AU, Tamayo et al. (2015) estimate its mass to be  $\lesssim 0.30$  if they are not in MMR and  $\gtrsim 0.72$  if they are. Pinte et al. (2016) also estimate the mass of a single planet at 69.0 AU forming the last two gaps to be at least  $0.44^{+0.05}_{-0.09} M_J$ .

<b>a (AU)</b>					<b>M (<math>M_J</math>)</b>					<b>Method</b>	<b>Ref.</b>
13.1	33.0	68.6			0.35	0.17	0.26			Hydrodynamic & radiative transfer	Jin et al. (2016)
13.2	32.3	68.8			0.2	0.27	0.55			SPH	Dipierro et al. (2015)
	$28 \pm 2$	$69 \pm 2$				0.8	2.1			Equation 4.1	Yen et al. (2016)
$13.5^{+0.4}_{-0.4}$	$32.4^{+0.6}_{-0.4}$	$65.2^{+1.3}_{-0.9}$	$77.2^{+0.8}_{-0.7}$		$88.8^{+5}_{-5}$ 0.85	$3.6^{+0.7}_{-0.6}$ 0.61	$1.5^{+0.5}_{-0.5}$ 0.62	$0.3^{+0.1}_{-0.1}$ 0.51		Hill Radius Equation 4.1	Akiyama et al. (2015)
$13.6^{+0.2}_{-0.2}$	$33.3^{+0.2}_{-0.2}$	$65.1^{+0.6}_{-0.6}$	$77.3^{+0.4}_{-0.4}$	$93.0^{+0.9}_{-0.9}$	?	?	$\lesssim 0.11$ NoMMR	$\lesssim 0.11$ NoMMR	$\lesssim 0.11$ NoMMR	N body sim, REBOUND package (Rein & Liu, 2012)	Tamayo et al. (2015)
					?	?	$\lesssim 0.30$ MMR	$\lesssim 0.30$ MMR	$\lesssim 0.30$ MMR		
$13.2^{+0.2}_{-0.2}$	$32.3^{+0.1}_{-0.1}$	$64.2^{+0.1}_{-0.1}$	$73.7^{+0.1}_{-0.1}$	91	$>0.02^{+0.01}_{-0.01}$	$>0.07^{+0.01}_{-0.01}$	$>0.03^{+0.00}_{-0.01}$	$>0.08^{+0.03}_{-0.05}$	$>0.11^{+0.03}_{-0.06}$	Surface density measurements	Pinte et al. (2016)

## 4.2 Method

### 4.2.1 The HL Tau Disk Profile

We use the FITS image of the HL Tau disk available publicly at the ALMA website and observed in dust continuum emission in band 7 for the highest resolution. The observed profile of the HL Tau disk used here is extracted by the following method:

We make a cross cut across the disk’s major axis to extract HL Tau’s radial brightness profile in  $Jy/beam$  per radial distance from the star. The extracted profile is 186 pixels long over a physical distance of 115 AU. However, the resolution of the image is only 35 milliarcseconds or  $\sim 5$  AU at 130 parsec (see NRAO, 2014) and so we assess that we really only have  $115/5 \approx 23$  bins for the purposes of determining our degrees of freedom (see section 4.2.4) and  $186/23 \approx 8$  pixels per bin.

### 4.2.2 Simulations

Our simulations are performed with a symplectic integrator based on the Wisdom–Holman algorithm (Wisdom & Holman, 1991). A fixed timestep of 150 days is used for all simulations. Only point particles are simulated, without the gas drag, radiation pressure, or the PR drag. These effects are likely to be important in sculpting the HL Tau disk but our purpose here is to determine what, if any, and how much of the planetary parameters can be recovered by the simplest possible model. The bins are weighted by the blackbody emission of their particles assuming dust albedo of 0.5 and emissivity of 1.0 at mm wavelength to calculate the equilibrium temperature of the disk particles. The stellar luminosity and effective temperature are taken to be  $8.3 L_{\odot}$  and 4000 K, respectively (Ruge et al., 2016).

Simulations are run for 10,000 years ( $\sim 1000$  inner orbits) and recorded at 100-year intervals. Three planets and 1000 particles are placed within the disk on circular orbits around a 1.3 Solar-mass central star (ALMA Partnership et al., 2015). Particles are removed if they reach a distance less than  $\sim 500$  Solar radii or greater than 220 AU. The planets are placed nominally at

11.7, 29.1, and 64.5 AU based on the locations of the gaps in the HL Tau disk, but the planet's locations will be varied as part of the fitting process, described later in Section 4.2.3.

Simulated disk profiles are created from the last 5 snapshots of the disk. The use of several snapshots increases our signal-to-noise without the computational expense associated with simulating additional particles, though it assumes that the disk is in a quasi-steady state. Examination of the disk during the final stages confirms that indeed the disk structures are well-established.

For plotting purposes, the simulation data is extracted into a histogram with 186 bins to match the observations. For calculation of the chi-square, the data is box-car smoothed down to the effective resolution of the observations (8.3 bin box-car).

### 4.2.3 Fitting

Best fit parameters are established on the basis of the chi-squared ( $\chi^2$ ) between the observational profile and a simulated profile normalized to the first bin in the observed profile. This normalization reduces our degrees of freedom by one. Minimization of the  $\chi^2$  parameter is accomplished using *Interactive Data Language* (IDL) and the Amoeba package which is a multi-dimensional derivative-free optimization algorithm based on the downhill simplex method of Nelder and Mead (Nelder & Mead, 1964). Typical Amoeba runs would require 900-1000 simulations and a total of 10 hours to complete. Amoeba requires the tolerance to be at least equal to the machine's double precision, so we set the tolerance to  $10^{-12}$ . This is the decrease in the fractional value of the  $\chi^2$  in the terminating step.

Chi-squared minimization using the Amoeba algorithm does not require calculating derivatives. Furthermore, each iteration only takes one or two function evaluations and therefore Amoeba converges faster than some other minimization routines such as non-linear least-square fitting using the Levenberg-Marquardt algorithm (Marquardt, 1944; Levenberg, 1963) which takes several calculations per iteration. Amoeba is also more robust for problems with stochastic components such as what we are dealing with here (e.g. the particle positions are

chosen randomly, which introduces some statistical noise to the profiles). These justify using the Amoeba algorithm for our purposes.

However, a downside to using Amoeba is that it can get to a point where the change in the parameter values becomes insignificant before a minimum is reached. Thus it is generally recommended to restart Amoeba from the point where it seems to have found a minimum (see Press et al., 1992) and this is what we do a few times until we achieve similar results. Our procedure was to first perform initial minimization runs using parameter values chosen arbitrarily, except for the semimajor axes of the three planets that were estimated from the locations of the major gaps in the HL Tau disk and allowed each parameter to vary by  $\pm 50\%$  by the minimization routine. From the lowest chi-squared obtained from these initial runs (our ‘initial solution’), in order to ensure as much as possible that the minimum  $\chi^2$  achieved is the global minimum, we perform 10 additional minimization runs where we change the initial conditions such that each parameter falls randomly within 10% of the one obtained from the initial solution. At the end, we record the parameters that produce the lowest  $\chi^2$  from the 10+1 Amoeba runs.

For our simulations here, we will fit 10 parameters of the planets and disk (in our model with the broken power-law but 7 when we use a single power-law for disk density distribution, see Section 4.3). We will assume that there are three planets on circular orbits. In addition to the masses and semimajor axes of these three planets, we also fit a power-law to the disk surface density. The surface density of circumstellar disks is generally taken to have a profile of the form  $\Sigma \propto R^{-\alpha}$  with the power-law index,  $\alpha$ , is between 0 and 1 depending on the mass of the protoplanetary disk (Andrews & Williams, 2007b) (Note that the power-law index derived from Minimum Mass Solar Nebula is 1.5 (Weidenschilling, 1977)). However, use of a single power-law does not well reproduce the radial profile of HL Tau’s flux density. A much lower  $\chi^2$  value is obtained by selecting a different power-law index beyond the location of the outermost planet (see Section 4.3). Yen et al. (2016) also use a broken power-law in their measurements of gap widths and depths in the HL Tau disk where the slopes of the dust distribution based on

the column density of  $HCO^+$  are found to be  $-0.5 \pm 0.2$  at  $\sim 20$  AU and  $-0.9 \pm 0.3$  at  $\sim 60$  AU, suggesting a steep decline in dust continuum emission beyond where the outer major gap lies. Jin et al. (2016) propose that the deficit in dust in the outer part of the HL Tau disk is due to the inward drift of dust caused by gas drag and the absence of a source to supply the dust at large radii (also see Birnstiel & Andrews, 2014). In fact, disks are found to have exponentially tapered edges and the exponential decrease in dust surface density has also been observed for a number of other circumstellar disks (see for instance, McCaughrean & O’Dell, 1996) with power-law indices beyond the above-mentioned range, suggesting that the pure power-law (i.e.  $\Sigma \propto r^{-\alpha}$ ) does not accurately represent a disk’s intensity profile and must be replaced by an exponentially truncated density distribution with  $\Sigma \propto r^{-\gamma}$ , where  $\gamma$  is the exponent in the viscosity dependence on distance from the star (e.g. Hartmann et al., 1998). For simplicity (that is, to avoid adding additional parameters to our fit), we will assume a standard power-law slope without an exponential term. Therefore, we argue that our fit to the radial profile of the outer disk would be improved if we adopt the above surface density profile and incorporate dust re-generation and gas drag in our model which we leave to a future work.

#### 4.2.4 Uncertainties

Uncertainties in the fitted parameters are estimated based on the chi-square values. The number of degrees of freedom,  $\nu$ , will be the effective number of bins (23, see Section 4.2.1) minus one for the normalization discussed in Section 4.2.3, and minus one for each free parameter. We have 10 free parameters, giving us a total of 12 degrees of freedom.

The uncertainties to be at the locations in phase-space can be approximated as where the  $\chi^2$  value is increased over its minimum value by an amount  $\Delta\chi^2$  dependent on the degrees of freedom,  $\nu$ , and the stringency of the uncertainty bounds desired. Here we choose a  $p = 0.95$  (nominally  $2\sigma$ ) confidence region, which means that our uncertainties correspond to the locations for which (Press et al., 1992):

$$Q\left(\frac{\nu}{2}, \frac{\Delta\chi^2}{2}\right) = 1 - p, \quad (4.3)$$

where  $Q$  is the incomplete gamma function, and  $\Delta\chi^2$  gives the increase in  $\chi^2$  corresponding to our uncertainty.

Note that we compute our uncertainties from chi-squared values with all the parameter values except the one in question held constant. This implicitly assumes that the parameters are uncorrelated, which we assume here for reasons of simplicity and practicality. Our  $\chi^2$  is derived by a process with inherent stochasticity (i.e. the initial conditions of particles within the disk have a random component), thus we have too many free parameters and too noisy a system to determine the covariance between them all effectively. This will be more apparent when the uncertainty results are discussed in Section 4.3.

## 4.3 Results

As mentioned earlier in Section 4.2.3, a single power-law index for the surface density cannot reproduce the observed density profile of the HL Tau disk due to a steep fall-off in the outer part of the disk beyond the location of the outermost planet. This is shown by figure 4.1. Therefore, we break the disk into two segments, each having a different power-law index,  $\alpha_1$  and  $\alpha_2$ , which we leave as free parameters in our simulations. We also allow the location of the boundary between the two segments to vary, and introduce an additional parameter to allow for a change in the surface density of the disk at the boundary between the two segments.



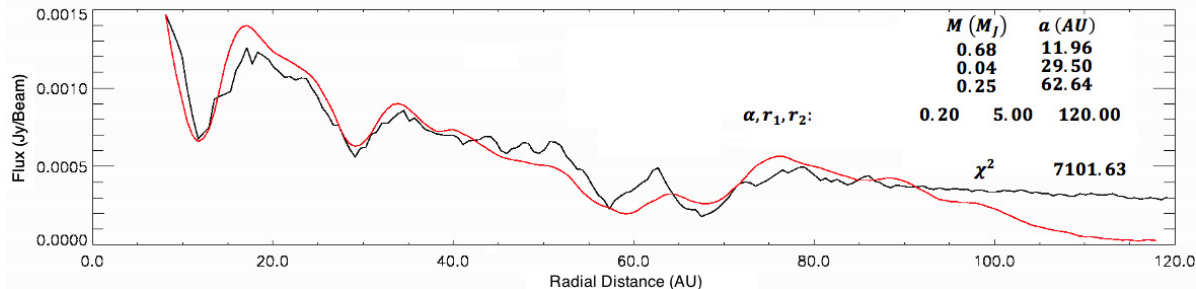


Figure 4.1: Comparison between the radial profile of the HL Tau disk extracted from the FITS image observed by ALMA (red) and our simulation (black). We place three planets at nominal radii of 11.03, 28.91, and 64.52 AU and allow Amoeba to determine the best fit parameters (i.e. the three planet masses,  $M(M_J)$ , and semimajor axes,  $a(AU)$ , as well as the power-law index,  $\alpha$ ) by minimizing the chi-squared. For simplicity, we assume that the three planets are in circular orbits but acknowledge that the gaps in the HL Tau disk are found to have some eccentricity (see Section 4.1.1). Here we use a single power-law surface density index for the disk that extends from  $r_1 = 5.0$  AU to  $r_2 = 120.0$  AU. However, the model with a single power-law index fails to reproduce the disk profile beyond the location of the outermost planet.

To obtain the best fit values, we thus need to include 10 free parameters in our simulations: one for each planet’s mass ( $M$ ) and semimajor axis ( $a$ ), two for the surface density power-law indices ( $\alpha_1$  and  $\alpha_2$ ), one for the transition point that separates the two parts of the disk with different slopes ( $r_2$ ), and finally one for the fractional increase in surface density at the transition point ( $f$ ). Note that we keep  $r_1$  and  $r_3$  fixed at 5.0 and 120.0 AU which roughly mark the inner and outer edges of the HL Tau disk. The use of the broken power-law for the disk’s surface density as well as introducing an increase in the surface density at the boundary between the two segments result in a lower  $\chi^2$  value which is shown by Figure 4.2.

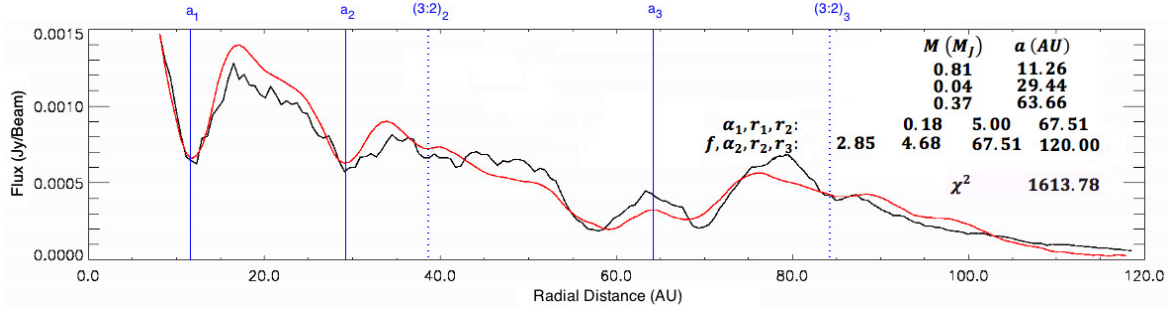


Figure 4.2: Same as Figure 4.1 except that we use two different power-law indices for dust surface density distribution to account for the exponentially decaying surface density profile of the HL Tau disk and the steeper slope beyond the orbit of the planet that we place inside the third major gap. The chi-squared value in this case is significantly improved. The nominal locations of the three planets are shown by the solid blue lines. We also identify two gaps that fall at mean-motion resonances with the planets at  $a_2$  and  $a_3$  and mark their locations with dotted blue lines (see Section 4.3.1 for a discussion on possible MMR gaps in the HL Tau disk).

The  $2\sigma$  uncertainties for each parameter are found using the procedure outlined in Section 4.2.4. Figure 4.3 shows uncertainty calculations for the three planet masses. In each case, we fit a polynomial spline curve of the lowest possible degree to the bowl-shaped part of the  $\chi^2$  surface and mark the two points where it crosses the  $2\sigma$  cut-off. The difference between either of those points and the lowest  $\chi^2$  value determines the positive and negative uncertainties.

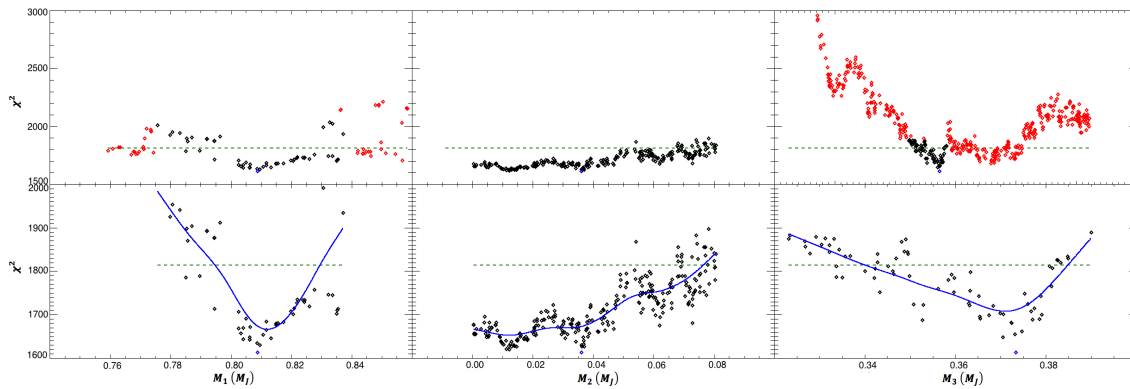


Figure 4.3: Uncertainty calculations at  $2\sigma$  confidence level for the masses of the three planets in the HL Tau disk:  $M_1$  (left),  $M_2$  (middle),  $M_3$  (right). We exclude the points that fall outside the bowl-shaped part of the  $\chi^2$  surface around the minimum (the blue diamond) as well as those that are outside the  $2\sigma$  level by more than 10%. The excluded points are shown by the red symbols in the top panels. We then fit a spline curve of the lowest possible degree (the blue curve) and note the points where it crosses the  $2\sigma$  cut-off (the dashed green line). The difference between the minimum  $\chi^2$  and either of those points is taken as the uncertainties for the parameter value. Note that we are unable to constrain the negative uncertainty for  $M_2$ .

The best fit parameters obtained and their uncertainties are shown in Table 4.2 for the masses and semimajor axes of the three planets that we place in the major gaps of the HL Tau disk. Though some authors have placed two planets in the last two major gaps of the HL Tau disk (at  $\sim 59$  and  $70$  AU), we are able to produce both gaps with a single planet at  $\sim 64$  AU. We attribute the increase in dust emission at the location of the outermost planet to particles that are trapped in 1:1 MMR with the planet. For comparison, in Table 4.2 we also provide the range of values proposed in the literature for the orbital radii and masses of the three planets (see Table 4.1 for more details). All our parameters are well within the range of values given by others who have studied the HL Tau disk structure using various other techniques as listed in Table 4.1, except for the mass of the second planet, which overlaps the literature range but extends to smaller masses.

Table 4.2: The best-fit parameters and uncertainties obtained using the downhill simplex method for the semimajor axes and masses of the three planets that are likely responsible for sculpting the prominent gaps of the HL Tau disk (top row) along with the range of values proposed by others (bottom row). Note that we exclude mass measurements using the size of each planet’s Hill radius by Akiyama et al. (2015) since that has led to obtaining a very large (stellar) mass for the innermost planet.

<b>a (AU)</b>			<b>M (<math>M_J</math>)</b>		
$11.26^{+0.20}_{-0.11}$	$29.44^{+2.56}_{-3.62}$	$63.66^{+0.46}_{-0.37}$	$0.81^{+0.02}_{-0.01}$	$0.04^{+0.04}$	$0.37^{+0.01}_{-0.03}$
[13.0, 13.9]	[26.0, 33.5]	[64.1, 71.0]	[0.01, 0.85]	[0.06, 4.3]	[0.02, 2.0]

Our best-fit parameters for the power-law indices of the disk’s surface density profile are  $\alpha_1 = 0.18^{+0.01}_{-0.01}$  and  $\alpha_2 = 4.68^{+0.06}_{-0.05}$  where the break occurs at  $r_2 = 67.51^{+0.68}_{-0.23}$ . We note that these two values are very different from each other and from what Yen et al. (2016) report (see Section 4.2.3), partly owing to the fact that we introduced a sudden increase in the disk’s surface density by almost a factor of 3 (i.e.  $f = 2.85^{+0.05}_{-0.10}$ ) where we broke the intensity profile of the disk into the two segments. However, our surface density slope in the outer disk is close

to the value obtained by Pinte et al. (2016). According to their model, the surface density profile of the HL Tau disk has a slope of -3.5 out to about 75 AU but falls off faster in the outer part of the disk. They find the power-law slope in the outer disk to be -4.5 which is similar to what we obtain from our model. They attribute the change in the surface density of dust to two possible reasons: lack of efficient grain growth in the outer disk or the removal of a significant fraction of mm-sized grains from the outer disk via radial migration of dust. When using a single power-law for the disk's surface density, we find  $\alpha$  to be  $\sim 0.20$ . We therefore conclude that we would need a more robust model for the disk surface density to better estimate the power-law indices in the two segments.

On the other hand, a comparison between planetary parameters (masses and semimajor axes) that we obtain using our relatively simpler model of the HL Tau disk where we do not consider the effect of gas drag, radiation pressure or the PR drag shows that the values we obtain are within the range proposed by others found using various models with higher levels of complexity. Therefore, our model is successful in reproducing the observed intensity profile of the HL Tau disk without the need to include certain elements that are necessary to fully study a gas disk.

### 4.3.1 MMR Gaps in the HL Tau Disk

The orbital radii of the planets found by our fitting procedure represent the locations of the three major gaps in the HL Tau image to within uncertainties (where the two gaps made by the outermost planet are considered to be a single wide gap separated by particles in 1:1 mean-motion resonance with a planet at  $\sim 64$  AU). A closer look at the observed intensity profile of the HL Tau disk reveals a few other relatively narrower gaps which have motivated some authors to include more planets in their modeling of the HL Tau disk. However, our earlier studies, Tabeshian & Wiegert (2016, 2017), have shown that not all disk gaps need to contain planetary bodies and that some gaps can, in fact, be made via mean-motion resonance with a planet that is located outside the gaps and can be used to learn about the hidden planets. We

note that our model of the HL Tau disk which only includes three planets is able to reproduce some of those narrower gaps as well. In fact, given the locations of the second and the third planets, we argue that the gaps seen at  $\sim 38$  and  $\sim 84$  AU are made by exterior 3:2 MMR with those two planets, respectively. These are shown by the vertical dotted lines in Figure 4.2. Furthermore, the location of the first and second planets places them in a 4:1 MMR with each other.

In order to visually compare the result of our simulation with ALMA’s image of the HL Tau disk, we make a simulated image using the Common Astronomy Software Applications (CASA) for simulating ALMA observations (McMullin et al., 2007) based on the disk produced with our best-fit parameters. To make the CASA simulated image, we assume that our disk is placed at the HL Tau distance of 130 pc and therefore has the same radial size on the sky. We also assume that the particles are perfect blackbodies at local thermal equilibrium and take the disk’s total flux to be 700 mJy at 1.3 mm (Kwon et al., 2011). Stellar radius and effective temperature are  $6.0 R_{\odot}$  and  $4000 K$ , respectively (Ruge et al., 2016). We set the image resolution at 35 milliarcseconds or  $\sim 5$  AU to match that of ALMA’s observation of the HL Tau disk and use all the 50 available antennas in the 12 m array. We assume that the disk is observed for a total of 4 hours and set the integration time to 10 sec per pointing. The RA and Dec of the center of the image are  $\alpha = 04^h 31^m 38^s.45$  and  $\delta = 18^{\circ} 13' 59''.0$ , J2000 (Tamayo et al., 2015). Beam deconvolution is done using CASA’s *CLEAN* algorithm. The result is shown by Figure 4.4. We adopt the same nomenclature used by ALMA Partnership et al. (2015) for the dark gaps that we see in our simulations, except that we take the two gaps around the outermost planet to be the same with the planet in the middle.

It must be noted that we are not claiming that the properties of gas-rich disks can be fully learned from simple models that do not incorporate gas and radiation forces. However, based on the results of our simulations to reproduce the intensity profile of the HL Tau disk, we argue that reasonable matches with observations can be achieved with relatively simple particle-only models of this intrinsically much more complicated gas disk. Therefore, at least as far as

understanding the dynamics of the system is involved, we make the case that simple models could be used to extract useful information about the number and properties of possible planets embedded in gas-rich disks which could be used in future thorough analyses of these disks.

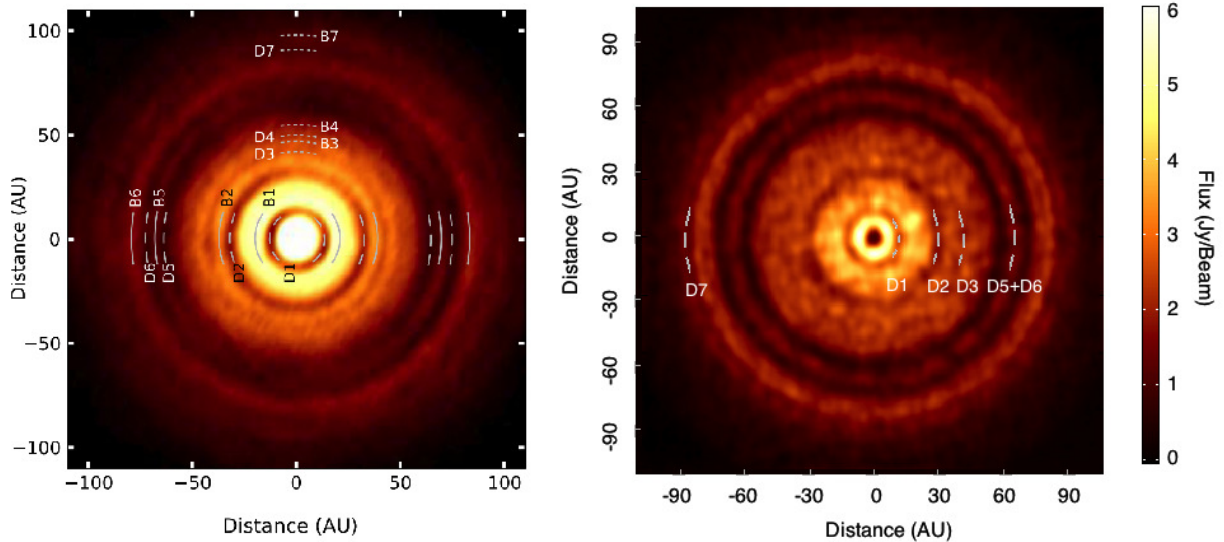


Figure 4.4: Comparison between ALMA’s (deprojected) image of the HL Tau disk (ALMA Partnership et al., 2015) on the left with a CASA simulated image drawn from our best-fit parameters on the right. The dark and bright rings are labeled D1 through D7 and B1 through B7 by ALMA Partnership et al. (2015). We use the same notation to mark the locations of the gaps that we believe are sculpted by planets in the HL Tau disk (D1, D2, and D5+D6) as well as the two narrower gaps (D3 and D7) that we believe to be due to mean-motion resonances with the embedded planets. The mean-motion resonance gaps are also marked on Figure 4.2 with dotted blue lines. Note that to make this CASA simulated image, we increased the number of disk particles by 10 times for clarity.

## 4.4 Summary and Conclusions

The advancements of observing capabilities in the recent years have revolutionized our understanding of planet formation and evolution. Interferometric data made available in the mm and sub-mm regime, particularly by ALMA, has provided remarkably detailed images of circumstellar disks with unprecedented angular resolution of a few milliarcseconds. In protoplanetary disks, the structures observed are mostly believed to be due to tidal interactions with unseen planets that clear gaps as they accumulate and then sweep up their orbits of gas and dust.

Therefore, studying such structures would provide insight into the processes involved in the formation and evolution of planets and planetary systems and would help determine some planetary parameters without the need to resolve the planets themselves, a task that has proved to be challenging.

We provided a dynamical model of the HL Tau disk, the most detailed protoplanetary disk structure observed by ALMA to this day, without much of complex physics typically required in modeling gas-rich disks. In particular, we hypothesized that the gas does not dominate the dynamics, and set out to explore whether the radial profile of the HL Tau disk could be recovered using a particle-only model. We were, indeed, able to reproduce the disk's intensity profile and determined the masses of the planets that could likely be sculpting the most prominent gaps in the HL Tau disk. The values we obtained for the masses and radial distances of the three planets we believe are embedded in this disk are within the range quoted in the literature that are derived from more complicated hydrodynamic simulations. We note that the mass of the middle planet in our model also overlaps previous values but is more on the low end. Furthermore, we recovered the tapered-edge of the disk, in which the surface density of the disk changes exponentially beyond the orbit of the outermost planet, as also noted by others and determined the surface density slope of the disk in the two regions using data from ALMA's observation at band 7. Though more work is required to understand dust density distribution in protoplanetary disks, we found the disk to have a significantly different dust density distribution in the outer regions which is consistent with the exponential fall-off in dust emission observed in gas disks. Another achievement by our model was reproducing a few narrow gaps away from the orbit of the three planets. Whereas the number of planets in the HL Tau disk has remained a matter of debate, our results indicate that at least 5 gaps can form in the HL Tau disk by including only 3 planets: the additional gaps are attributed to mean-motion resonances with the embedded planets.

Our intention here is not to undermine the importance of hydrodynamic and SPH analyses of gas-rich disks. Though computationally more intensive, such studies are undoubtedly

essential in gaining a better understanding of the underlying physics at work in gas disks as sites of planet formation and evolution. However, simpler particle-only models can be used to glean some important information with regards to the dynamics of planet-disk interactions. Such models provide initial conditions to hydrodynamics codes as a first step toward in-depth studies of disk structures, particularly those that are believed to have been formed by unseen planets.



# Bibliography

- Akiyama, E., Hasegawa, Y., Hayashi, M., et al., 2016, *ApJ*, 818, 158.
- ALMA Partnership, Brogan, C. L., Pérez, L. M., et al., 2015, *ApJL*, 808, L3.
- Andrews, S. M. and Williams, J. P., 2007b. *ApJ*, 659, 705.
- Andrews, S. M., Wilner, D. J., Espaillat, C., et al., 2011, *ApJ*, 732, 42.
- Birnstiel, T. and Andrews, S. M., 2014, *ApJ*, 780, 153.
- Casassus, S., van der Plas, G., M. S. P., M., Sebastian Perez, et al. 2013, *Nature*, 493, 191.
- Dipierro, G., Price, D., Laibe, G., et al., 2015, *MNRAS*, 453, L73.
- Duffell, P. C. and MacFadyen, A. I., 2013, *ApJ*, 769, 41.
- Fouchet, L., Maddison, S. T., Gonzalez, J. F., et al., 2007, *A&A*, 474, 1037.
- Fung, J., Shi, J. M., and Chiang, E., 2014, *ApJ*, 782, 88.
- Gladman, B., 1993, *Icarus* 106, 247.
- Haghighipour, N. and Boss, A. P., 2003, *ApJ*, 583, 996.
- Hartmann, L., Calvet, N., Gullbring, E., et al., 1998, *ApJ*, 495, 385.
- Jin, S., Li, S., Isella, A., et al., 2016, *ApJ*, 818, 76.
- Kanagawa, K. D., Muto, T., Tanaka, H., et al., 2015, *ApJ*, 806, L15.

- Kitamura, Y., Momose, M., Yokogawa, S., et al., 2002, *ApJ*, 581, 357.
- Kwon, W., Looney, L. W., and Mundy, L. G., 2011, *ApJ*, 741, 3.
- Levenberg, K., “*A Method for the Solution of Certain Non-Linear Problems in Least Squares*,” 1944, *The Quarterly of Applied Mathematics* 2, 164.
- Maddison, S. T., Fouchet, L., and Gonzalez, J. F., 2007, *Ap&SS*, 311, 3.
- Marquardt, D., “*An algorithm for least-squares estimation of nonlinear parameters*,” 1944, *Journal of the Society for Industrial and Applied Mathematics* 11, 431.
- McCaughrean, M. J. and O’Dell, C. R., 1996. *AJ*, 111, 1977.
- McMullin, J. P., Waters, B., Schiebel, D., et al., 2007, in Shaw R. A., Hill F., Bell D. J., eds, *Astronomical Data Analysis Software and Systems XVI* Vol. 376 of *Astronomical Society of the Pacific Conference Series*, CASA Architecture and Applications. p. 127.
- Murray, C. D. and Dermott, S. F., 1999, *Solar System dynamics* (Cambridge: Cambridge Univ. Press).
- Nelder, J., A. and Mead, R., 1964. *A simplex method for function minimization*, *The Computer Journal*, 7, 308-313.
- NRAO, 2014, “*Birth of Planets Revealed in Astonishing Detail in ALMA’s ‘Best Image Ever’*”, National Radio Astronomy Observatory (Press Release).
- Paardekooper, S. J. and Mellema, G., 2004, *A&A*, 425, L9.
- Pinte, C., Dent, W. R. F., Ménard, F., et al., 2016, *ApJ*, 816, 25.
- Press, W., Teukolsky, S., Vetterling, W., et al., 1992, *Numerical Recipes in C*, Cambridge University Press, Cambridge.

- Price, D. J., Wurster, J., Nixon, C., et al., 2017, Publications of the Astronomical Society of Australia (PASA), arXiv:1702.03930.
- Rein, H. and Liu, S. F., 2012, *A&A*, 537, A128.
- Ruge, J. P., Flock, M., and Wolf, S., 2016, *A&A*, 590, A17.
- Shakura, N. I. and Sunyaev, R. A., 1973, *A&A*, 24, 337.
- Tabeshian M. and Wiegert P. A., 2016, *ApJ*, 818, 159.
- Tabeshian M. and Wiegert P. A., 2017, *ApJ* (submitted).
- Tamayo, D., Triaud, A. H. M. J., Menou, K., et al., 2015, *ApJ*, 805, 100.
- Takahashi, S. Z. and Inutsuka, S. I., 2014, *ApJ*, 794, 55.
- van der Marel, N., van Dishoeck, E. F., Bruderer, S., et al., 2013, *Science*, 340, 1199.
- Weidenschilling, S. J., 1977, *MNRAS*, 180, 57.
- White, R. and Hillenbrand, L., 2004, *ApJ*, 616, 998.
- Wisdom, J. and Holman, M. 1991, *AJ*, 102, 1528.
- Yen, H. W., Liu, H. B., Gu, P. G., et al., 2016, *ApJL*, 820, L25.
- Zhang, K., Blake, G., and Bergin, E., 2015, *ApJL*, 806, L7.

# Chapter 5

## Summary, Conclusions, and Future Prospects

### 5.1 Summary and Conclusions

Our observing capabilities of circumstellar disks reached a milestone in November of 2014 with the release of an image of a protoplanetary disk around the young star HL Tau by the *Atacama Large Millimeter/submillimeter Array* (ALMA) (see NRAO, 2014), transforming our understanding of structures formed in circumstellar disks which are likely the result of gravitational interaction with planets concealed in these disks. Considering the difficulty in direct detection of extrasolar planets, observations of the gravitational signature of planets embedded or near circumstellar disks can not only provide important clues into their existence but can also be used to study some of their properties such as semimajor axis, mass, and orbital eccentricity (see Appendix A for a brief overview of orbital elements).

Circumstellar disks were first revealed indirectly through analyses of their Spectral Energy Distributions (SEDs). However, more recent direct observations of these disks have provided a wealth of information and revealed rich structures including spirals, offsets, warps, clumps, rings and gaps that offer invaluable information about disk dynamics. Although interactions

with planets may not be the only reason such structures are formed in circumstellar disks, planet-disk dynamics remains an integral part of the observed architecture of disks, from young primordial gas-rich disks to older, left-over disks of dust and planetesimals that have lost most of their gas content.

This work began by considering gravitational interactions of a single planet with a gas-poor and dynamically cold debris disk in an attempt to propose an indirect technique to detect as well as characterize extrasolar planets via their resonant signature on the disk. Since the discovery of the first planet outside the Solar System in 1992, more than 3000 planets have been confirmed to exist beyond the Solar System and a few thousand more are awaiting confirmation. The majority of these planets have been found through indirect means that are mostly based on the planets' effects on their host stars. This is due to the fact that direct detection of exoplanets has been proved to be difficult even with the present-day technology. We proposed a new indirect method for exoplanet detection and characterization that is based on the gravitational perturbation of a single, non-migrating planet on a debris disk via mean-motion resonances (MMRs). Each planet detection technique has its own limitations and we often rely on more than one technique to confirm exoplanets and measure their mass and orbital parameters. Thus it is important to understand the advantages and shortcomings of each technique.

First noted in 1867 as distinct gaps in the distribution of asteroids' semimajor axis in the Solar System's Main Asteroid Belt (Kirkwood, 1867), structures formed by mean-motion resonances can be used in the study of planets causing them, which often remain challenging to detect directly. Using the already established relation between the location and width of a MMR gap and the location and mass of the planet with which it is in resonance (see Equations 2.2 and 2.4 and Murray & Dermott (1999)), we set out to quantify how some planetary parameters can be determined from the locations and widths of observed gaps. This was achieved through numerical simulations based on the Wisdom-Holman algorithm (Wisdom & Holman, 1991) where we simulated both interior and exterior MMRs with a single planet on zero or very low ( $e \sim 0.05$ ) eccentricity orbit (see Chapter 2). In both cases, our simulations revealed a

MMR gap at the planet's 2:1 (interior and exterior) resonance even when the mass of the planet was as small as  $1.0 M_{\oplus}$ . We conclude that some of these gaps are wide enough that may be revealed through telescopic observations of debris disks with current technology.

Our results showed a linear relationship between the mass of the planetary perturber and the width of the MMR gap it creates, in line with our theoretical calculations of gap widths as a function of planetary mass. Thus we argued that disk gaps do not necessarily need to contain planetary bodies and that MMR gaps can be highly diagnostic of the properties of the planets creating them. These results are published in *The Astrophysical Journal* (see Tabeshian & Wiegert, 2016).

A slight increase in the orbital eccentricity of the planetary perturber was found to produce an additional gap in the disk, which prompted us to extend our study to the case where the planet can take on a wider range of orbital eccentricities (see Chapter 3). We noted that the additional gap occurs at a higher order resonance, in this case 3:1, which can not only be alternatively used to measure planetary parameters, especially if the 2:1 gap is eroded by increasing planet mass and/or eccentricity, but it can also be used to distinguish 3:1 from 2:1 MMR if both gaps are observed. This is important because in cases where the planet is undetected, once we can identify which resonance gap we see in the disk, determining the planet's semimajor axis becomes trivial. Following the same analysis from our earlier work, we quantified how the mass of a planetary perturber placed exterior and interior to a debris disk can be measured from the width of both 2:1 and 3:1 gaps. Moreover, we showed that the orbital eccentricity of the planetary perturber could also be determined from the forced eccentricity at the semimajor axes of the MMR gaps, assuming that the disk particles have negligible free eccentricities.

Unlike gaps formed in the feeding zone of planets that are generally azimuthally symmetric (unless there is significant particle trapping at the planet's 1:1 MMR or if it is caused by geometric effects, see Chapter 1, Section 1.2.2), we found gaps formed by MMRs away from the orbit of the planet to not only be asymmetric about the star but also to have different shapes for interior versus exterior 2:1 and 3:1 resonances. According to our simulations, a 2:1 interior

MMR forms two arcs whose centers lie at the planet's inferior and superior conjunctions while the same gap is a single arc with its center at the planet's opposition if it is formed exterior to the planet's orbit. Furthermore, we noted that while the center of the 2:1 resonance gap traces the planet, a MMR gap formed by the 3:1 resonance with a planet has its center fixed in the inertial frame at the disk's apocenter for interior MMR and at pericenter if it is formed by exterior resonance. Therefore, the distinctive shape and behavior by MMR gaps can be used to direct targeted searches for extrasolar planets, whose direct observation has remained challenging. We, therefore, provided an algorithm for measuring planetary parameters, in particular semimajor axis, mass, and orbital eccentricity based on the location, width, and eccentricity of gaps formed through mean-motion resonances. Furthermore, we investigated the observability of MMR gaps using the Common Astronomy Software Applications (CASA) for simulating observations by ALMA (McMullin et al., 2007) and concluded that under certain conditions, detecting MMR gaps is within the reach of our current observing capabilities. These results are submitted for publication to *The Astrophysical Journal* (see Tabeshian & Wiegert, 2017).

Adding gas to circumstellar disks introduces an extra level of complication, making the study of any structures in gas disks computationally challenging. Therefore, in Chapter 4, we examined the question of whether a simpler particle-only model can be used as a first step to understanding dynamical structures in gas disks, particularly those formed by planets, to determine the nature of the structures as well as some parameters of the hidden planets. For this purpose, we chose the famous image of the HL Tau disk observed by ALMA in dust continuum emission at band 7 and tried to match its intensity profile using the same numerical model we applied to our previous work with debris disks. We placed three planets in the major gaps of the HL Tau disk and allowed their masses and semimajor axes to vary by our fit. The fit was made by comparing our simulation with HL Tau's radial profile by minimizing the chi-squared value using the downhill simplex method of Nelder and Mead (Nelder & Mead, 1964). To match the radial profile of the HL Tau disk, in addition to fitting the masses and semimajor axes of the three planets, we fit a double power-law model for dust surface density distribution where

we also allowed the boundary between the two segments with different power-law indices as well as the fractional increase in dust surface density at that boundary to be changed by our fit. The best-fit parameters obtained for the masses and semimajor axes of the planets are all well within the range of values estimated by hydrodynamic simulations, except for the mass of the second planet, which overlaps that range but extends to lower values. The best-fit planetary parameters were  $0.81_{-0.01}^{+0.02}$ ,  $0.04^{+0.04}$ , and  $0.37_{-0.03}^{+0.01}$  Jupiter-mass for the planets at  $11.26_{-0.11}^{+0.20}$ ,  $29.44_{-3.62}^{+2.56}$ , and  $63.66_{-0.37}^{+0.46}$  AU.

Our simulations also reproduced a few narrower gaps that appear in ALMA's image of the HL Tau away from the orbit of the three planets. The nature of these gaps has been a matter of debate but based on our simulations, we believe that they are the result of planet-disk interactions via mean-motion resonances. On the other hand, we are not as certain about the power-law indices we found for the disk's surface density distribution. In fact, the density distribution in the HL Tau disk - and in protoplanetary disks in general - is not well constrained in the literature and we need a more robust model to be able to prescribe power-law indices that represent HL Tau's density distribution. Nevertheless, our results indicate that we can, indeed, use a rather simpler particle-only model to extract some valuable information from complicated systems involving gas disks, especially with regards to their embedded planets before applying a disk hydrodynamic model to investigate the disk and planet properties more thoroughly.

## 5.2 Future Prospects

Astrophysical disks are complex systems. Future studies will improve our understanding by challenging the assumptions and simplifications of current models. For example, for planet interactions with debris disks, we assumed that the system contains only one planet. However, more than 70% of the confirmed extrasolar planets to date are found in multiple-planet systems<sup>1</sup> while the statistics could suffer from detection bias inherent to the search for extrasolar planets.

---

<sup>1</sup><https://exoplanets.nasa.gov/>



Therefore, considering that planets most likely have at least one other planetary companion, the need to investigate the effect of multiple planets on MMR structures as well as the effect of secular resonances formed by precessing planets cannot be overlooked. This work could then be extended to investigate MMRs in Saturn's rings that are affected by multiple satellites. We also assume that the system is well-established and that all planetary migration has stopped. However, planet migration through the disk can affect the dynamic sculpting of the disk and needs to be thoroughly investigated.

Another assumption we made for simplicity in our model is that the disk particles only interact gravitationally with the planet, thereby ignoring particle-particle interactions as well as the effects of the radiation pressure and the Poynting-Robertson (PR) drag. These simplifications are justified when considering dynamically cold debris disks and where the collisional lifetime of dust is shorter than the timescale for the inspiralling of dust due to the PR drag (see Wyatt et al. (1999) and our discussion in Chapter 3, Section 3.2.3). However, future models should include these effects for more precision.

We also assumed that the orbital eccentricities of disk particles are defined solely by the forced eccentricity of the planet at their semimajor axes and that they have no free eccentricity, an assumption justified in studying dynamically cold debris disks. Another assumption that arises from the disk being dynamically cold is that the disk particles lie in the same orbital plane as the planet. Although studies have shown that a planet inclined to a disk can cause the disk to be warped, (see for instance Augereau et al., 2001), our preliminary results using a small orbital inclination for the planet relative to the plane containing the disk particles revealed no significant difference in MMR gap structures but needs to be studied in more detail.

Varying the surface density distribution of disk particles in our simulations as well as simulating disks with a combination of various particle sizes are also important in quantifying planet-disk dynamical interactions. On the same note, modelling MMR structures in disks with ongoing collisional fragmentation must also be incorporated in our model. It must be noted that although some authors have studied collisional debris disks through simulations (see

for instance Nesvold & Kuchner, 2015), the effect of collisional fragmentation on determining planetary parameters from MMR structures remains to be studied.

Our modeling of the HL Tau disk, though successful in illustrating that dynamics of a protoplanetary disk can be explained to some extent with a simpler gas-poor model, needs further improvements especially with regards to the use of a better model for dust density distribution that includes factors such as the scale height of the disk, disk viscosity and temperature, dust replenishment via collision among larger bodies, planet migration, secular effects, etc. Future models should also include radiation effects such as stellar radiation pressure and the PR drag as well as more planets to investigate the structure of the HL Tau disk more thoroughly.

Planet-disk dynamical interactions are important in shaping the architecture of circumstellar disks. With direct detection of extrasolar planets being difficult to achieve, gaps and other symmetric and asymmetric structures in circumstellar disks can serve as potential signatures of hidden planets. As ALMA and other facilities continue to image extrasolar disks with unprecedented resolution and sensitivity, planet hunters would have the increasingly powerful tool of detecting and characterizing extrasolar planets through their gravitational imprint on circumstellar disks.

# Bibliography

Augereau, J. C., Nelson, R. P., Lagrange, A. M., et al., A&A, 370, 447.

Kirkwood, D., 1867, *Meteoric Astronomy: A Treatise On Shooting-stars, Fireballs, & Aerolites*, Philadelphia, PA: J. B. Lippincott & Co.

McMullin, J. P., Waters, B., Schiebel, D., et al., 2007, in Shaw R. A., Hill F., Bell D. J., eds, *Astronomical Data Analysis Software and Systems XVI* Vol. 376 of *Astronomical Society of the Pacific Conference Series*, CASA Architecture and Applications. p. 127.

Murray, C. D. and Dermott, S. F., 1999, *Solar System dynamics* (Cambridge: Cambridge Univ. Press).

Nelder, J., A. and Mead, R., 1964., *A simplex method for function minimization*, *The Computer Journal*, 7, 308-313.

Nesvold, E. R. and Kuchner, M. J., 2015, *ApJ*, 798, 83.

NRAO, 2014, “*Birth of Planets Revealed in Astonishing Detail in ALMA’s ‘Best Image Ever’*”, *National Radio Astronomy Observatory* (Press Release).

Tabeshian M. and Wiegert P. A., 2016, *ApJ*, 818, 159.

Tabeshian M. and Wiegert P. A., 2017, *ApJ* (submitted).

Wisdom, J. and Holman, M., 1991, *AJ*, 102, 1528.

Wyatt M. C., Dermott S. F., Telesco C. M., et al., 1999, *ApJ*, 527, 918.

# Appendix A

## Orbital Elements

*The contents of this appendix are adapted from Murray & Dermott (1999) and Roy (2005).*

The orbit of a particle (e.g. a planet) around a central body (e.g. the host star) may fully be described by a set of six parameters, called the orbital elements, two of which specify the size and shape (and hence the ‘nature’) of the orbit, three define the orientation of the orbit and the remaining element marks the position of the orbiting body at any given time. Orbital elements that specify angles are measured with respect to a reference plane and a reference line. In the case of Solar System objects, the reference plane is taken to be the plane of Earth’s orbit around the Sun (i.e. the ecliptic) and the reference direction is toward the first point of Aries ( $\Upsilon$ ) which is the direction of the vernal equinox (i.e. where the Sun appears to be on the first day of Spring) and where the ecliptic intersects Earth’s celestial equator. These six elements, shown by Figure A.1 are briefly outlined here.

### A.1 Semimajor Axis ( $a$ )

Keplerian orbits are elliptical with the star at one focus of the ellipse. Therefore, the planet-star distance varies over the orbit of the planet with the maximum and the minimum distances called the apocenter (apoastron or apoapse) and the pericenter (periastron or periapse), respectively.

The longest diameter of an ellipse is called the major axis, half of which is referred to as the semimajor axis ( $a$ ). It can also be described as half of the sum of pericenter and apocenter distances. Thus the major axis of an ellipse is sometimes called *the line of apsis*, the line connecting the two apsis and passing through the central body. The orbital sizes of celestial bodies are often expressed in terms of the semimajor axis of their orbits. Similarly, half of the smallest diameter of an ellipse is called the semiminor axis ( $b$ ). The two parameters are related via the eccentricity of the ellipse (see the next section). Furthermore, the orbital period (the time to complete one orbit around the central body) is related to the semimajor axis of the orbit via Kepler's third law given by Equation A.1:

$$P^2 = \frac{4\pi^2}{G(M_\star + M_p)} a^3, \quad (\text{A.1})$$

where  $G$  is the universal gravitational constant while  $M_\star$  and  $M_p$  are the masses of the star and the planet (or the two bodies involved) respectively. When using standard units, Equation A.1 reduces simply to  $P^2 = a^3$ . Thus the orbital period can be used to determine the size of the orbit and vice versa and the two are used for mass measurement.

## A.2 Eccentricity ( $e$ )

Eccentricity ( $e$ ) is a measure of the elongation of the orbit. For bound orbits, it varies between 0 and 1, with  $e = 0$  defining a circle, a special form of an ellipse. Eccentricity can be calculated from the major and minor axes through Equation A.2:

$$e = \sqrt{1 - \frac{b^2}{a^2}}. \quad (\text{A.2})$$

Therefore, the pericenter and apocenter distances, denoted by  $r_{peri}$  and  $r_{apo}$ , can be expressed in terms of the size and eccentricity of the orbit and are given by Equations A.3:

$$\begin{aligned} r_{peri} &= a(1 - e) \\ r_{apo} &= a(1 + e) . \end{aligned} \tag{A.3}$$

This means that the distance between the center of the ellipse to either of its foci is  $ae$ , thus eccentricity is a measure of deviation from a circle.

Except for Mercury, the orbital eccentricities of the Solar System planets are all less than 10%. However, this is not necessarily the case for the extrasolar planets that have thus far been detected, with some such as Fomalhaut b having an eccentricity as high as  $\sim 0.8$  (Pearce et al., 2015).

### A.3 Inclination ( $i$ )

The angle between the orbital plane of a body with the reference plane (i.e. the ecliptic for the Solar System objects) is called the inclination ( $i$ ). It varies between  $0^\circ$  (if the body's orbit lies in the reference plane) to  $180^\circ$ . By definition, Earth's orbital inclination is  $0^\circ$  while the other Solar System planets are found to orbit the Sun to within  $10^\circ$  of the ecliptic plane.

### A.4 Longitude of the Ascending Node ( $\Omega$ )

The two points where the orbital plane of a body intersects the reference plane are called the nodes and the line connecting them is referred to as the line of nodes. The point at which the orbiting body crosses a node going upward (downward) is called the ascending (descending) node. On the other hand, the longitudes of the nodes are measured from a reference direction (the first point of Aries for the Solar System). Therefore, the angle between the ascending node of the orbiting body and the reference direction measured along the plane of reference is called the longitude of the ascending node ( $\Omega$ ) and varies from  $0^\circ$  to  $360^\circ$ .

## A.5 Argument of Pericenter ( $\omega$ )

The orbital element specifying the direction of the line of apses is given by the argument of pericenter ( $\omega$ ) which is the angle between the pericenter (closest point of orbit to the central body) and the ascending node measured along the orbital plane of the body. The sum of the argument of pericenter and the longitude of the ascending node is called the Longitude of Pericenter ( $\varpi$ ):  $\varpi = \Omega + \omega$ .

## A.6 True Anomaly ( $\nu$ )

Due to the elliptical nature of bound orbits, the position of an orbiting body along its orbit is often quantified using the angle its radius vector makes with the pericenter and is called the true anomaly,  $\nu$ , or more precisely  $\nu(t)$ . It can be used to calculate the distance,  $r$  between the two bodies at any given time if the size and shape of the orbit are known (see Equation A.4).

$$r = \frac{a(1 - e)^2}{1 + e \cos(\nu)} \quad (\text{A.4})$$

Note that at pericenter ( $\nu = 0$ ) and apocenter ( $\nu = 180$ ), equation A.4 reduces to Equation A.3 for  $r_{peri}$  and  $r_{apo}$ , respectively.

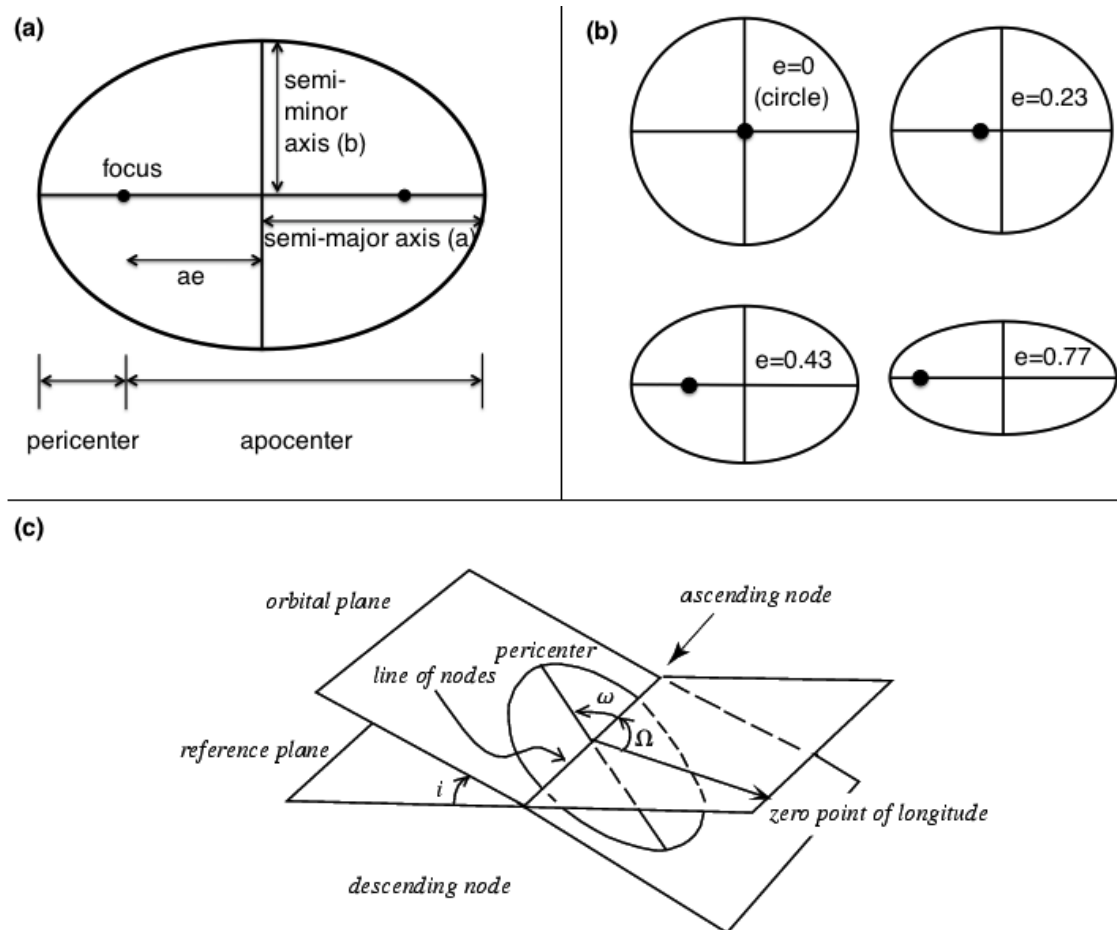


Figure A.1: Orbital parameters that describe the size, shape, and orientation of any Keplerian orbit. The size of the orbit is defined by its semimajor axis,  $a$  (panel (a)), its shape by eccentricity,  $e$  (panel (b)) and its orientation by three parameters that are measured with respect to a reference plane and a reference direction: inclination,  $i$ , longitude of the ascending node,  $\Omega$ , and the argument of pericenter,  $\omega$  (panel (c)\*). These together with true anomaly,  $\nu$ , provide a complete set of elements describing orbits in celestial mechanics.

\*Credit: Wolfram Research



# Bibliography

Murray, C. D. and Dermott, S. F., 1999, *Solar System dynamics* (Cambridge: Cambridge Univ. Press).

Pearce, T. D., Wyatt, M. C., and Kennedy, G. M., 2015, MNRAS, 448, 3679.

Roy, A. E., 2005, *Orbital Motion*, 4th ed., (Bristol: Institute of Physics Publishing).

# Curriculum Vitae

**Name:** Maryam Tabeshian

**Post-Secondary Education and Degrees:** Doctor of Philosophy, Astronomy  
University of Western Ontario  
London, ON, CA  
2012 - 2017 Ph.D.

Master of Science, Astronomy  
University of Western Ontario  
London, ON, CA  
2010 - 2012 MSc.

Bachelor of Science, Physics  
City University of New York, Hunter College  
New York, NY, USA  
2001 - 2004 BSc.

**Honors and Awards:** University of Western Ontario Graduate Research Scholarship  
2010-2016

**Related Work Experience:** Sessional Instructor  
Astronomy 2022B: Origin of the Universe  
University of Western Ontario  
Winter 2017

Graduate Research and Teaching Assistant  
University of Western Ontario  
2010-2017

**Publications:**

**Tabeshian M.**, and Wiegert, P. A., *Detection and Characterization of Extrasolar Planets through Mean-Motion Resonances I.: Simulations of Hypothetical Debris Disks*, 2016, The Astrophysical Journal (ApJ), 818, 159.

**Tabeshian M.**, and Wiegert, P. A., *Detection and Characterization of Extrasolar Planets through Mean-Motion Resonances. II. The Effect of the Planet's Orbital Eccentricity on Debris Disk Structures*, 2017, The Astrophysical Journal (ApJ) (submitted).

**Tabeshian M.**, and Wiegert, P. A., *Detection and Characterization of Extrasolar Planets: Applying a Particle-only Model to the HL Tau Disk*, In Prep.